Nanocomposite Glass-Ceramic Scintillators for Radiation Spectroscopy

A Thesis

Presented to

The Academic Faculty

By

Meredith Brooke Barta

In Partial Fulfillment

Of the Requirements for the Degree

Master of Science in Materials Science and Engineering

Georgia Institute of Technology

December 2012

Nanocomposite Glass-Ceramic Scintillators for Radiation Spectroscopy

Approved by:

Christopher J. Summers
School of Materials Science & Engineering
Georgia Institute of Technology

Brent K. Wagner
Electro-Optical Systems Laboratory
Georgia Tech Research Institute

Jason H. Nadler
Electro-Optical Systems Laboratory
Georgia Tech Research Institute

Kenneth Sandhage
School of Materials Science and Engineering
Georgia Institute of Technology

Zhitao Kang
Electro-Optical Systems Laboratory
Georgia Tech Research Institute

Date Approved: October 12, 2012

ACKNOWLEDGEMENTS

I must first thank my family and friends for their relentless support and encouragement throughout my academic career and my life. Without Lauren's pep talks, Daddy's unwavering confidence, Mama's indignation on my behalf, and Michael's daily engineering discussions, I would have never made it this far. They and my uncle, Steve Betts, inspired and encouraged me to become an engineer when I was a little girl playing with Legos. More importantly, they always remind me that a sense of self-worth is not found in one's chosen profession, and that if a person truly has remarkable intellect, they do not need to tell you about it. They just do awesome things and don't care if you think it's awesome or not.

For my professional development, I am deeply indebted to Jason. His remarkable (some might say insane) willingness to hire undergrads with damaged GPAs gave me the opportunity to work in a lab and put nebulous classroom theories into practice. Thankfully he was also a strong proponent of second chances, and did not kick me to the curb, even after I nearly set fire to the lab. I have also appreciated the help provided by other GTRI research scientists, as well as the host of technicians and laboratory managers around Georgia Tech who were generous with their time and patient in their explanations of complex topics. Finally, I must thank the Department of Homeland Security in general, and Program Manager Mark Wrobel in particular, for funding this work under contract number 2008-DN-077-ARI015-05.

TABLE OF CONTENTS

LIST OF TABLES

LIST OF FIGURES

SUMMARY

In recent years, the United States Departments of Homeland Security (DHS) and Customs and Border Protection (CBP) have been charged with scanning every cargo container crossing domestic borders for illicit radioactive material. This is accomplished by using gamma-ray detection systems capable of discriminating between non-threatening radioisotopes, such as ^{137}Cs, which is often used in nuclear medicine, and fissile material, such as ^{235}U, that can be used to make nuclear weapons or "dirty" bombs. Scintillation detector systems, specifically thallium-doped sodium iodide (NaI(Tl)) single crystals, are by far the most popular for this purpose because they are inexpensive relative to other types of detectors, but are still able to identify isotopes with reasonable accuracy. However, increased demand for these systems has served as a catalyst for the research and development of new scintillator materials to surpass NaI(Tl).

The purpose of the current investigation is to develop new glass-ceramic nanocomposite scintillators with gamma-ray spectroscopy performance equivalent to that of NaI(Tl) single crystals, but that are also sensitive to alpha-radiation. Glass-ceramics facilitate the study of scintillator compositions that cannot be grown via single crystal methods, producing scintillator volumes of $50cm^3$ or greater, and investigating novel geometries beyond the standard cylinder. This investigation will focus on the development and optimization of both the scintillating crystalline phase and the host glass matrix compositions, and scaling batch sizes to produce larger volume glass-ceramic scintillators.

INTRODUCTION

In recent years, the United States Departments of Homeland Security (DHS) and Customs and Border Protection (CBP) have been charged with task of scanning every cargo container crossing domestic borders for illicit radioactive material [1]. This is accomplished by using gamma-ray detection systems capable of discriminating between non-threatening radioisotopes, such as ^{137}Cs, which is often used in nuclear medicine, and fissile material, such as ^{235}U, that can be used to make nuclear weapons or "dirty" bombs [2]. Scintillation detector systems, specifically thallium-doped sodium iodide (NaI(Tl)) single crystals, are by far the most popular choice for this purpose because they are inexpensive relative to other types of detectors [3], but are still able to identify isotopes with reasonable accuracy [4]. However, increased demand for high-performance radiation detection systems has served as a catalyst for the research and development of new scintillator materials with potential to surpass NaI(Tl).

The focus of a majority of recent scintillator materials research has been on sintered transparent ceramics [5], phosphor-doped organic matrices [6], [7], and development of novel single crystal compositions [8–14]. Transparent ceramics are synthesized by thorough mixing and hot-isostatic pressing (HIP-ing) of a variety of scintillation crystal compositions. This method eliminates the solute segregation commonly found in NaI(Tl) single crystals [13], [15], but variations in refractive index through the bulk can scatter emitted photons and geometries are typically limited to cylinders or cubes. Phosphor-doped organic matrices consist of nano- or micro-scale luminescent phosphor powders

dispersed in a liquid polymer solution, such as poly(vinyl alcohol), which is then cured to form a solid scintillator. These scintillators can be fabricated into a wide variety of shapes, from cones to plates, and sizes up to several hundred cubic centimeters. However, nano-scale phosphor powders tend to agglomerate into micron-size or larger clusters, and the mismatch in refractive index between the powders and matrix often cause photon scattering to become significant [16], [17]. A more detailed report of the work conducted by this group on phosphor-loaded polymer composite scintillators can be found in the Appendix. Single crystals of novel compositions such as $LaBr_3$(Ce) and SrI_2(Eu) have been shown to surpass the energy resolution of NaI(Tl) [18–22], but are available in limited sizes (<15cm^3) for commercial use and must be encapsulated in stainless steel, aluminum, or other environmental isolation medium to prevent degradation due to atmospheric moisture. Finally, some of the most promising new materials are glass ceramic nanocomposites [23–25]. These composites are synthesized by mixing scintillating powders such as GdF_3 with and glass-formers such as silica and alumina, and then firing to form a homogenous melt. The melt is then cast and quenched to yield a scintillating glass, with geometries varying from cylinders to tubes or plates. The cast glass is then re-heated to 50-150°C above the glass transition temperature to precipitate 20-50nm scintillating crystallites while inhibiting matrix devitrification. Melt casting allows a wide variety of geometries to be investigated, and *in-situ* precipitation of scintillating crystallites from a glass matrix provides environmental isolation and allows investigation of novel compositions not typically grown as single crystals [26–30].

A schematic of the configuration of a standard radiation detection system is shown in *Figure 1*. Scintillators (item (A)) are coupled to a photomultiplier tube (PMT), item (B), that converts the photon pulses produced by absorbed radiation energy into electrical pulses with amplitude proportional to the number of photons in the pulse. The peak spectral sensitivity wavelength will vary with the brand of PMT used, though the most common models usually exhibit peak sensitivity to either 350nm or 543nm photons. The electrical pulses are then passed to an array of signal amplifiers (C) and multi-channel analyzers (D) that sort the pulses according to their amplitude into channels that correspond to a particular keV energy. Because each isotope emits a characteristic series of decay product energies, the source isotope can be identified by its pulse-height spectrum [2], [4].

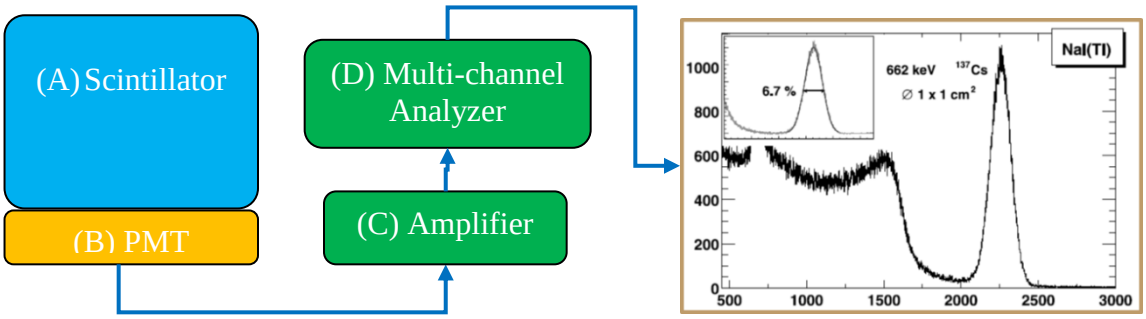

Figure 1: Schematic of gamma-ray detection system

The accuracy with which the source isotope may be identified depends on the energy resolution of the peaks in the pulse-height spectrum [31], which is defined by the full-width at half the maximum peak energy divided by the peak energy (equation (1)).

$$R = \frac{\Delta E}{E_{peak}} \qquad (1)$$

Peak resolution increases with the number of photons produced per pulse by the scintillator [32–34], known as the light yield, and the number of photons produced by photoelectric interactions between the incident radiation particles and the scintillator material. NaI(Tl) scintillators generate 50,000 photons per MeV of radiation energy absorbed, resulting in an energy resolution of 6-7% for a 662keV incident gamma-ray [35]. Greater energy resolution improves the accuracy of isotope discrimination [36], as shown by the distinct spectra for 137Cs and 60Co shown in *Figure 2*.

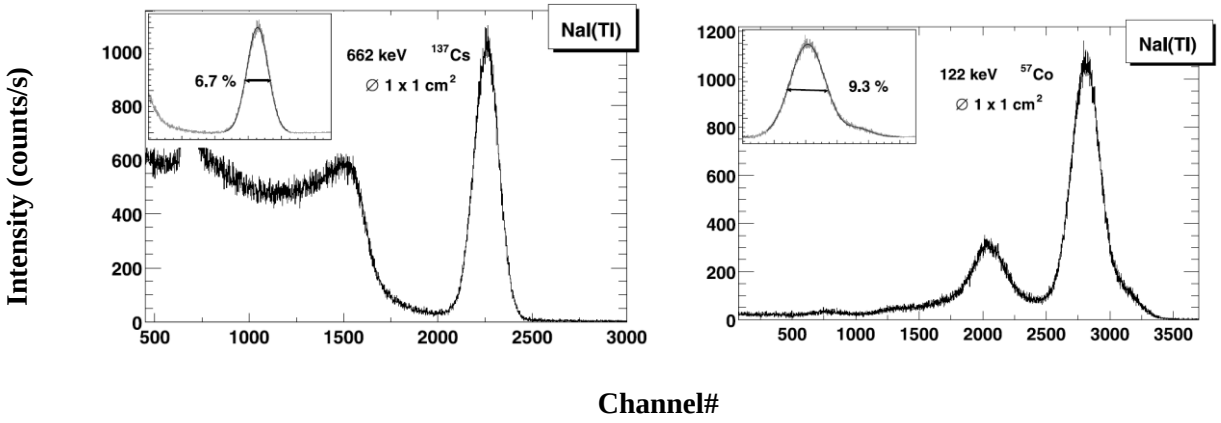

Figure 2: Energy spectra for ^{137}Cs (left) and ^{57}Co (right) generated by a NaI(Tl) single crystal [37]*. The inset indicates the scintillator's energy resolution at the photopeak.*

The purpose of the current investigation is to develop new glass-ceramic nanocomposite scintillators with gamma-ray spectroscopy performance comparable to that of NaI(Tl) single crystals, and that are also sensitive to alpha-particles, unlike NaI(Tl). Studies will focus on compositions that cannot be grown via single crystal methods, producing scintillator volumes of $50cm^3$ or greater, and characterizing changes in scintillator performance between glass systems of varying composition, with a study of varying geometries the subject of a future investigation.

BACKGROUND

Overview of Scintillation Process

Inorganic scintillators convert energy from incident radiation into thousands of 3-6eV photons via the electronic excitation and relaxation scheme illustrated in Figure 3. When the kinetic energy of the incident radiation particle ($h\nu_{ex}$) is greater than the band gap energy of the scintillator (E_2-E_1), the energy is absorbed by promoting an electron from the valence band (E_1) of the scintillator to the conduction band (E_2), leaving a corresponding hole in the valence band [38]. Most scintillator band gaps are between 5-7eV, which allows a large number of photons to be produced per unit radiation energy absorbed, but is not so small as to allow excitation due to thermal energy available at room temperature [36], [39]. If the electron-hole pairs were to recombine directly from the conduction and valence bands, the resulting photon would be far into the UV regime and outside the spectral sensitivity of most PMTs [40]. Instead, the electron-hole pairs are transferred to activator ions doped into the host crystal. The energy separation between the ground (E'_1) and excited (E'_2) electron energy levels of the activator ion is smaller than that of the host crystal band gap, and the wavelength of emitted photons depends on the activator ion used [41]. For example, Ce^{3+} centers are used to produce 350nm photons while Tb^{3+} are used to produce 543nm photons [42], [43].

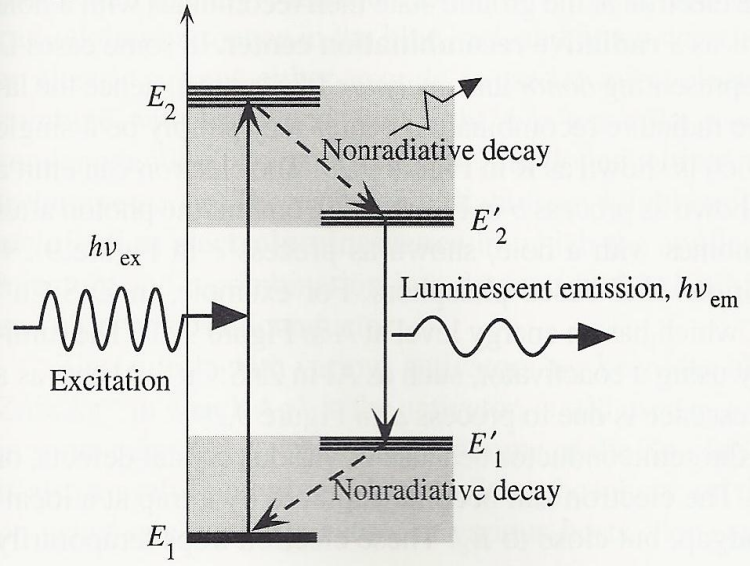

Figure 3: Schematic of scintillation process. The narrower separation of energy levels in the rare-earth ion allows the emitted photon energy to be within the visible regime [38]

In order for this electron transition scheme to produce an acceptably high light yield, the scintillator must have an ordered, periodic lattice structure. This reduces the statistical variance in electron-hole recombination modes, and ensures that a large fraction of the relaxation processes are radiative [44]. If the lattice periodicity is disturbed due to defects or breakdown in long-range order, new recombination or relaxation modes are introduced, which can either produce photons outside of the desired wavelength range or allow electrons to relax via non-radiative lattice vibrations (phonons) [35]. The strong ionic bonding of NaI(Tl) provides an ordered crystallographic structure that minimizes phonon relaxation modes and creates similar crystal field splitting effects in the electron energy levels of the luminescent ion. Elements such as iodine, bromine, and lanthanum are preferred because their high atomic number ensures that a majority of the incident gamma-ray energy is deposited within the dimensions of the scintillator.

The time duration of the scintillation process is usually 200ns or less, and so the PMT is configured to collect photons in time increments slightly longer than the scintillator decay time. Thus, any radiation energy deposited in the scintillator over this time period is integrated into a single pulse, with the height proportional to the amount of energy deposited [44]. The maximum achievable pulse height represents interaction events in which the full energy of the radiation was absorbed within the scintillator either via a single photoelectric interaction or a series of Compton interactions. Smaller pulses result when the radiation only deposits a fraction of its energy in the form of Compton interactions prior to escaping the scintillator, or when secondary reaction products escape prior to full absorption [36].

Overview of Current Single Crystal Scintillators

A high-performance scintillator displays the following characteristics: 1) Efficiently converts the absorbed incident radiation energy to detectable photons (high scintillation efficiency), with the light yield remaining proportional to the energy deposited over a wide energy range; 2) the scintillator is transparent to the emitted photon wavelengths to minimize absorption; 3) the time required to convert radiation energy to photons (decay time) is on the order of a few hundred nanoseconds or less; and 4) the material may be fabricated to volumes of at least a few cubic centimeters [44]. No single scintillator fully meets all of these criteria, and requires the quality of some properties to be sacrificed for the sake of improved performance elsewhere.

NaI(Tl) single crystals fulfill many of these requirements, though new single crystal compositions such as $LaBr_3$(Ce) and SrI_2(Ce) developed in the last decade suggest that energy resolution can be improved with the new compositions [10], [20], [45], [46]. However, growing large volume crystals from these compounds is difficult because their low-symmetry crystal structures ($LaBr_3$(Ce) is monoclinic) cause anisotropic thermal expansion during cooling, which causes larger crystals to fracture [11]. Additionally, limiting research efforts only to the development of new single crystal compositions restricts scintillator geometry solely to cylinders, and eliminates potential investigations into the effect of varied geometries on the scintillator performance. Finally, most of these ionic salts are extremely hygroscopic, and so must be encased in stainless steel or other isolation medium to prevent degradation due to atmospheric moisture. Alpha-particles cannot penetrate the cover and so these hygroscopic scintillators are useful only for gamma-spectroscopy.

Glass-Ceramic Nanocomposite Scintillators

Glass-ceramic nanocomposite scintillators are a promising alternative to single crystals because new scintillator compositions, shapes, and sizes may be developed [23], [47–50]. Glass-ceramic nanocomposites contain nanoscale crystallites precipitated from an amorphous host glass. Using nanoscale scintillating crystallites rather than a single crystal monolith allows scintillator compositions such as $LaBr_3$(Ce) to be fabricated to larger ($45cm^3$) volumes, and the spectroscopy performance to be directly compared to NaI(Tl) [44]. Also, because glass-ceramic synthesis begins by casting a homogeneous glass melt, new geometries may be fabricated and cast to near-net shape [51]. Finally, the

glass matrix ensures environmental isolation of the hygroscopic scintillating crystals, and so glass-ceramic scintillators show potential to serve as viable detectors in alpha- and neutron-spectroscopy in addition to gamma-rays [50], [52–54]. For glass-ceramics to be successfully used as scintillators, several material properties must first be optimized. For example, the glass matrix must have a high solubility limit of scintillating, the nucleation and growth of crystallites must be readily controllable by varying aging temperature or duration, and the rare-earth activator must be chosen to produce an emission wavelength that matches the peak spectral sensitivity of the PMT used. The main properties of interest to this study are the effect of precipitated particle size on spectroscopy performance [31], [55–57], the relationship between the host glass matrix and the solubility of scintillating compounds [58], [59], and the variation in emitted photon intensity and wavelength with batch composition [39], [60], [61]. These concepts are discussed in further detail below.

Effect of Precipitated Crystallite Size

The size of crystallites precipitated in a glass-ceramic is controlled by a process known as ceramization [62–64] in which one crystalline phase is preferentially precipitated from an amorphous host matrix. There is greater control over the ceramization process when the temperature of the precipitation reaction lies between and is well separated from the glass transition and matrix devitrification temperatures. This temperature separation allows the desired crystalline phase to form without devitrification of the glass matrix. The size of precipitated particles is controlled by varying the ceramization, or aging, temperature,

with particle size typically increasing with aging temperature, as illustrated by the micrographs in *Figure 4* [54], [65].

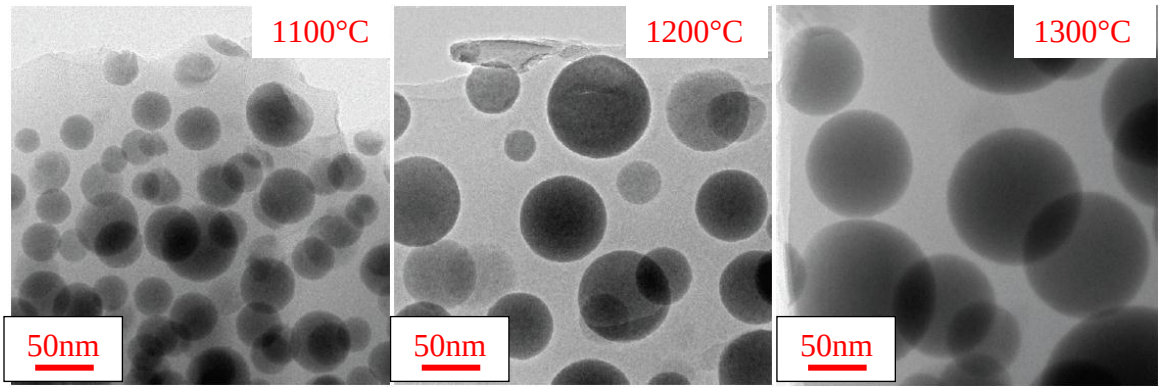

Figure 4: Transmission electron micrographs showing nanoscale crystallites precipitated from a glass matrix. Micrographs show how crystallite size increases with aging temperature [65]

The choice and concentration of rare-earth dopants has also been shown to affect the size of precipitated crystallites. For example, a study performed by Bocker [55] found that higher concentrations of ErF_3 incorporated into the oxyfluoride host glass resulted in a smaller average size of PbF_2 crystallites. The precipitated particle size should be less than 50nm to minimize Rayleigh scattering and scattering due to the mismatch in refractive index between the crystalline and amorphous phases [66], [67].

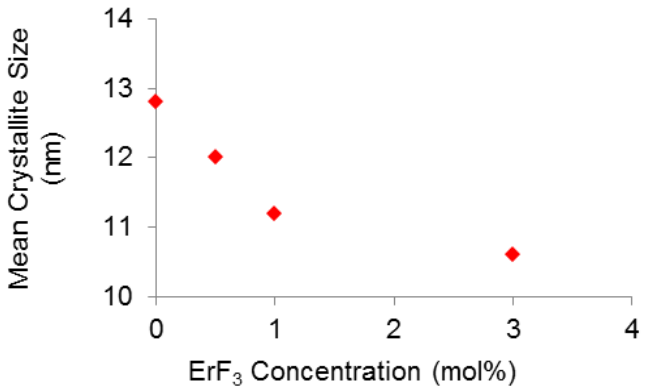

Figure 5: Relationship between rare-earth loading and mean precipitated crystallite size. In this case, higher Er^{3+} concentrations result in smaller average crystallite size [55].

Effect of Matrix Glass Free Volume

The solubility of scintillating compounds in the host glass is limited by the free volume available in the glass network. Oxide-based host glass matrices with large free volume can accept a higher concentration of rare-earth halides while maintaining transparency in the visible range [68], [69]. Glasses whose primary structure is composed of tetrahedrally-coordinated cations (such as silica or alumina) are expected to have higher network free volume than glasses whose cations are triangularly-coordinated (such as borates) [69]. If the solubility limit is exceeded, the glass matrix may reject the undissolved compounds (as shown in Figure 6), causing a crystalline phase with particle size larger than the emitted wavelength to form and reduce transparency of the final glass-ceramic [70], [71].

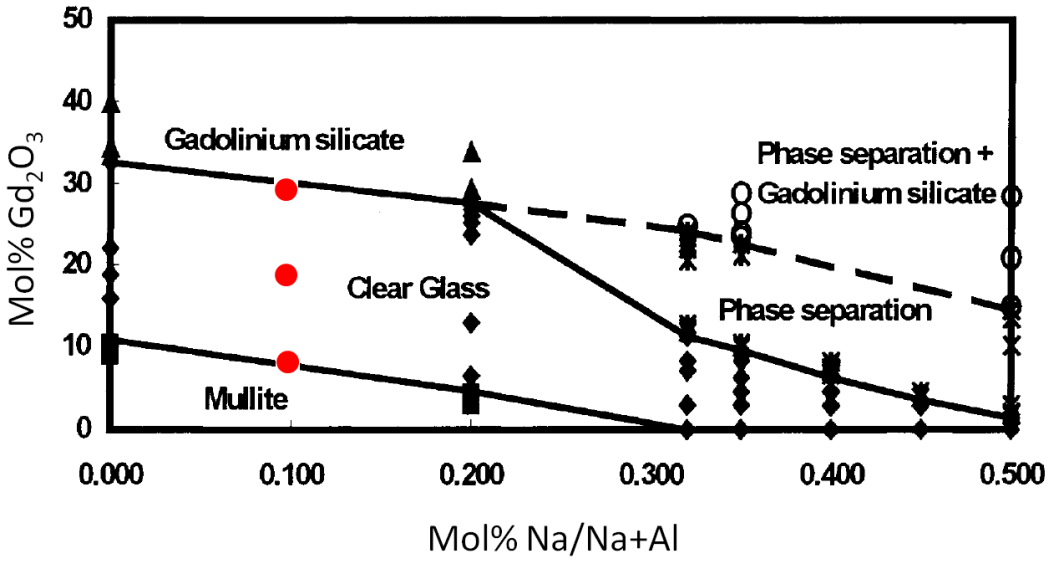

Figure 6: Variation in the morphology of a Gd_2O_3–doped alumino-borosilicate host glass with Gd_2O_3 concentration [72]. *The figure indicates compositions necessary to form a clear glass and those that cause a gadolinium silicate or mullite phase to separate from the melt. The red dots represent the Gd_2O_3 and concentrations used in a portion of this study.*

Dependence of Emitted Photon Intensity (Light Yield) on Composition

Arguably one of the most important properties of any scintillator is the number of photons produced by a scintillator per unit energy of incident radiation absorbed, which is known as the light yield. The light yield places an inherent limit to the achievable energy resolution of a scintillator, with increasing light yield corresponding to greater energy resolution and more accurate isotope discrimination [44]. Light yield is maximized by ensuring a high absorption cross-section of the scintillating material and limiting the amount of absorbed energy released via non-radiative transitions such as phonons. A material with a high absorption cross-section will absorb the full energy of the incident radiation within the dimensions of the detector [36], [73]. Absorption cross-section is increased by using high density (high *Z*) materials [35]. The light yield is also increased by using compounds with a smaller band gap [74], such as BaF_2 [75] or Gd_2SiO_5 [76], which will produce more photons per MeV of incident radiation particle energy absorbed. However, materials with band gaps smaller than 1eV must be operated at cryogenic temperatures to remove noise introduced by thermally excited electrons, and so compounds with band gaps of 5-7eV, which can operate at room temperature, are preferred [35]. Photon pulses produced within the scintillator must be transferred to a photomultiplier tube (PMT) and converted into an electrical signal that can be processed by the electronic multi-channel analyzer. The quantum efficiency of the PMT is a function of photon wavelength, and so it is advantageous to tailor the wavelength of scintillation photons to the spectral sensitivity of the particular PMT used. The most commonly used PMTs have peak sensitivity at either 320nm or 500nm [77].

Light yield is also affected by the concentration of the rare-earth dopant ion (Ce^{3+}, Eu^{2+}) within the host crystal ($GdBr_3$, SrI_2). Undoped $GdBr_3$ and SrI_2 crystals exhibit negligible luminescence, and so rare-earth dopant ions are needed to activate the host crystals to produce a high light yield and match the emitted photon wavelengths to the peak spectral sensitivity of the PMT [43]. However, the activator ion doping concentration in the host crystal must be optimized because neighboring luminescent centers that are too closely spaced may re-absorb emitted photons and cause concentration quenching [78]. By contrast, if the rare-earth ion concentration is too low, the density of luminescent centers may be too low to produce a high light yield.

Dependence of Emitted Photon Energy on Composition

The wavelength of photons emitted by the scintillating crystallites is affected by both the composition of the crystallites and the crystal field splitting of electron energy levels in the rare-earth ion, which is affected by the degree of order in the ion's structural surroundings [79–83]. During the aging/ceramization step, rare-earth ions diffuse from the amorphous matrix into the ordered crystallites. As the rare-earth dopants move to sites in the nanocrystals rather than the amorphous matrix, the nearest neighbor distances and locations become more periodic, which results in fewer possible electron transitions as splitting of outer electron orbitals in the ion is reduced [41]. This also increases the probability of radiative transitions as phonon relaxation probabilities decrease. As the number of possible electron transitions reduces to just a few excited and ground energy states, the range of emission energies (wavelengths) narrows and emission intensity increases [24]. As illustrated in Figure 7, the site that the rare-earth ion occupies in the

crystallite can also affect emitted photon wavelength. In this diagram, the larger separation distance between the excited and ground states of the ion in the octahedral site would yield higher energy photons relative to ions in the tetrahedral site.

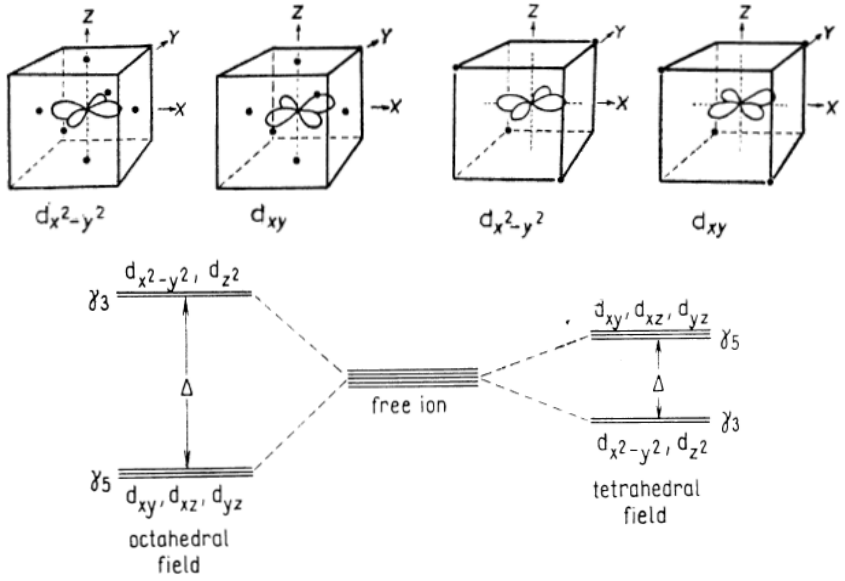

Figure 7: Schematic of changing emission energies due to orbital splitting as luminescent ions are incorporated into ordered crystalline structure [83]. *The figure illustrates how the ligand field surrounding the luminescent ion can change the d-orbital splitting of the ion, which in turn affects the scintillation photon energies.*

As an example, NaI adopts a rocksalt crystal structure, with thallium atoms forming a substitutional solid solution at the sodium sites. This creates four sites per unit cell that are theoretically available for thallium-doping. However, concentration quenching effects become significant when the thallium doping levels exceed 0.1mol%, meaning that only one site out of every 250 are occupied by a thallium atom. This creates a separation distance of approximately 160nm between thallium dopant sites in the single crystal. Finally, emitted photon wavelength will change with the charge of the rare-earth ion. For

example, Eu^{2+} ions have an emission peak centered around 430nm [20], while the peak for Eu^{3+} ions is closer to 600nm [84].

PROCEDURE

Materials Selection

Potential scintillating compounds were chosen based on the method described by Cherepy et. al. [51]. The group's selection criteria is illustrated schematically by the periodic table shown in *Figure 8*. They systematically eliminated elements that were not suitable for use as scintillators either due to inherent radioactivity or small band gaps that would create background noise in the energy spectrum, those that were not transparent to scintillation photon wavelengths, and those that were not conducive to growing large single crystals. While this project seeks to avoid single crystal growth, the behavior of scintillating crystallites in an amorphous host matrix is not yet well-understood, and so the list of potential scintillating materials was restricted to these compounds whose behavior has been previously studied to isolate the effects of nanoscale scintillating crystals and glass-ceramics on scintillator energy resolution.

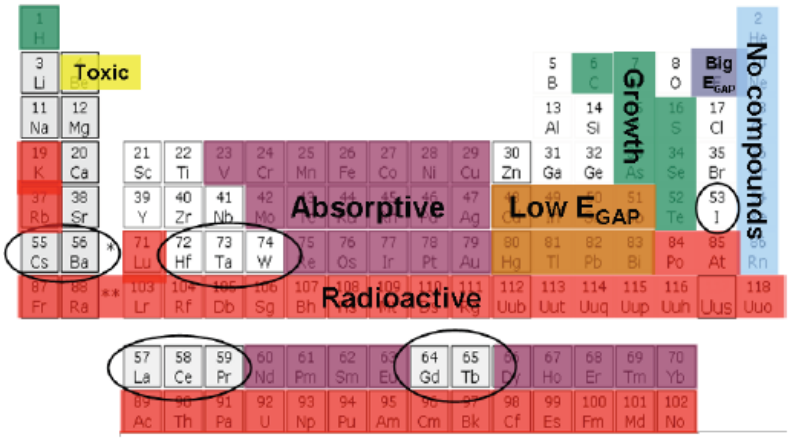

Figure 8: Schematic illustrating the criteria used for selecting potential scintillating crystal compositions [51].

Three host glass matrices were chosen to observe the effects of the matrix structure on scintillation. A sodium-borosilicate (NBS) system was chosen because of its low content of refractories such as alumina and silica, and high boron content that would facilitate relaxation of thermal stresses. The baseline ternary glass system was adapted from Pucker [85], though inhibiting phase separation was somewhat difficult, as shown by the large immiscibility region in the phase diagram in *Figure 9* [86]. Additional CaO and BaO were incorporated incrementally to promote mixing when phase separation proved to be problematic in early batches.

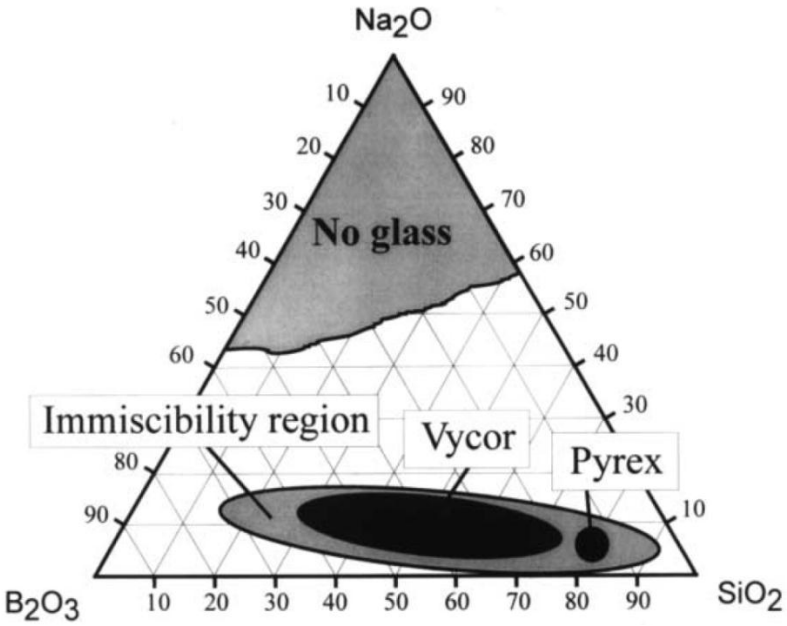

Figure 9: Phase diagram of the ternary sodium-borosilicate system with glass forming regions and areas of phase separation marked [86].

An alumino-borosilicate (ABS) system was chosen to increase the stability of the glass and create a larger network free volume into which the scintillating compounds may be dissolved. High-alumina glasses possess large network free volume because they are composed primarily of alumina tetrahedra. The baseline composition was adapted from

work by Li [72], who studied the solubility and partitioning of Gd_2O_3 in ABS glasses, with $GdBr_3$ and $CeBr_3$ substituted in place of the Gd_2O_3. Several articles in the literature [70], [87], [88] suggest that rare-earth constituents will preferentially partition into a borate-rich phase when incorporated into oxide glasses. A phase diagram of the ternary baseline glass system is shown in *Figure 10* [89].

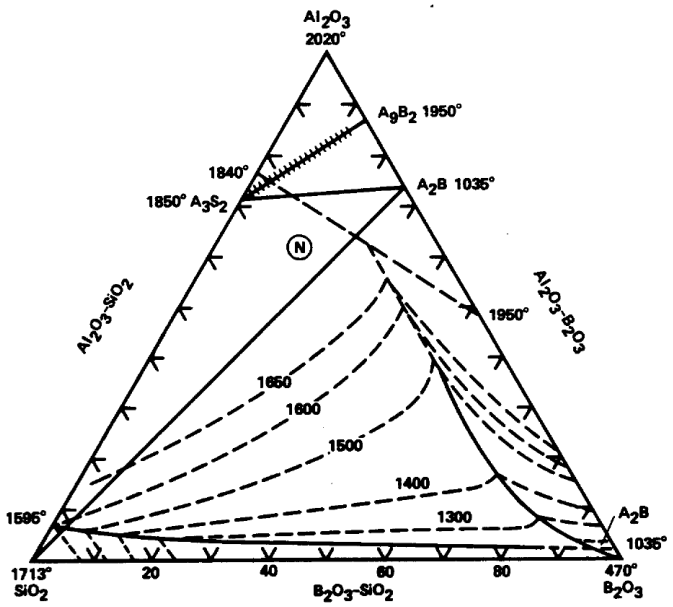

Figure 10: Phase diagram for a ternary alumino-borosilicate system [89]

A sodium-aluminosilicate (NAS) host glass was thus studied to investigate the behavior of the rare-earth halides in the absence of a borate-rich phase. This base glass composition was adapted from work by Chen [90], who studied the behavior of GdF_3(Eu) crystallites in a sodium-aluminosilicate host glass. The concentration of rare-earth dopants in the glass exceeded that reported in Chen's work in order to determine the solubility limit in the NAS glass. The phase diagram for this baseline system is shown in *Figure 11* [91].

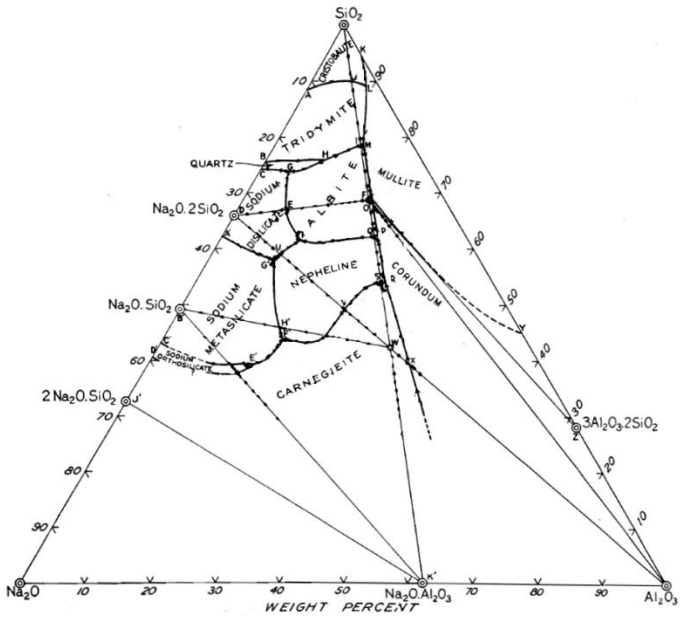

Figure 11: Phase diagram for baseline ternary sodium-aluminosilicate glass system [91]

Synthesis

All samples were prepared using the same melt casting method, though processing temperatures were altered to compensate for the varying concentration of refractory compounds between the series (presented with associated annealing temperatures in Table 1). High purity (>99.9%) precursor powders were used to minimize discrepancies and defects introduced by compositional impurities. All precursor powders were supplied by Alfa Aesar.

Efforts first focused on developing novel combinations of glass matrix and scintillating crystal compositions. The light yield and peak emission wavelength were analyzed to determine the composition's viability as a large scale glass-ceramic scintillator.

Compositions that proved promising were then scaled up to larger batch sizes useful for radiation spectroscopy measurements and optimization of ceramization schedules.

Sodium-Aluminosilicate (NAS) System

The series of samples with NAS base glass (shown in Table 1) were synthesized to optimize the concentration of scintillating compounds ($GdBr_3$ and $CeBr_3$) within the host matrix and to optimize the concentration of activator dopant (Ce^{3+}) within the host scintillation crystal ($GdBr_3$). The total concentration of $GdBr_3$ and $CeBr_3$ within the NAS glass matrix was increased in 1mol% increments until transparency was lost.

Table 1: Composition (in mol%) of batches prepared to maximize the loading of scintillating compounds into the NAS host glas.

SiO_2	NaF	Al_2O_3	$GdBr_3$	$CeBr_3$
48.3	18.7	15.4	14.8	2.93
47.5	15.1	18.3	15.9	3.16
46.6	18.0	14.8	17.1	3.39
46.3	17.9	14.7	17.7	3.50
45.9	17.7	14.6	18.2	3.61

Next, the ratio of $CeBr_3$ to $GdBr_3$ was optimized to provide a large population of luminescent centers while minimizing concentration quenching between neighbors. The compositions of samples synthesized in this series are given in Table 2. The total loading of rare-earth halides in the host glass was held constant at 19mol%.

Table 2: Composition (in mol%) of batches prepared to optimize Ce-doping in $GdBr_3$ host crystals to maximize luminescence intensity

SiO_2	NaF	Al_2O_3	$GdBr_3$	$CeBr_3$
49.8	19.2	15.8	15.2	0
48.4	18.7	15.4	17.4	0.2
48.3	18.7	15.4	14.8	2.93
48.3	18.7	15.4	13.8	3.88
48.2	18.6	15.3	11.4	6.4

Sodium-Borosilicate (NBS) System

Sodium-borosilicate (NBS) base glasses were studied to lower processing temperatures, and thus minimize burn off of the volatile $GdBr_3$ and $CeBr_3$. Batch compositions were based on work by Bartl [86], with $BaCO_3$ and CaO added to suppress phase separation. The most successful glass compositions are given in Table 3. Other compositions either devitrified or had such pronounced phase separation that additional characterization and analysis was not useful. Only 15mol% $GdBr_3$-$CeBr_3$ was able to be incorporated before phase separation in the liquid degraded the transparency of the cast glass. The Na_2O was added as a carbonate (Na_2CO_3) because pure Na_2O reacted violently with the adsorbed water in the $GdBr_3$ and $CeBr_3$. The BaO was also added as a carbonate ($BaCO_3$) and B_2O_3 as H_3BO_3 due to the lower melting points that provided greater flux to the silica and alumina and the reduced cost per gram.

Table 3: Composition (in mol%) of batches prepared to maximize $GdBr_3$(Ce) doping in the NBS system while maintaining glass transparency.

B_2O_3	SiO_2	Na_2O	CaO	BaO	$GdBr_3$	$CeBr_3$
31.7	36.7	11.2	7.9	5.37	6.01	1.20
30.6	35.5	10.8	7.61	5.17	8.60	1.71
29.1	33.8	10.3	7.23	4.92	12.3	2.44
20.4	42.6	10.1	7.10	4.82	12.5	2.49

Alumino-Borosilicate (ABS) System

Alumino-borosilicate (ABS) glasses were studied to increase solubility of scintillating compounds in the glass matrix. Similar to the NBS system, H_3BO_3 and Na_2CO_3 precursor constituents were used to incorporate the necessary B_2O_3 and Na_2O concentrations,

respectively, to the glass batch. While transparent samples up to 30mol% $GdBr_3$ – $CeBr_3$ were achieved, samples with 20mol% scintillating compounds exhibited superior performance and so were more extensively characterized. A batch with 10mol% $GdBr_3$(Ce) loading was also prepared, though was opaque and not able to be cast. The composition of each batch is given in Table 4.

Table 4: Composition (in mol%) of batches prepared to maximize $GdBr_3$(Ce) loading in the ABS system while maintaining glass transparency

SiO_2	B_2O_3	Al_2O_3	Na_2O	$GdBr_3$	$CeBr_3$
34.4	25.0	25.1	6.25	7.63	1.59
30.3	22.0	22.0	5.50	17.4	2.80
26.2	19.0	19.0	4.75	26.1	4.96

Batch Processing

For batch sizes smaller than 100g, precursor powders were mixed by hand in a mortar and pestle, and then charged into an alumina crucible. For batch sizes larger than 100g, the precursor powders were ball-milled for two hours in a polypropylene container using ¼ inch diameter alumina milling beads, followed by a deionized water rinse to ensure intimate mixing. The slurry was dried and the resulting material ground and charged into an alumina crucible. The mixture was heated above the melting temperature in a Thermolyne-Barnstead 46-200 High Temperature Muffle Furnace under an inert argon atmosphere to homogenize the melt. For batches smaller than 100g, a graphite plate was placed on top of the crucible to provide a reducing atmosphere, with a dwell time of two hours at the melting temperature. For batches larger than 100g, the dwell time at the melting temperature was extended to four hours to ensure homogeneous mixing of the low viscosity, low melting temperature liquid and the more refractory silica and alumina

constituents. The graphite plate would burn off before the end of the dwell, which caused the Ce^{3+} to oxidize to Ce^{4+}. To maintain a reducing atmosphere, the graphite plate was replaced with an alumina plate and tube and a 90%:10% mixture of Ar:CO purge gas was applied.

Once homogenized, the melt was cast into a cylindrical graphite mold preheated to 200°C, and placed into an annealing furnace to remove thermal stresses and control cool to room temperature. Annealing temperatures varied from 450-650°C depending on the composition of the glass batch. The cast glass was then heated to an aging temperature (determined from DTA analysis, described below) 50-150°C above the glass transition temperature to precipitate the scintillating crystalline phase. Multiple exothermic peaks were visible in the DTA traces for the NAS and ABS glass systems, and so aging studies were performed at each temperature. Shards of as-cast glass were held for 5-96 hours at the aging temperature of interest. The aged shards were then ground for photoluminescence and X-ray diffraction characterization studies. Samples were compared based on the photoluminescence light yield produced by each combination of dwell time and aging temperature. A summary of the processing temperatures used for each glass system are summarized in Table 5.

Table 5: Processing parameters used in synthesis of samples from the NAS, NBS, and ABS glass systems

Sample	Melting Temperature	Annealing Temperature	Annealing Time	Largest Sample Mass
NAS	1450°C	650°C	36 hours	106g
ABS	1400°C	550°C	36 hours	127g
NBS	1375°C	450°C	24 hours	38g

Batch sizes synthesized in the composition study were approximately 50g to allow for a preliminary evaluation of quality before scaling to larger sizes. For samples used in radiation spectroscopy measurements and ceramization studies, batch sizes were held near 150-250g to produce a sample of similar size to single crystal scintillators currently in use. There was significant mass loss when the carbonates decomposed to oxides and the adsorbed water burned off of the halides, and so the final glass yield was usually less than 130g.

Characterization

Differential Thermal Analysis (DTA)

Differential thermal analysis was performed to evaluate the characteristic glass transition, crystal precipitation, and matrix devitrification temperatures of each glass sample. A Linseis STA PT-1000 TG-DTA with a maximum operating temperature of 1000°C and an alumina reference samples was used for thermal analysis of all samples. Glass samples (140-160mg) were finely ground using a mortar and pestle and then loaded into an uncovered alumina crucible. The samples were heated to 1000°C using a heating rate of 10°C per minute under an argon atmosphere. The dependence of ceramization temperature on glass composition was evaluated by observing shifts in the exothermic crystallization peak.

Photoluminescence Excitation (PLE) and Emission (PL)

Photoluminescence emission (PL) and excitation (PLE) measurements were performed to quantify the light yield and peak emission wavelength of the glass-ceramic scintillators.

Samples of finely ground powder (40-60mg) were loaded into the stage, and then scanned with a Spectra-Physics BeamLok Ar-ion laser and SPEX 1681 0.22m and SPEX 1000M Spectrometers. A 350nm excitation wavelength was used for PL measurements with a scanning range of 370 to 500nm, a 1nm step-size, and an integration time of one second per step. For PLE measurements, a 423nm monitor wavelength was used over a 200-400nm scanning range with similar scanning rates and steps.

X-Ray Diffraction (XRD)

To observe the evolution of the crystalline phase at different aging temperatures, samples of aged glass were finely ground in a mortar and pestle, loaded into a 1-inch diameter powder XRD stage, and packed to form a level surface. X-ray diffraction patterns were collected using an X'Pert PRO Alpha-1 diffractometer by PANalytical (Westborough, MA) equipped with a Cu-Kα source (λ = 1.54 Å) and an ultra-fast X'Celerator. Scans were performed over 10-70° (2θ) with a step size of 0.016° (2θ) and two seconds per step. Resulting patterns were analyzed using MDI Jade 9 and compared to standards from the powder diffraction database of the International Centre for Diffraction Data (ICDD).

Radiation Spectroscopy

Radiation spectroscopy measurements provide the most direct comparison between the energy resolution of the novel glass-ceramic scintillators and current NaI(Tl) crystals. Because energy resolution not only varies between scintillators, but also with energy of the incident radiation, it is customary to quote energy resolution of any scintillator in terms of its FWHM at 662keV for gamma-rays from a ^{137}Cs source and at 5.486 MeV for

alpha-particles from a ^{241}Am source. All spectroscopy tests were conducted at the Environmental Radiation Center (ERC) at the Georgia Tech Research Institute.

Cylindrical samples with diameters ranging from 2.5-5cm, depending on the final batch yield, were measured to mimic the geometry of NaI(Tl) crystals as closely as possible. Samples were wrapped in Teflon tape to internally reflect emitted photons and minimize escape. Teflon tape was not applied to the surface to be coupled to the PMT and omitted entirely from samples during alpha-spectroscopy measurements. The sample was then coupled to a Hamamatsu R6231-100 PMT (peak sensitivity of 350nm) using silicon-based refractive index matching grease (available from Alpha-Spectra, Inc.), and the apparatus sealed in a shielded counting chamber. A button source of ^{137}Cs or ^{241}Am (previously calibrated) was placed on top of the scintillator and a spectrum acquired with a Canberra multi-channel analyzer using 1024-channels and 100-1,000 second counting times (depending on source intensity), with a PMT gain of 400. Energy spectra produced by the glass-ceramics were compared to those from a 5cm diameter NaI(Tl) crystal (from Alpha Spectra, Inc.) sealed in an aluminum can and tested under identical conditions.

Electron Microscopy

Scanning electron microscopy (SEM) and transmission electron microscopy (TEM) were performed on several samples to observe the microstructure of the as-cast glass and glass-ceramic samples. For SEM, shards of glass were encapsulated in a cylindrical acrylic and then carbon sputtered to prevent charging under the electron beam. Samples were observed at magnifications ranging from 30,000X to 150,000X using a 15kV accelerating voltage and a 10μA beam current in a Hitachi S-4700 SEM. This instrument had limited

capability to observe 50nm or smaller crystallites, and so a few samples (given in Table 6) were selected for TEM observation.

Table 6: Samples from the NAS and ABS glass systems chosen for TEM analysis.

Host Glass System	**$GdBr_3$(Ce)-loading**	**Aging Temperature/Time**
NAS	19mol%	Unaged
NAS	19mol%	815°C – 24 hours
NAS	19mol%	815°C – 48 hours
ABS	20mol%	Unaged

TEM specimens were prepared by grinding the sample into a powder using a mortar and pestle, then suspending in deionized water. A carbon-coated copper grid was dipped into the suspension to deposit the powders, and the specimens observed using a JEOL 4000EX high-resolution TEM.

RESULTS

Synthesis

As expected, variations in melting, glass transition, crystallite precipitation, and matrix devitrification temperatures were observed between the three glass systems studied. The temperature required to achieve a single phase melt was higher for the NAS (1450°C) and ABS (1400°C) systems, which were high in alumina, than the NBS system (1350°C). However, the large concentration of scintillating compounds in the ABS system served as an effective fluxing agent, and allowed the ABS system to be processed at lower temperatures than the NAS system, despite its greater alumina content.

The high alumina systems were vulnerable to thermal shock during cooling, which caused many samples to shatter shortly after casting. Higher annealing temperatures and longer dwell periods at the annealing temperature were used to counteract this problem. Addition of B_2O_3 to the melt resulted in marked decreases in annealing temperature from 650°C for the NAS system (0mol% B_2O_3) to 450°C for the NBS system (41mol% B_2O_3). However, due to the lower network free volume of the NBS matrix, the highest concentration of $GdBr_3$-$CeBr_3$ that could be incorporated before loss of transparency was 18mol%, much lower than the over 30mol% achievable in the ABS system.

It was difficult to mix and remove bubbles from the melt because no stirring apparatus was available for the furnace used. Especially in the larger sized batches, this caused a high density of small bubbles to become trapped in the solidified glass, which degraded

energy resolution. To remove bubbles, batches were held for longer dwell times at the melting temperature, but this usually resulted in decreased light yield as the volatile scintillating compounds began to reach their vaporization points and burnoff became a significant problem. Cast samples were also crushed and re-melted under identical conditions in an attempt to further reduce the bubble concentration. While this method was fairly effective at removing some bubbles, complete elimination of bubbles was never achieved and approximately 15g of material was lost in every firing cycle. Fining agents (such as NaF) were also added to reduce the number of bubbles without the need for additional firing steps, and showed reasonable success. As shown by the photographs in *Figure 12*, there were far fewer bubbles in a batch containing NaF and only melted once than the batch that did not contain NaF but was melted twice. Reducing the number of melt/cast cycles was advantageous because roughly 12g of material was lost to the crucible with every firing cycle.

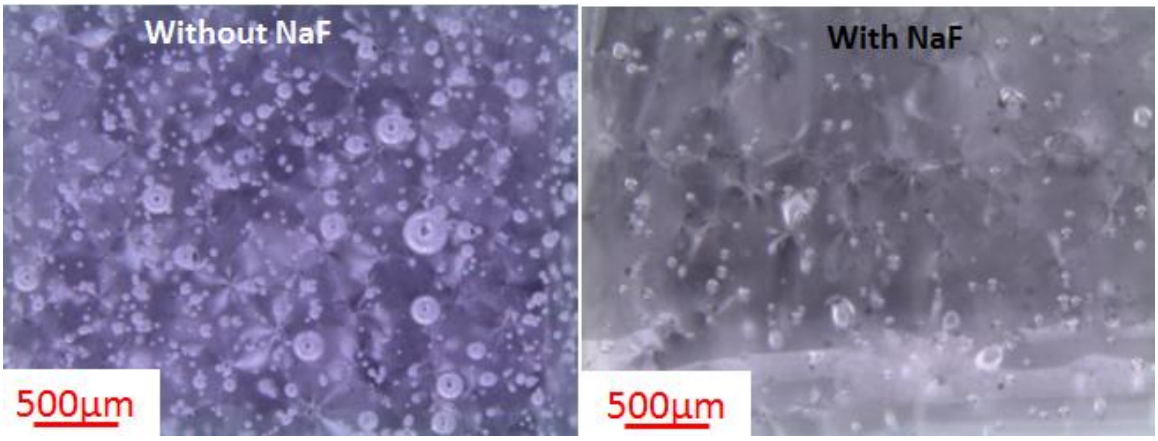

Figure 12: Photographs illustrating the more efficient removal of bubbles when 1wt% NaF fining agent was incorporated into samples from the ABS system (20mol% $GdBr_3$(Ce)). The left image shows a batch that did not contain any NaF and was melted and cast twice. The right image shows a batch that contained 1wt% NaF and was melted and cast once.

Sodium-Aluminosilicate (NAS) System

Photoluminescence Excitation (PLE) and Emission (PL)

PLE/PL scans were performed to observe changes in light yield and shifts in peak emission wavelength as glass composition and ceramization (aging) times and temperatures were varied. Excitation (PLE) and emission (PL) behavior of glasses from the NAS system with the concentrations of scintillating compounds varying between 18mol% and 22mol% using a monitor wavelength of 423nm is shown in *Figure 13*.

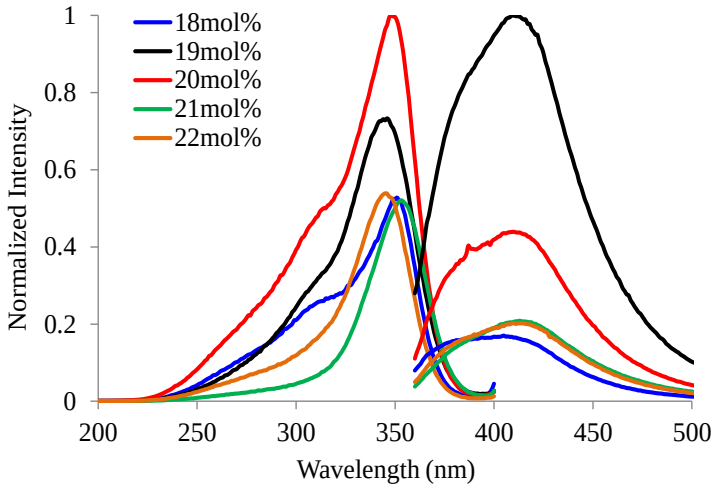

Figure 13: Photoluminescence excitation (PLE) and emission (PL) spectra for glass samples from the NAS system with concentration of $GdBr_3$(Ce) ranging from 18mol% to 22mol% of the precursor batch.

Once the total $GdBr_3$-$CeBr_3$ concentration had been optimized, the doping concentration of $CeBr_3$ in the $GdBr_3$ host crystals was studied. As shown in *Figure 14*, a $CeBr_3$ concentration of 4mol% of the total composition produced the greatest emission intensity.

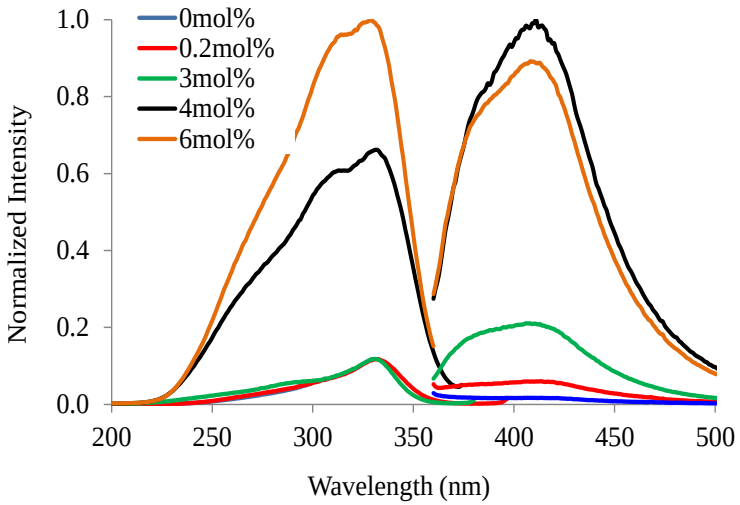

Figure 14: PL spectra for NAS glass samples with $CeBr_3$ concentration ranging from 0-6mol%, with the total $GdBr_3$(Ce) concentration held at 19mol%

The composition NAS-19mol% $GdBr_3$(4mol%Ce) exhibited the highest light yield from the composition optimization study, and so a larger sample of this composition was synthesized for the aging study. Three exothermic peaks at 750°C, 815°C, and 950°C were barely visible above background noise in the DTA trace for this composition (shown in *Figure 15*). Aging studies were carried out at all three temperatures to better characterize the reaction occurring at each.

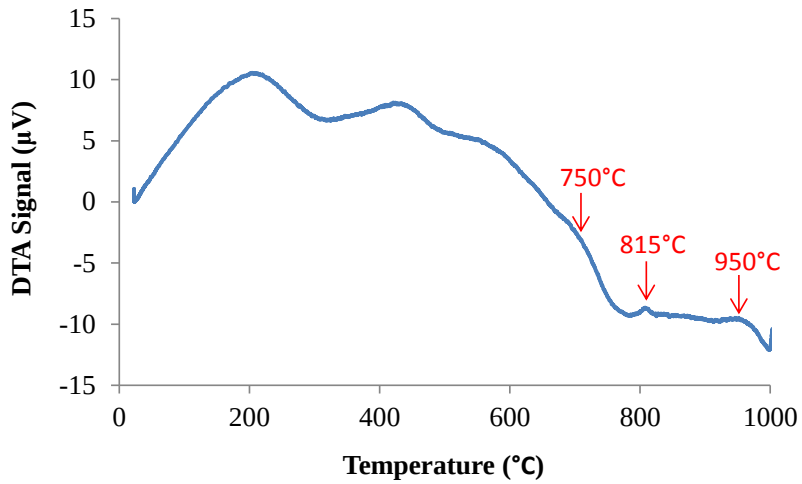

Figure 15: DTA trace showing exothermic peak temperatures used for aging studies in the NAS system. Because the peaks were severely convoluted by background noise, aging studies were performed at each temperature to characterize the phase precipitated.

Shards from the cast boule were aged for 5, 24, and 48 hours at 750°C, and then ground for PL/PLE study. Emission (PL) behavior of these samples is shown in *Figure 16*.

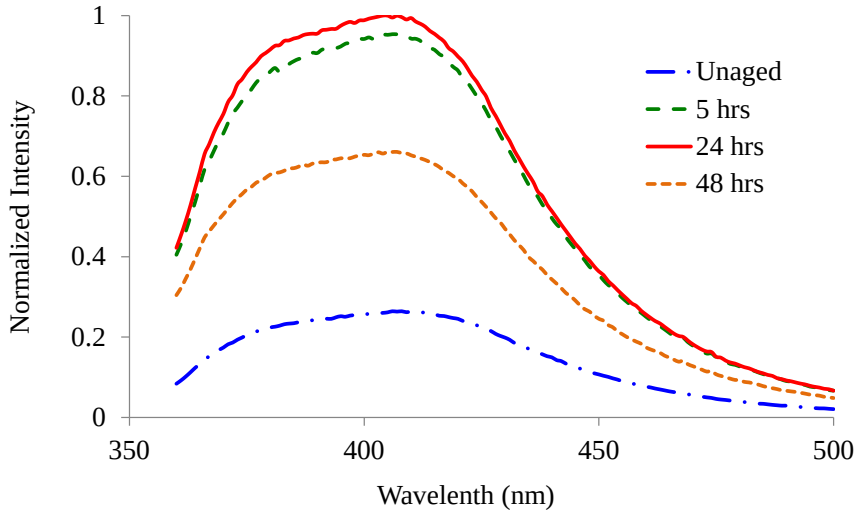

Figure 16: Photoluminescence emission (PL) spectra for shards of NAS 19mol% $GdBr_3$(3mol%Ce) aged from 5-48 hours at 750°C

Emission behavior for samples aged for 24 and 48 hours at 815°C is shown in *Figure 17*.

Note that intensity initially increased with aging, but deteriorated after aging for 48

hours. All three shards were transparent with only a slightly translucent layer visible on the surface of the aged shards, as shown in *Figure 18*.

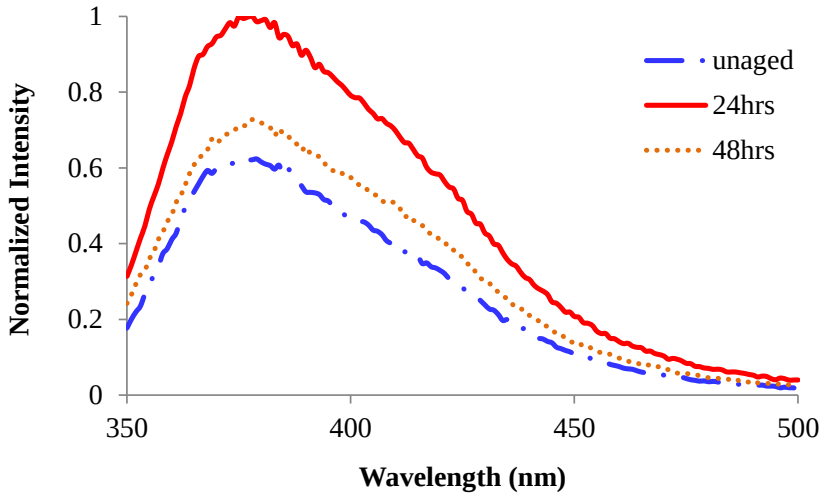

Figure 17: PL spectra for NAS-19mol%$GdBr_3$(3mol%Ce) aged for 24 and 48 hours at 815°C

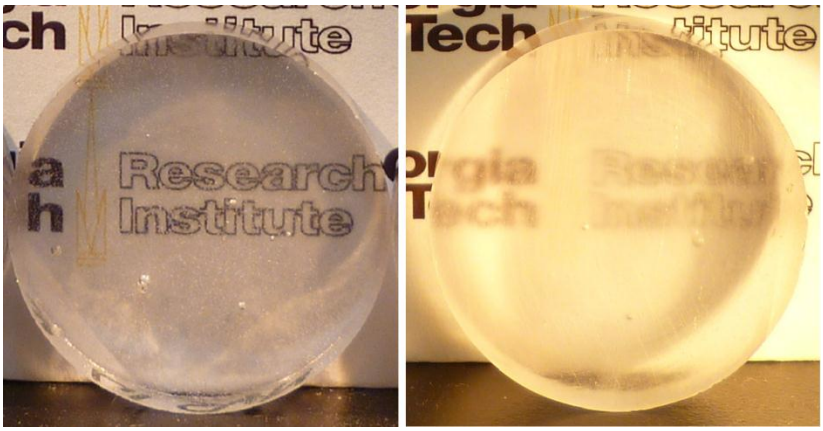

Figure 18: Photograph of disk sectioned from 106g NAS sample. The unaged disk is shown on the left, and after aging for 24 hours at 815°C on the right. The aged disk has a cloudy surface layer indicating that surface crystallization was dominant in this sample.

Finally, emission behavior of the shards aged at 950°C for 4, 8, and 12 hours is shown in *Figure 19*. Samples aged up to 8 hours were transparent, though the sample aged for 12 hours became opaque.

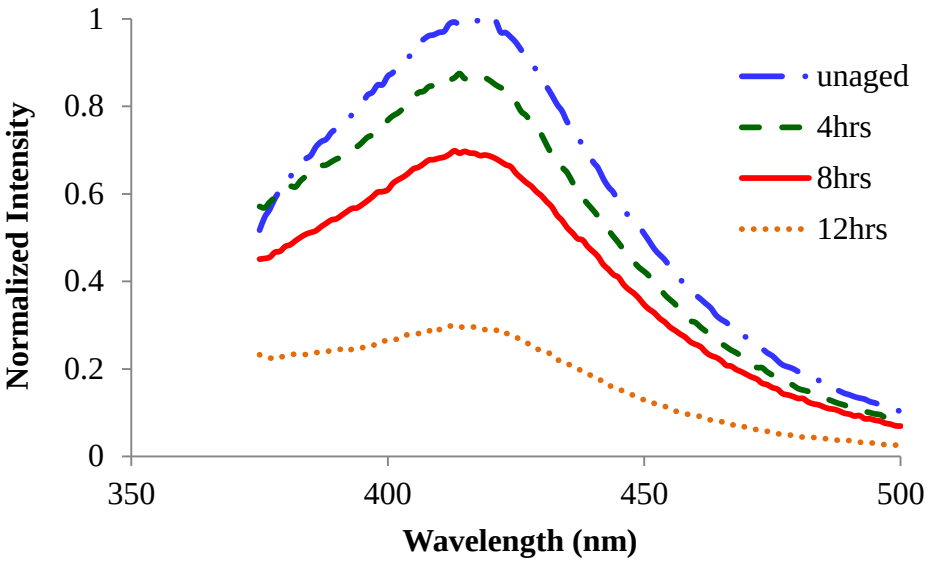

Figure 19: PL spectra for NAS-19mol%$GdBr_3$(Ce) aged for 4, 8, and 12 hours at 950°C

X-Ray Diffraction (XRD)

XRD scans were performed to characterize the crystalline phases precipitated during the ceramization step. Multiple exothermic peaks were observed in the thermal analysis spectrum of the NAS system with 19mol% $GdBr_3$-$CeBr_3$, and so samples were aged at each temperature and the resulting precipitated phases were characterized. The spectra generated by samples aged at 815°C for 24 and 48 hours are shown in *Figure 20*.

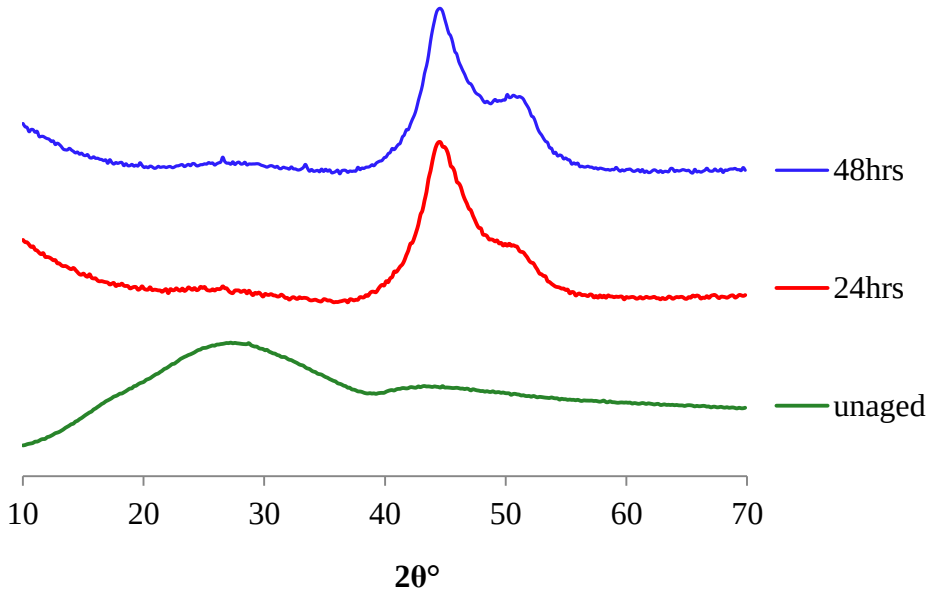

Figure 20: XRD spectra of NAS-19mol% $GdBr_3$(Ce) aged for 24 and 48 hours at 815°C

XRD spectra for the NAS shards aged at 950°C for 4, 8, and 12 hours are shown in *Figure 21*. The sample aged for 12 hours was devitrified and opaque at the end of the aging time while the others remained transparent. The composition of the precipitated phase through the 8 hour aging time most closely corresponds to $Ce_{0.7}Gd_{0.3}O_{1.85}$ (PDF 00-046-0507), though a second, unidentified phase that seems to resemble kyanite (Al_2SiO_5) begins to form at 12 hours. No phases containing bromine were identified, though a list of the PDF reference files whose three most prominent peaks matched those found in the XRD spectra for samples aged in this system are given in Table 7.

Table 7: PDF reference cards that exhibited peak locations similar to the three highest intensity peaks observed in XRD spectra for the NAS system. Not all peaks for these reference phases matched the NAS peak locations exactly.

Reference Phase	**PDF Identification Number**
CeO_2	01-073-7747
Gd_2O_3	01-074-3085
Al_2SiO_5	01-072-1447

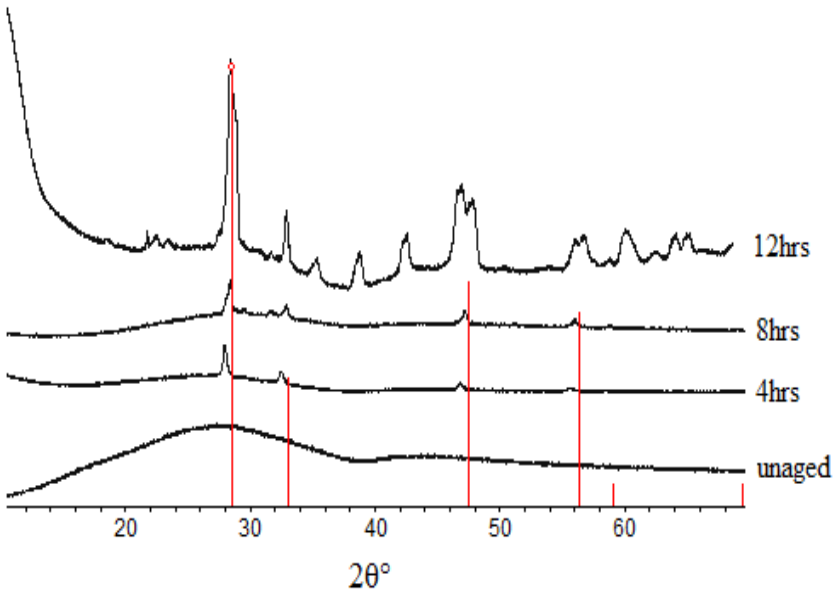

Figure 21: XRD spectra of NAS-19mol% $GdBr_3$(Ce) aged for varying times at 950°C

Radiation Spectroscopy

Batch yields from the composition optimization study of the NAS system were 50g or less, which is prohibitively small for radiation spectroscopy measurements because the gamma-ray range is much larger than the sample dimensions. This means that only a small fraction of the total gamma-ray energy would be absorbed within the dimensions of the scintillator before the gamma-ray escaped. Larger batch sizes of the 19mol% $GdBr_3$(Ce) composition were synthesized to observe effects of aging and scintillator size on energy resolution. As shown in *Figure 22*, increasing the batch size from 48g to 106g yields a narrower photopeak in the ^{137}Cs spectrum, though at a lower channel number and with a more pronounced Compton continuum, suggesting that photon scattering was problematic at the larger batch size.

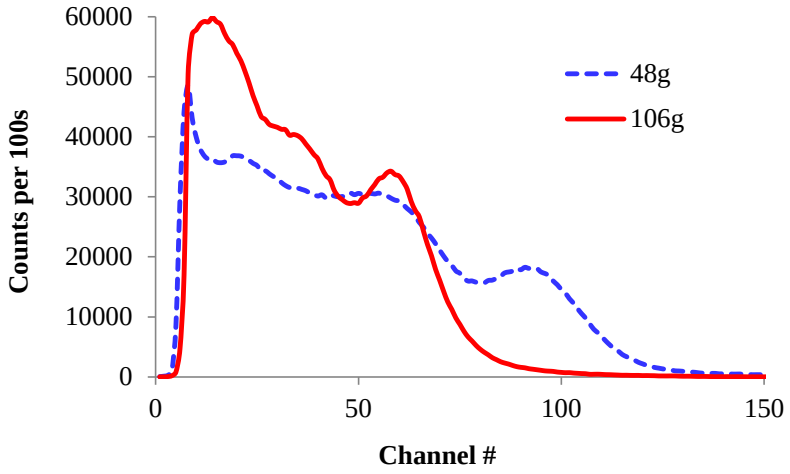

Figure 22: ^{137}Cs spectra generated by 48g and 106g samples of NAS-19mol% $GdBr_3$(Ce)

In contrast, the resolution in the ^{241}Am alpha-spectra (*Figure 23*) was greatly improved by increasing the NAS batch size. A distinct 5.5 MeV photopeak is visible with less scattering present at the lower energy channels for the 106g sample while a photopeak was not visible in the spectrum generated by the 48g sample.

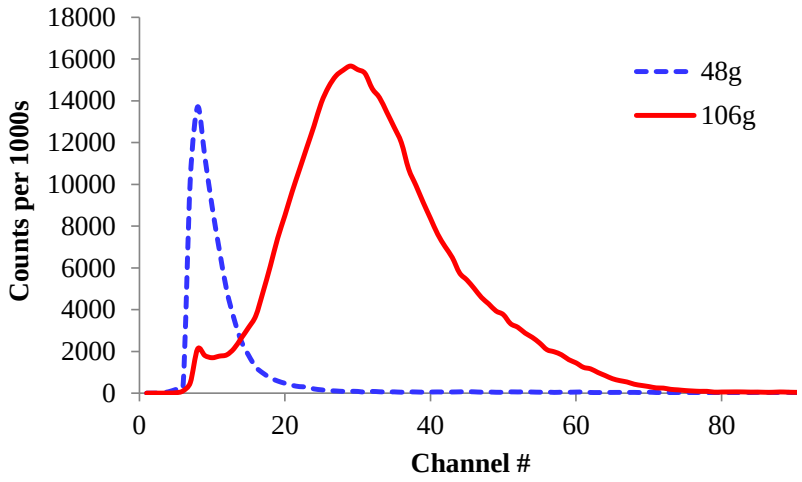

Figure 23: ^{241}Am spectra from 48g and 106g samples of NAS-19mol% $GdBr_3$(Ce)

To determine the degree to which residual thermal stresses in the glass affected emitted photons, the 106g scintillator was annealed at 550°C for 72 and 120 hours, with spectroscopy measurements taken after each cycle. As shown in *Figure 24*, the 5.5 MeV photopeak shifted to higher channel numbers, indicating a higher average number of photons per pulse. It is interesting to note that there was no measureable change in resolution, which remained 32% in both samples. The higher light yield is attributed to reduced photon scattering rather than increased scintillation efficiency from the luminescence centers, and the significant peak shift underscores the importance of ensuring all thermal stresses are relaxed during the annealing step.

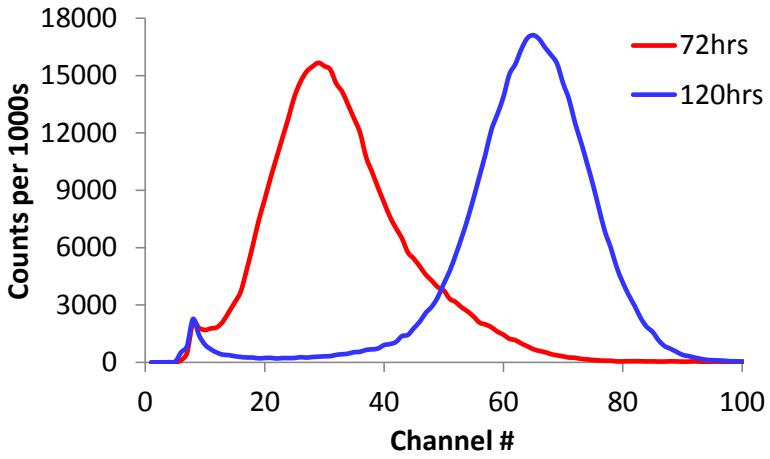

Figure 24: ^{241}Am spectra from 106g NAS sample annealed for 72 and 120 hours at 550°C to observe the effect of thermal stresses on photon scattering

Next, the 106g sample was sectioned into three 1cm disks to characterize sample homogeneity and the effects of ceramization on spectroscopy performance. The ^{137}Cs gamma-ray spectra for the three unaged sections and 106g monolith are shown in *Figure 25*, while the ^{241}Am spectra from the same three disks are shown in *Figure 26*. The

variance between samples in the ^{137}Cs are negligible, though the shifts in peak channel number in the ^{241}Am spectra are of interest.

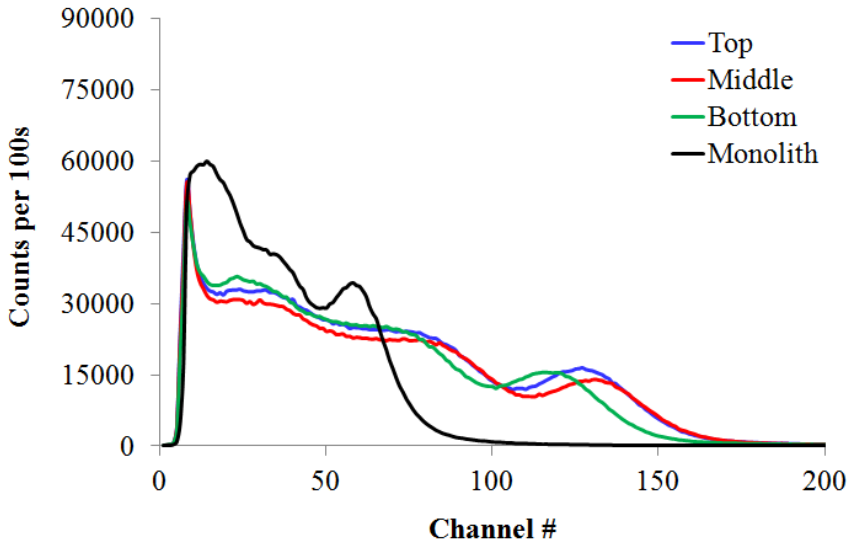

Figure 25: Gamma-ray spectra produced from three sections of NAS-19mol% $GdBr_3(Ce)$. The monolith spectrum is included to show the change in spectroscopy behavior after the 106g sample was sectioned into three disks.

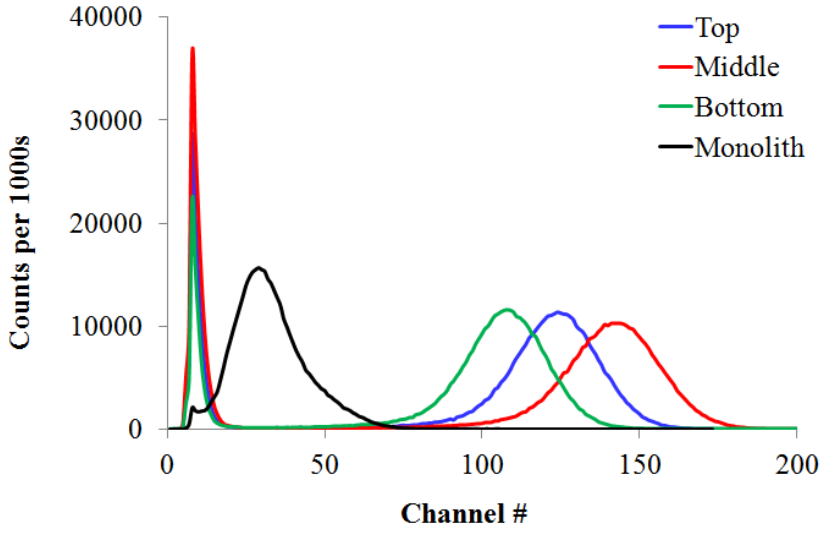

Figure 26: Alpha spectra generated by three sections of NAS-19mol% $GdBr_3(Ce)$

The disks were then aged at 815°C for 24 and 48 hours, with the resulting gamma-ray and alpha-particle spectra shown in *Figure 27* and *Figure 28*, respectively. In the ^{137}Cs spectra, resolution improved from 33% to 27% with aging up to 24 hours, though the photopeak was completely lost in the Compton continuum after aging for 48 hours. While the photopeak location in the alpha-spectra shifted to lower channel numbers after aging for 24 hours, the change in resolution from 24% to 25% was not significant. Similar to the gamma-ray spectrum, the photopeak in the alpha-spectrum became imbedded in the background noise after aging for 48 hours.

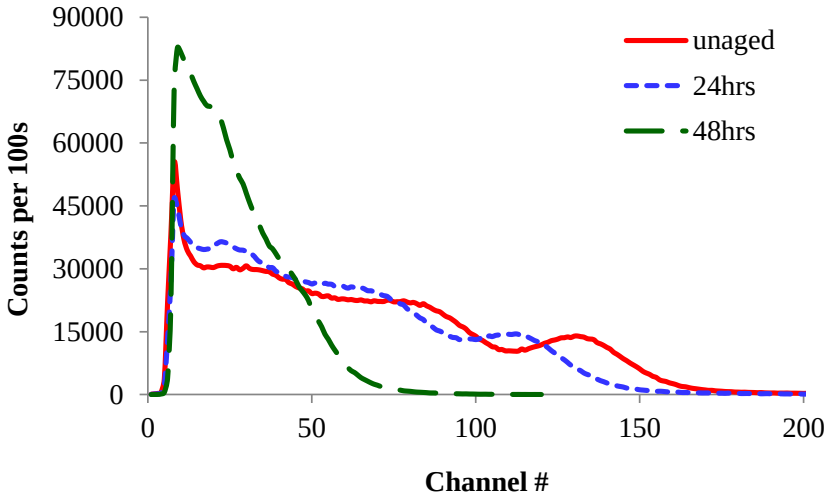

Figure 27: ^{137}Cs spectra generated by NAS disks aged at 815°C for 24 and 48 hours

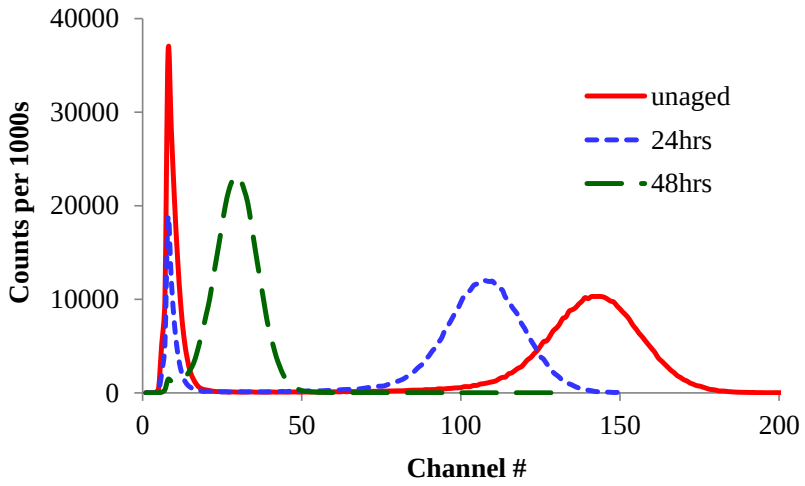

Figure 28: ^{241}Am spectra generated by NAS disks aged at 815°C for 24 and 48 hours

Alumino-Borosilicate (ABS) System

Photoluminescence Excitation (PLE) and Emission (PL)

The alumino-borosilicate base glass composition was adapted from work by Li et. al. [72], who doped Gd_2O_3 into ABS glasses. Li's work showed that there exists and a range of gadolinium concentrations in the host glass that suppresses the formation of mullite at its minimum and prohibits precipitation of gadolinium silicate at its maximum. Three concentrations that fall within this range were chosen (10mol%, 20mol%, 30mol%), and equivalent molar concentrations of $GdBr_3$ and $CeBr_3$ substituted for the Gd_2O_3. The compositions studied are marked by the red dots in the diagram shown in *Figure 5*. The PLE spectra in *Figure 29* show an increase in light yield and a slight shift in peak wavelength (from 317nm to 329nm mto 346nm) as $GdBr_3$(Ce) concentration is increased from 10mol% to 30mol%. The sample with only 10mol% $GdBr_3$(Ce) was opaque because there was in insufficient concentration of fluxing halides to reduce the melting temperature of the more refractory constituents to within the 1450°C processing regime.

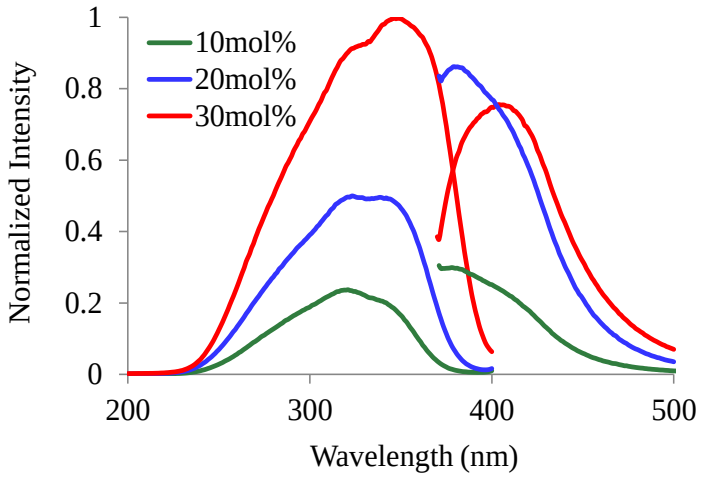

Figure 29: PL/PLE spectra for ABS base glasses with 10mol%, 20mol%, and 30mol% $GdBr_3$(Ce) incorporated into the matrix. Emission intensity appears to decrease slightly from 20 to 30mol%

A batch of ABS with 20mol% $GdBr_3$(Ce) was sectioned into 11cm^3 rectangular coupons for the aging study. The 20mol% $GdBr_3$(Ce) concentration was chosen to allow more direct comparison of behavior of $GdBr_3$(Ce) between the three glass systems. As with the NAS system, the exothermic peaks were convoluted with background noise, and so aging studies were performed at both temperatures. The DTA trace for a sample of an as-cast ABS glass loaded with 20mol% $GdBr_3$(Ce) in the precursor mixture is shown in *Figure 30*.

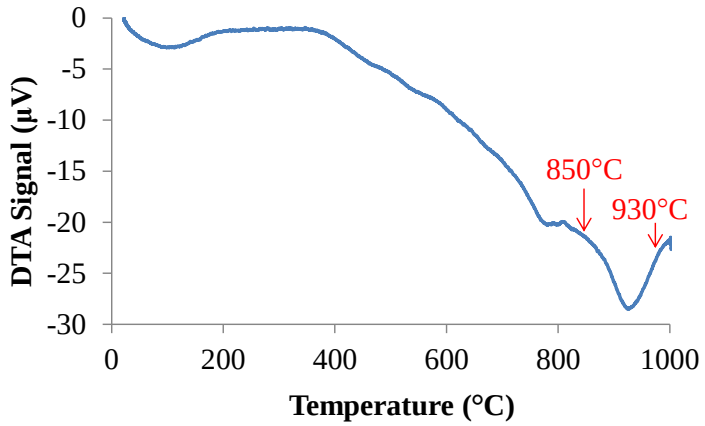

Figure 30: DTA trace of a sample of ABS host glass loaded with 20mol% $GdBr_3$(Ce) in the precursor mixture. Exothermic peaks are not easily visible above the background noise and so aging studies were performed at the two most prominent peak temperatures.

After aging, the billets were ground to powder for characterization studies. The photoluminescence emission behavior of the samples aged at 850°C for 12-96 hours is shown in *Figure 31* and photographs of three of the samples before and after aging are shown in *Figure 32*.

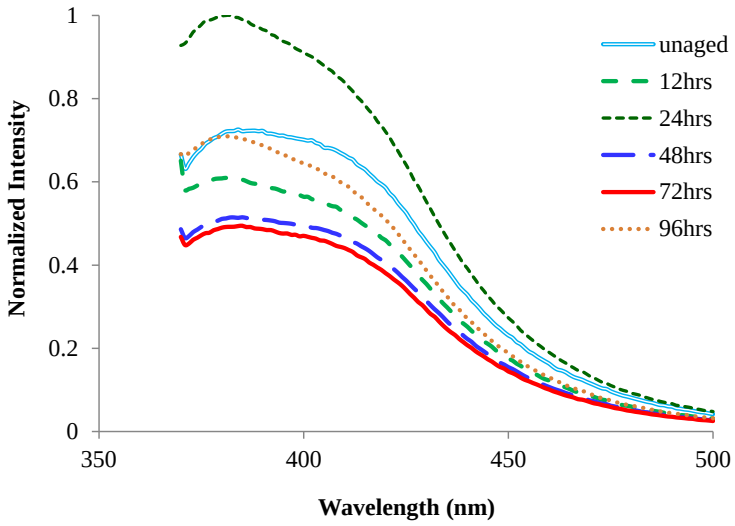

Figure 31: Photoluminescence emission (PL) behavior of ABS-20mol% $GdBr_3$(Ce) billets aged at 850°C for 12-96 hours

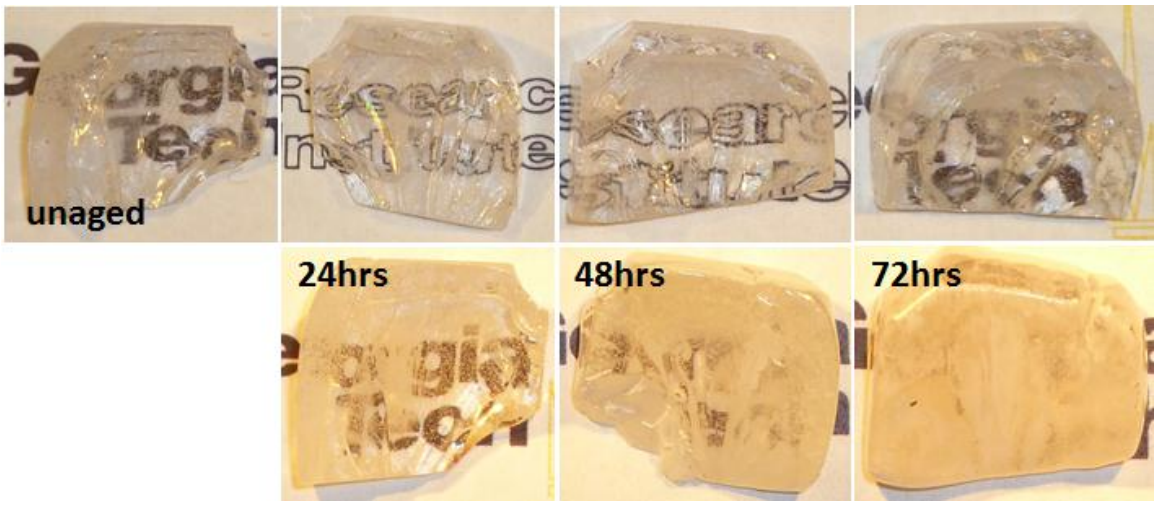

Figure 32: Photographs showing formation of surface crystallites on coupons of ABS-20mol% $GdBr_3$(Ce) during aging at 850°C

The PLE behavior of the ABS samples aged at 850°C is shown in Figure 33. There is no discernible trend between aging time and luminescence intensity, though the sample aged for 24 hours exhibited the highest light yield.

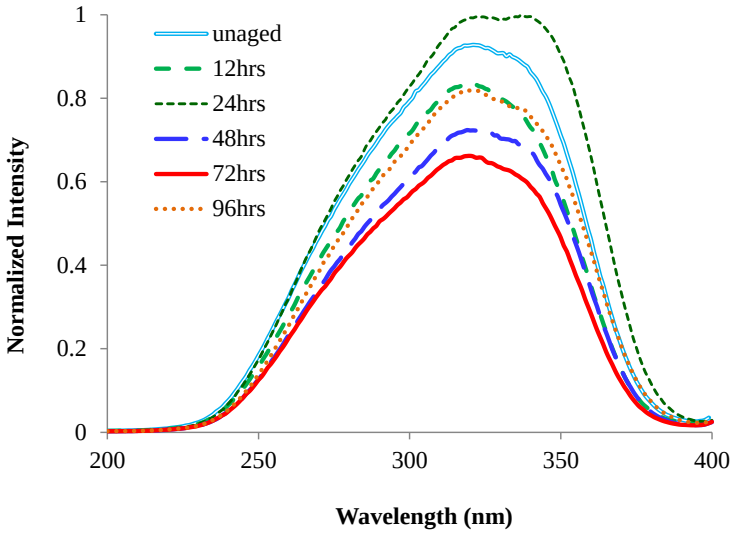

Figure 33: Photoluminescence excitation (PLE) behavior of ABS-20mol% $GdBr_3$(Ce) aged at 850°C for 12-96 hours

As with the NAS system, two exothermic peaks were visible at 850°C and 930°C in the DTA trace of the ABS-20mol% $GdBr_3$(Ce) composition, and so aging studies were performed at both temperatures to observe the different products of reaction. The PL/PLE behavior of samples aged at 930°C is shown in *Figure 34* and *Figure 35*, respectively. Note the significant decrease in luminescence intensity with increased aging time. The inset shows a more detailed view of the emission behavior of the aged samples.

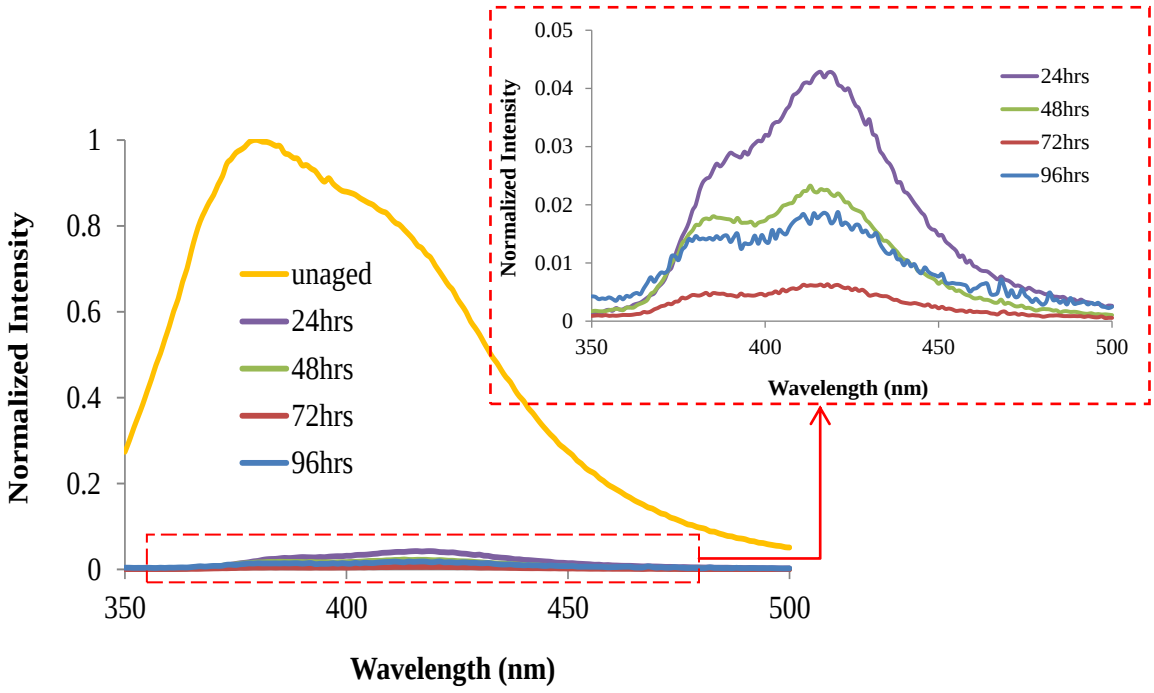

Figure 34: PL spectra for ABS-20mol% $GdBr_3$(Ce) aged at 930°C

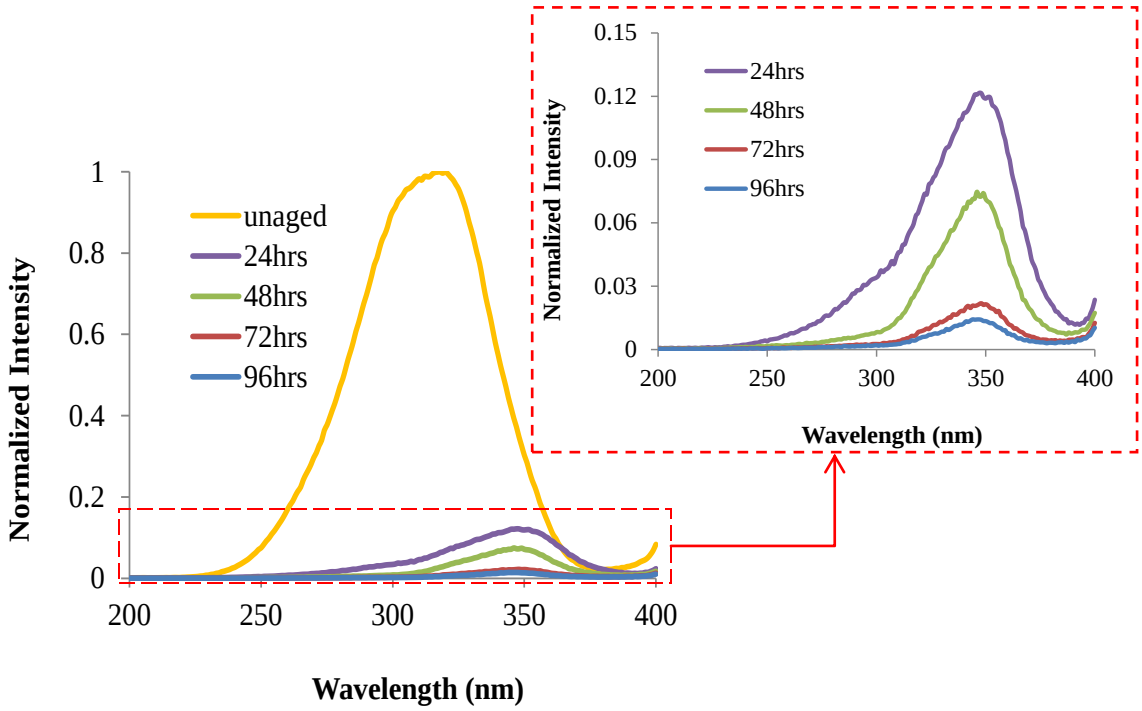

Figure 35: PLE spectra for ABS-20mol% $GdBr_3$(Ce) aged at 930°C

X-Ray Diffraction (XRD)

XRD spectra of ABS billets (20mol% $GdBr_3$(Ce)) aged at 850°C for 12 to 96 hours are shown *Figure 36*. Scan times were increased to 12 hours, which was much longer than the 1 hour scan times used in other specimens. Samples aged at 850°C and scanned for only one hour did not generate XRD peaks, as shown by the spectra in the upper half of *Figure 36*. The highest intensity peaks correspond to a $GdBO_3$ phase (shown by the red reference peaks), with the lower intensity (blue reference) peaks corresponding to $Gd_{0.6}Ce_{0.4}O_{1.70}$.

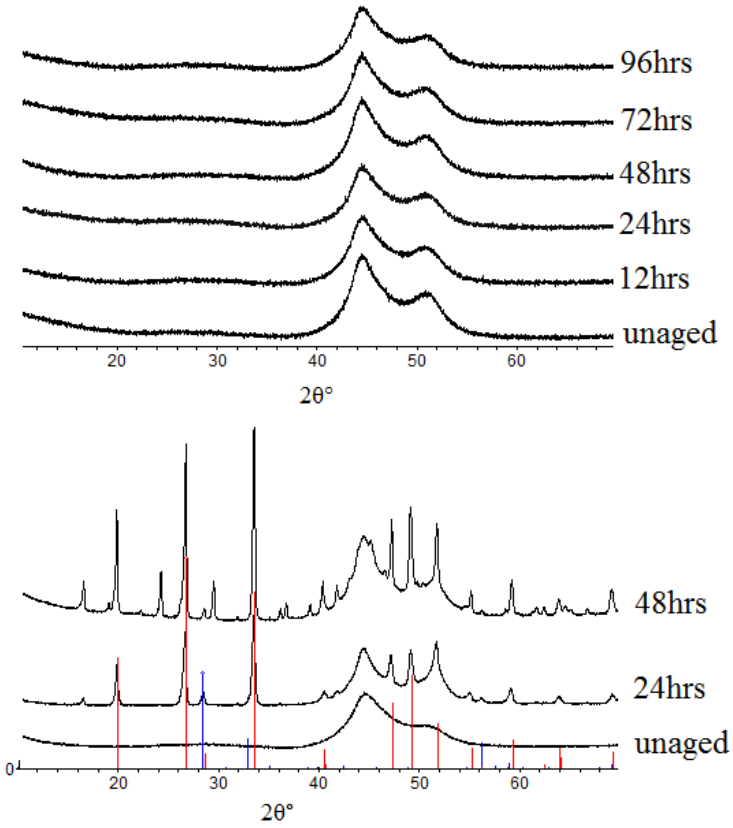

Figure 36: XRD spectra of ABS-20mol% $GdBr_3$(Ce) aged for varying times at 850°C. The top spectrum was acquired using a scan time of 1 hour, while the lower spectra were acquired using a scan time of 12 hours. The red PDF overlay in the lower spectra is the $GdBO_3$ phase (PDF 04-010-9111) and the blue overlay is the $Gd_{0.6}Ce_{0.4}O_{1.70}$ phase (PDF 01-073-3587)

As shown in *Figure 37*, the XRD spectra for samples aged at 930°C had more peaks visible than the spectra for samples aged at 850°C. The peak locations most closely correspond to a gadolinium borate phase (PDF 04-010-9111), although the luminescence intensity decreases with longer aging time. The shards aged for longer than 24 hours developed a translucent surface layer that was easily removed during lapping and polishing of the sample. These layers illustrate the affinity for crystallites to precipitate preferentially on the surface, which may have created a non-uniform spectroscopy response.

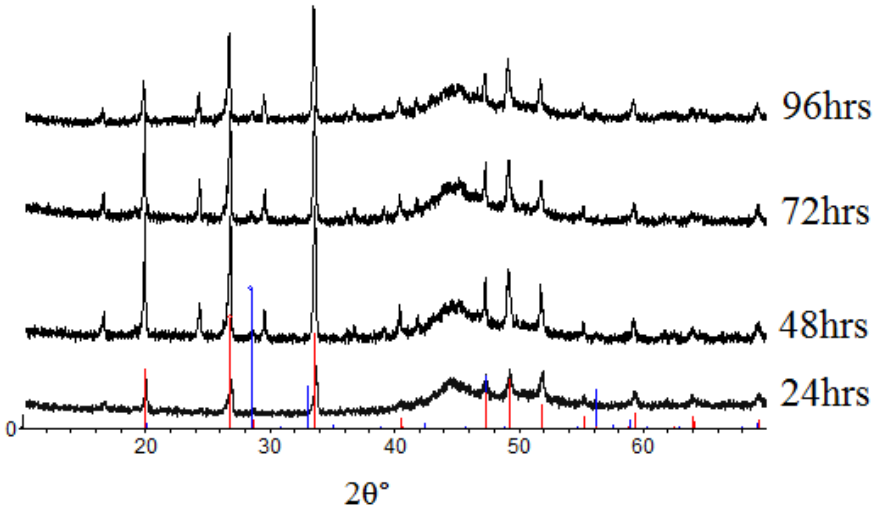

Figure 37: XRD spectra for ABS-20mol%$GdBr_3$(Ce) samples aged at 930°C with $GdBO_3$ (PDF 04-010-9111in red) and $Gd_{0.6}Ce_{0.4}O_{1.70}$ phase (PDF 01-073-3587 in red) reference peaks overlaid.

Radiation Spectroscopy

Gamma-ray spectra produced by the ABS glass system loaded with 20mol% and 30mol% $GdBr_3$-$CeBr_3$ are shown in *Figure 38*, with the corresponding alpha-spectra shown in *Figure 39*. The 20mol% $GdBr_3$(Ce) sample produced a gamma-ray photopeak resolution of 35% and the 30mol% sample a resolution of 38%, though with a much greater light yield. In the alpha-spectra, the resolution from the 20mol% $GdBr_3$(Ce) sample was 38% while the resolution from the 30mol% samples was 89%.

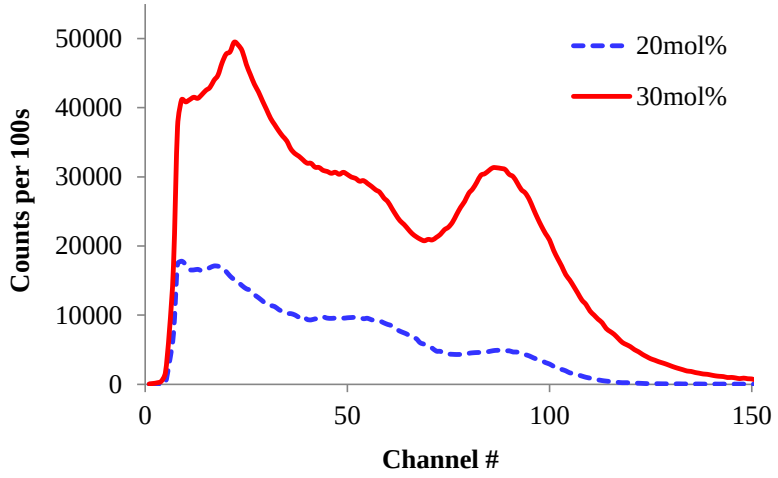

Figure 38: ^{137}Cs spectra generated by ABS glass doped with 20mol% and 30mol% $GdBr_3$(Ce)

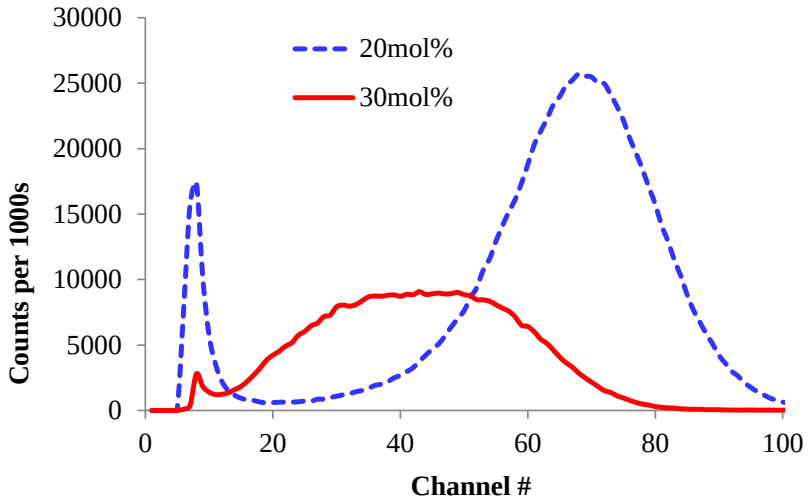

Figure 39: ^{241}Am spectra generated by ABS glass doped with 20mol% and 30mol% $GdBr_3$(Ce)

Three different batch sizes (54g, 68g, and 127g) were synthesized for the ABS-30mol% $GdBr_3$(Ce) system. Variations in the quality of the gamma-ray and alpha-particle spectra for the three different sizes are shown in *Figure 41* and *Figure 40*, respectively, with their corresponding energy resolutions given in Table 8. The 68g sample exhibited finer

energy resolution, though the 127g sample produced a higher light yield, which suggests that photons experience significant scatter or escaped before passing to the PMT.

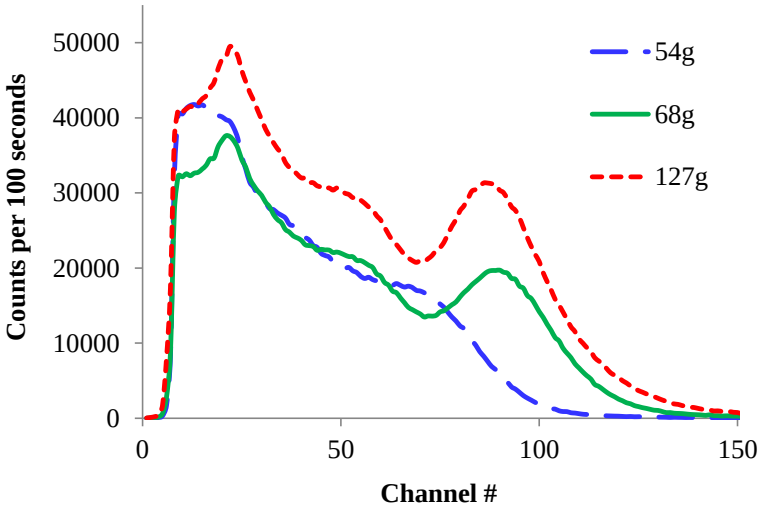

Figure 40: ^{137}Cs spectra generated by ABS-30mol% $GdBr_3$(Ce) of varying sizes

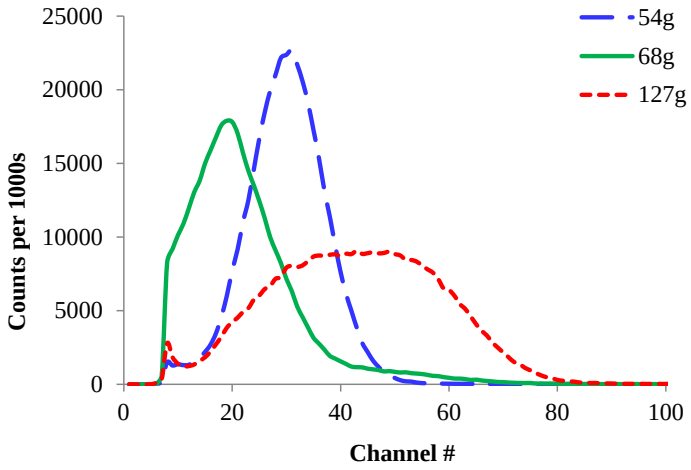

Figure 41: ^{241}Am spectra generated by ABS-30mol% $GdBr_3$(Ce) of varying sizes

Table 8: Photopeak energy resolution from ABS glass samples of varying size loaded with 30mol% $GdBr_3(Ce)$

Sample Mass	**^{241}Am Resolution**	**^{137}Cs Resolution**
54g	45%	No peak visible
68g	53% (peak cutoff in noise)	35%
127g	89%	38%

Formation of bubbles within the glass melt and their subsequent entrapment in the cooled piece caused significant photon scattering, which resulted in a more pronounced Compton continuum and degraded energy resolution (from 38% to 40%), as shown by the spectra in *Figure 42*. This further underscores the importance of incorporating a fining agent to eliminate bubbles.

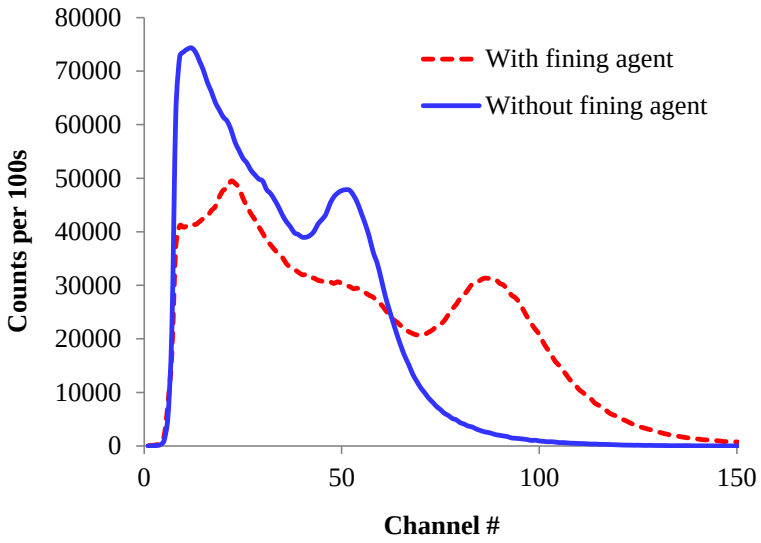

Figure 42: ^{137}Cs spectra for ABS glasses loaded with 30mol% $GdBr_3(Ce)$. One of the batches was also loaded with 1wt% NaF to act as a fining agent and reduce the bubble concentration

Bubbles also degraded the resolution of the alpha-spectra. A majority of the spectrum from the batch without added fining agents (seen in *Figure 43*) was overshadowed by the

background noise, while a photopeak with 28% resolution emerged in the spectrum with fining agent.

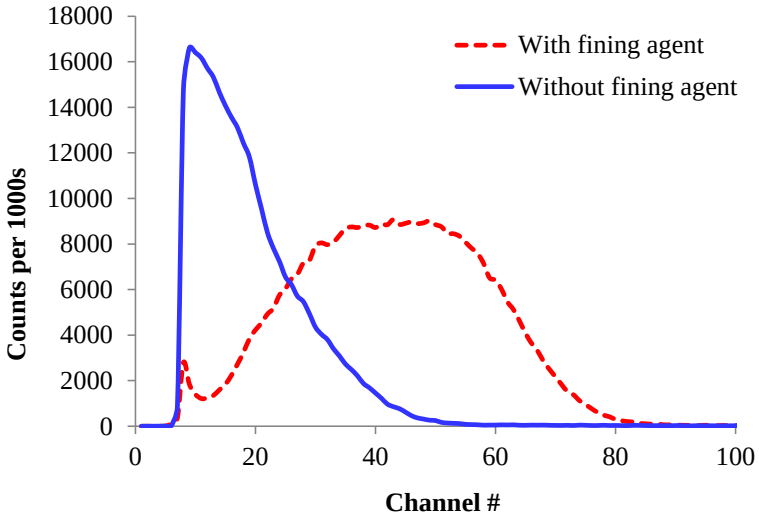

Figure 43: ^{241}Am spectra for ABS glasses loaded with 30mol% $GdBr_3$(Ce) both with and without added NaF as a fining agent

Disks sectioned from the ABS system for the aging portion of the study were not large enough to accommodate radiation spectroscopy measurements, and so spectroscopy data for aged samples in this system is not available.

Sodium-Borosilicate (NBS) System

Photoluminescence Excitation (PLE) and Emission (PL)

The PL/PLE behavior of scintillators from the NBS composition with $GdBr_3$(Ce) concentrations ranging from 7-15mol% is shown in *Figure 44*. There does not appear to be an obvious relationship between $GdBr_3$(Ce) concentration and light yield in either set of luminescence spectra.

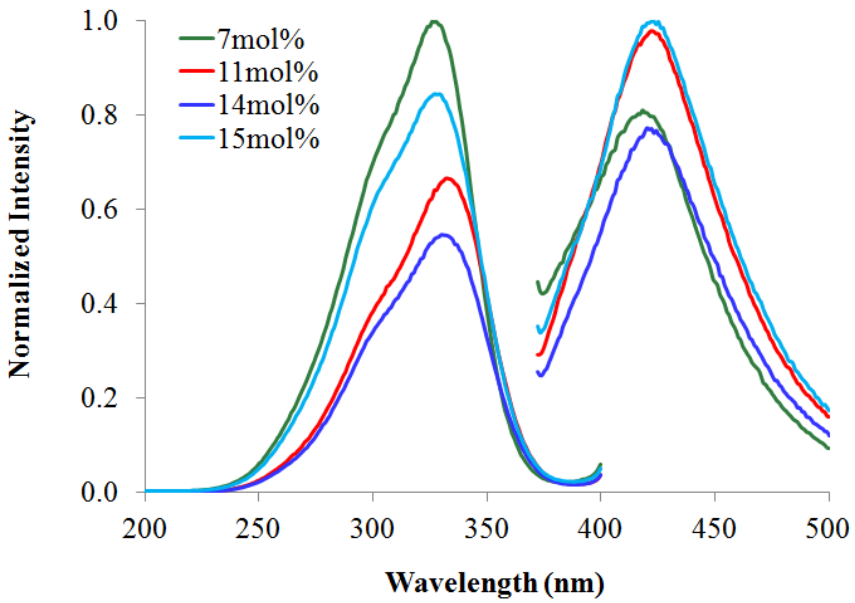

Figure 44: PL/PLE behavior of NBS glass system doped with 7-15mol% $GdBr_3$(Ce)

Radiation Spectroscopy

Batch sizes greater than 20g were not achievable in the NBS system, and samples that were fabricated showed far inferior spectroscopy performance relative to the NAS and ABS systems, as shown by the gamma-ray and alpha-particle spectra in *Figure 48* and *Figure 49*, respectively. The low solubility of scintillating compounds achievable in this glass system and poor spectroscopy performance prohibited further investigation of this glass system.

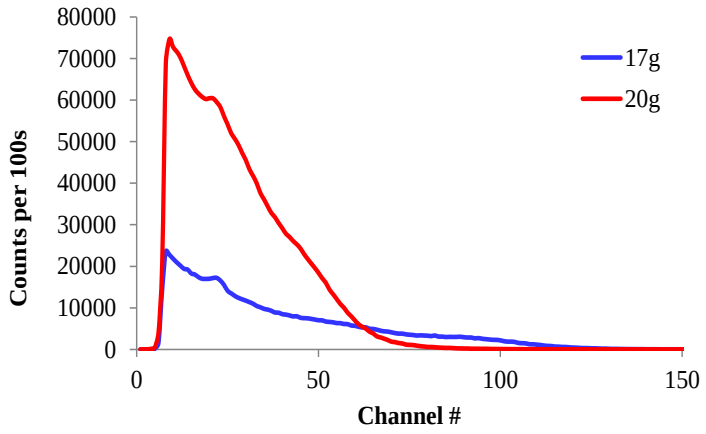

Figure 45: Gamma-ray spectra produced by two samples from the NBS system. The 662keV photopeak is not visible and the Compton continuum dominates.

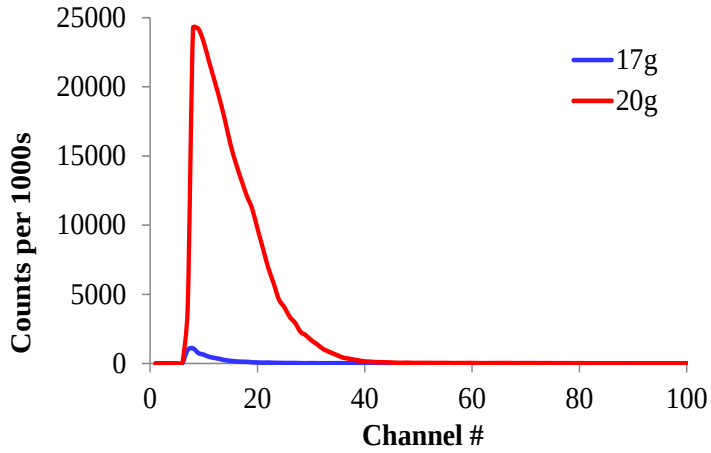

Figure 46: Alpha-particle spectra produced by the NBS system. The scattering region is pronounced with no visible photopeak

Systems Comparison

Photoluminescence Excitation (PLE) and Emission (PL)

The PLE behavior across the three glass systems is compared in *Figure 47*. Note the considerably higher light yield of the ABS system compared to both the NAS and NBS systems.

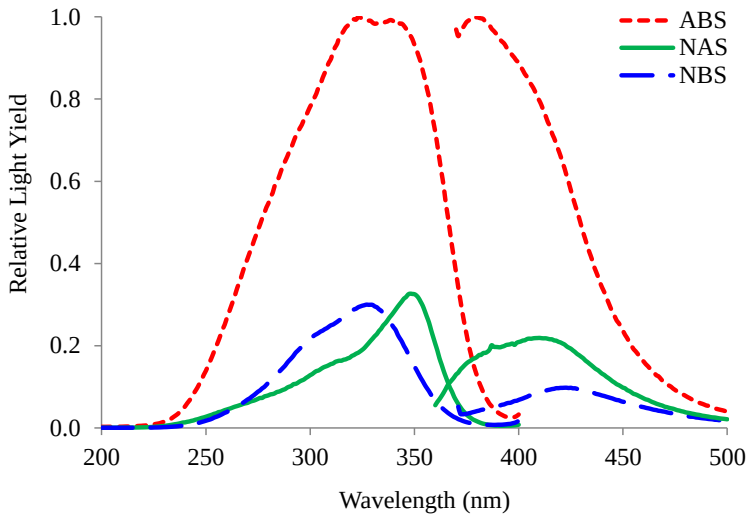

Figure 47: PLE/PL spectra produced by 20mol% $GdBr_3$(Ce)-doped NAS and ABS glass systems (15mol% in NBS) under 423nm monitor wavelength for PLE and 350nm excitation wavelength for PL and 423nm monitor wavelength for PLE

Radiation Spectroscopy

A comparison of the gamma-ray and alpha-particle spectroscopy performance of larger volume scintillators from the three different glass systems is shown in *Figure 48* and *Figure 49*, respectively, with the corresponding energy resolutions given in Table 9. A smaller achievable scintillator size (20g vs. 106g and 127g) likely contributes to the degraded performance of the NBS system relative to the other two.

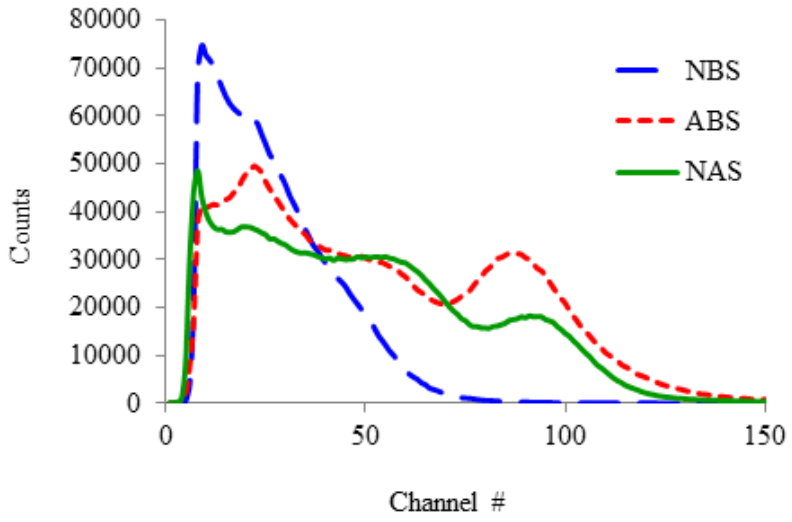

Figure 48: Gamma-ray spectra for ^{137}Cs generated by large volume samples

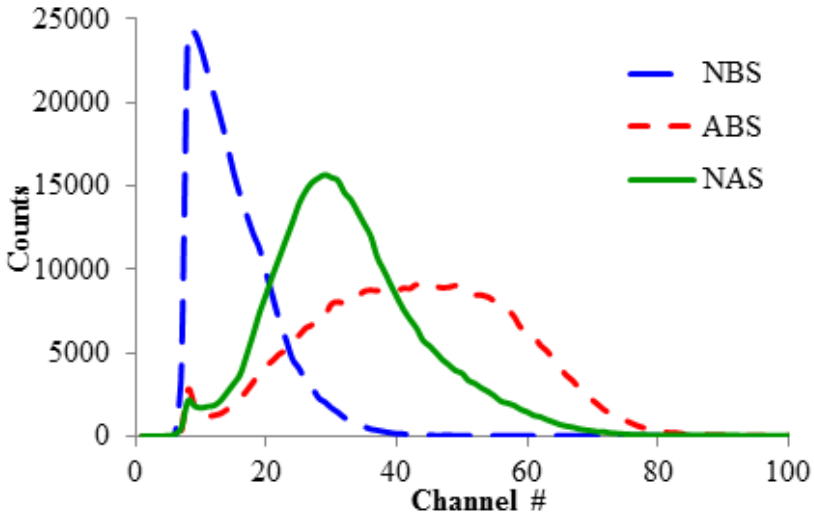

Figure 49: Alpha-particle spectra for ^{241}Am generated by large volume samples

Table 9: Energy resolution produced by samples from each glass system

Glass System	**^{241}Am Resolution**	**^{137}Cs Resolution**
NBS	No peak visible	No peak visible
ABS	89%	30%
NAS	32%	34%

DISCUSSION

Sodium-Aluminosilicate (NAS) Series

In the NAS system, emitted light yield increased with the concentration of scintillating compounds ($GdBr_3$ and $CeBr_3$) until the loading reached 19mol% of the glass batch. Subsequent additions reduced glass transparency and showed a slight increase in refractive index from 1.580 to 1.588 as loading increased from 19mol% to 22mol%. Such a trend is expected as the density of the glass increases with the higher concentration of heavy rare-earth elements [92]. The rare-earth halides also acted as a fluxing agent to the more refractory compounds, which reduced network connectivity and created additional non-bridging oxygen (NBO) atoms in the glass network. A higher concentration of NBO's in the glass increased the polarizability, and therefore the refractive index, of the glass network. While the higher refractive index reduced the tendency for photons to escape the glass matrix [93], it may have also increased the probability for photon scattering and absorption.

Figure 50: Photographs showing glass samples with A) 19mol% $GdBr_3$-$CeBr_3$, and B) 22mol% $GdBr_3$-$CeBr_3$.Transaprency began to decrease with $GdBr_3$-$CeBr_3$ additions past 19mol% until the glass began to turn black at 22mol% $GdBr_3$-$CeBr_3$.

The increase in refractive index was accompanied by a sharp drop in light yield, as shown in **Error! Reference source not found.**, with a similar effect seen upon increasing the concentration of cerium doped into the $GdBr_3$ host crystals, shown in *Figure 14*. In this case, light yield continued to increase up to a cerium concentration of 4mol%, with a decrease in intensity starting at 6mol%. This value fits well with the 3mol% reported in previous studies of Ce^{3+} additions to silicate glasses [94]. Additions past 4mol% $CeBr_3$ mark the onset of concentration quenching as ionic separation distance between neighboring luminescent centers becomes sufficiently small to allow cross-relaxation and re-absorption of emitted photons [95]. Although he studied $LaBr_3$(Ce) single crystals rather than $GdBr_3$(Ce) nanocomposites, Drozdowski reported a similar concentration quenching effect while optimizing the crystal composition (*Figure 51*). This result is particularly interesting because concentration quenching in a NaI(Tl) begins at 0.2mol% thallium-doping. Segregation of the luminescent centers into the nanocrystals likely inhibits clustering and thus reduce re-absorption of emitted photons by neighboring ions [96].

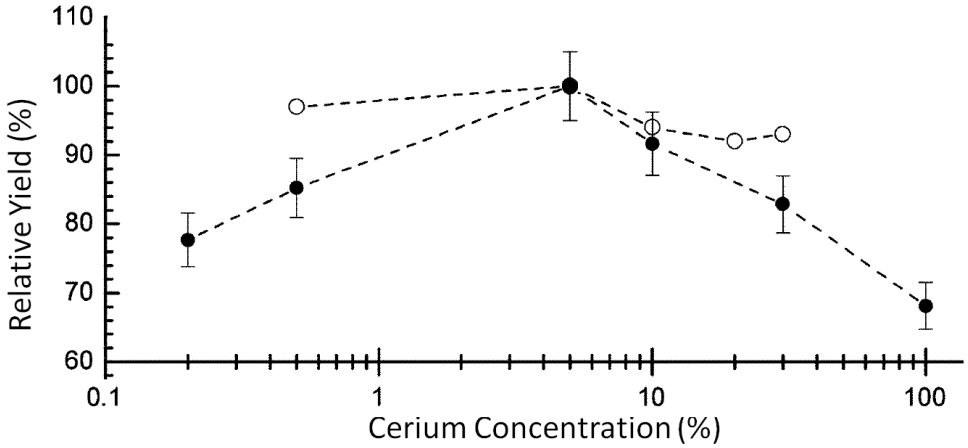

Figure 51: Data showing how light yield is reduced past a certain cerium concentration in a phenomenon known as concentration quenching [31]

To ensure luminescent centers are well-separated and the concentration quenching effect is minimized, a high density of crystal nuclei should be formed during melt quenching. The higher nuclei density creates greater competition for precipitating compounds during crystal growth, and thus limits precipitated particle sizes to 50nm or less [57]. The smaller crystallite sizes are desirable because the transfer of absorbed radiation energy from the non-radiative glass host to embedded luminescent crystals has been shown to become less efficient as crystal size increases [67]. The decrease in efficiency is attributed to an increased probability of trapping by non-radiative quenching sites, such as surfaces, interfaces, or vacancies [97], or a reduced number of luminescent centers available for energy transfer as a larger fraction of the centers are found farther into the interior of the crystal. Thus, a uniform distribution of smaller (<50nm) crystallites may exhibit superior performance relative to a glass-ceramic whose average crystallite size is larger and more heterogeneously dispersed. However, a larger fraction of luminescent ions will be located near the glass-crystal interface as crystallite size decreases, which

would create a higher phonon environment that could quench luminescence [67], [98]. Thus, there is likely an ideal crystallite size in the range of 20-50nm.

For samples of the NAS glass (19mol% $GdBr_3$-$CeBr_3$) aged at 750°C (*Figure 16*), light yield increased with aging time up to 24 hours, past which continued aging began to degrade intensity. A similar effect was seen when ceramization was carried out at 815°C (*Figure 17*). While variations in luminescence intensity were apparent at these aging temperatures, there were no peaks visible in the associated XRD spectra to explain the discrepancies. This may be because the volume fraction of the crystalline phase precipitated at these temperatures was too low to be distinguished above the background noise. However, the images shown in *Figure 18*, copied below for convenience, of the center disk prior to aging (left) and after aging for 24 hours at 815°C (right), indicate that surface crystallization may have been the dominant reaction in this sample [99], [100]. When a small segment is ground from this disk for powder XRD, only a small fraction of the sample would be crystallized. An alternative explanation may be that 815°C represents a strain point rather than a precipitation reaction, with increased light yield resulting from decreased scattering to due variations in refractive index through the sample bulk.

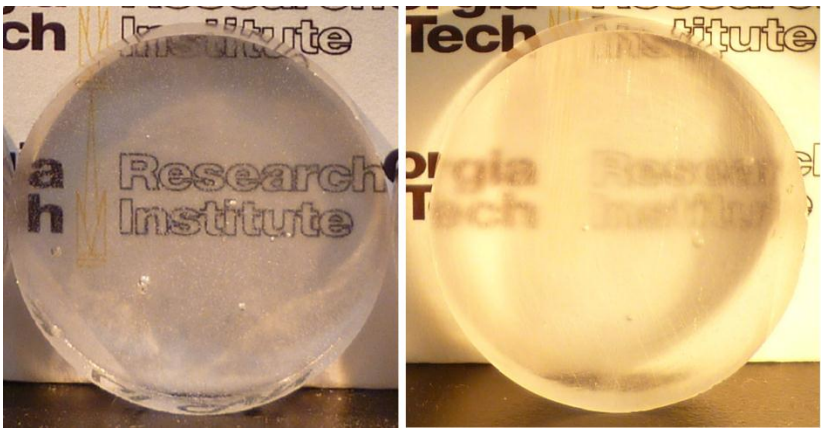

Figure 18 (copied from above): Photograph of disk sectioned from 106g NAS sample. The unaged disk is shown on the left, and after aging for 24 hours at 815°C on the right. The aged disk has a cloudy surface layer indicating that surface crystallization was dominant in this sample.

The surface crystallization argument is supported by SEM studies of the glass samples aged at 750°C. Pieces from the sample aged for 48 hours at 750°C were mounted directly on the SEM stage without lapping or polishing. The average crystallite size is approximately 50nm, though this phase was not detected during powder XRD scans.

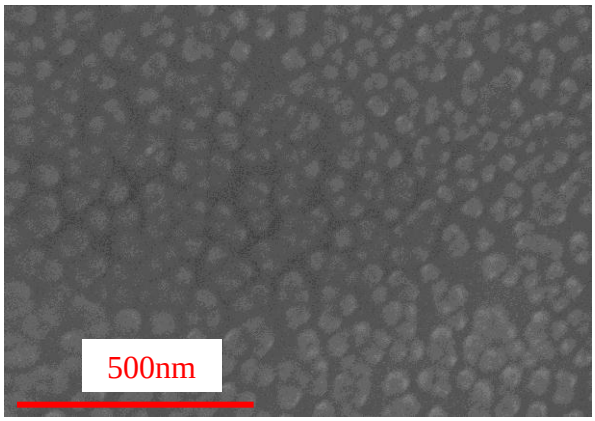

Figure 52: SEM micrograph showing surface crystallites formed in the NAS glass during aging at 750°C. These crystallites were not detected in XRD scans and did not appear in SEM analysis after being lapped and polished.

Aging at 950°C resulted in immediate and rapid degradation of light yield with aging time (*Figure 19*), though XRD analysis identified a $Ce_{0.7}Gd_{0.3}O_{1.85}$ phase composition.

Glass shards aged longer than 8 hours at this temperature became white/opaque, though from the corresponding XRD spectra in *Figure 21*, it is unclear whether the size of the Ce-Gd-O precipitated crystals caused opacity or if the second (unidentified) phase that formed is to blame. However, the SEM images in *Figure 53* show large crystals with plate-like morphology with a second needle-like phase interspersed as well. The average size of the plate-like crystals is clearly larger than 100nm, and so this phase was probably the most significant contributor to loss of transparency in the glass upon aging at 950°C. Work by Nikl [65] has shown that higher aging temperatures allow solute to diffuse over longer distances to the growing crystal, thus producing larger precipitates. When these precipitates begin to exceed 100nm in diameter, scattering can become significant for both the 350nm photons emitted and visible light.

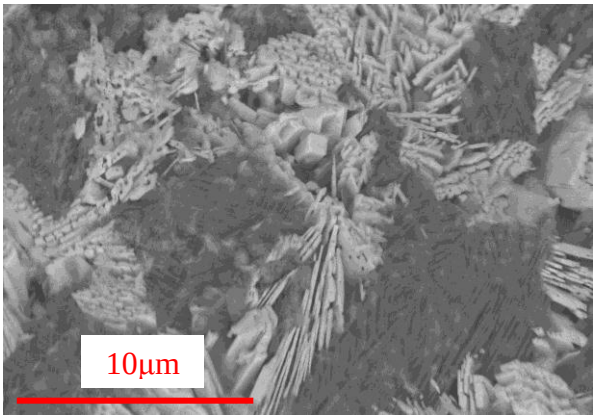

Figure 53: SEM micrograph of a sample of NAS glass (19mol% $GdBr_3$(Ce)) aged for 12 hours at 950°C. The large, plate-like crystallites contributed to loss of sample transparency and seem to correspond to a Al_2SiO_5 phase based on XRD analysis.

Although batch sizes produced during the composition optimization study were prohibitively small for spectroscopy measurements, variations in gamma-ray spectroscopy behavior with increasing sample volume were intriguing. As seen in *Figure*

22, when scintillator size was increased from 48g to 106g, the photopeak resolution was somewhat degraded from 27% in the 48g sample to 34% in the 106g sample. The 662keV photopeak also shifted to lower channels, indicating a lower light yield per pulse, and the Compton continuum became more pronounced in the larger sample. This indicates that photon scattering became a significant in the larger sample, and was most likely caused by residual thermal stresses and trapped bubbles. *Figure 54* shows the large number of bubbles trapped in the 106g NAS sample. However, the photopeak resolution in the alpha-particle spectrum produced by the 106g sample (32%) is far superior to the spectrum produced by the 48g sample, in which a photopeak was not visible. The larger scintillator was expected to show poorer alpha-resolution because of the increased probability for escape of near-surface photons or photon scattering in a larger sample [35]. The cause of this deviation is, as of yet, unclear, but will be the topic of future investigations.

Figure 54: Photo of 106g sample of 19mol% $GdBr_3$(Ce)-loaded NAS glass. The high density of bubbles likely contributed to significant photon scattering

Non-uniform composition through the sample bulk can also degrade photon yield, and so the 106g glass cylinder was sectioned and characterized to determine if such a defect

played a significant role in this system. Three, 1cm thick disks (shown in *Figure 55*) were sectioned and spectra acquired for each disk separately to characterize the uniformity in optical response along the scintillator axis. The resulting behavior, seen in *Figure 25* and *Figure 26*, shows some variation in optical behavior between the three disks, with resolution varying from approximately 28-35% in the gamma-ray spectrum and 24-25% in the alpha-particle spectrum. However, the bottom disk (shown on the far right) had several large bubbles trapped in the interior and showed less intense luminescence, which likely limited the achievable energy resolution in the gamma-spectra.

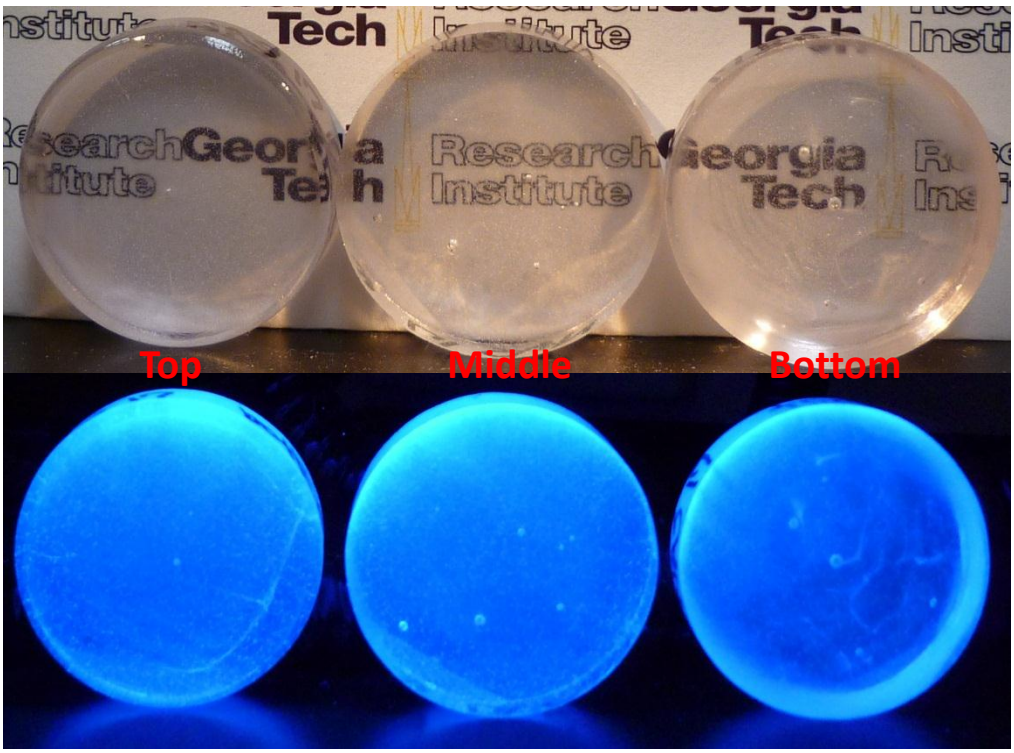

Figure 55: Disks sectioned from the 106g NAS sample under ambient (upper) and UV exposure (lower). The bottom disk (right) has two large trapped bubbles, which likely contributed to this disks lower energy resolution.

The negligible variations in the alpha-spectra indicate that the melt and resulting cast glass were of homogeneous composition. Two of the disks were then aged for 24 and 48

hours at 815°C and then characterized. The gamma-ray energy resolution (*Figure 25*), improved slightly from 33% to 27% in the sample aged for 24 hours, though the photopeak shifted to lower channel numbers, which indicates decreased light yield per pulse. The resolution for the sample aged for 48 hours was not determined because the photopeak was reduced to a small shoulder above the Compton continuum. The alpha-spectra resolution changed negligibly from 24% to 25% after aging for 24 hours, and the decrease in light yield was also less pronounced than in the gamma-spectra. The photopeak was again lost in the background noise of the 48 hour spectrum.

When TEM analysis was performed on samples aged for 24 and 48 hours at 815°C, clusters of crystallites were distinctly visible in the powders aged for 48 hours (*Figure 57*), while very few crystallites were found in the sample aged for 24 hours (*Figure 56*). This agrees with the trend seen in XRD analysis, though further study will be needed to fully describe the kinetics of the precipitation of rare-earth crystallites in this system.

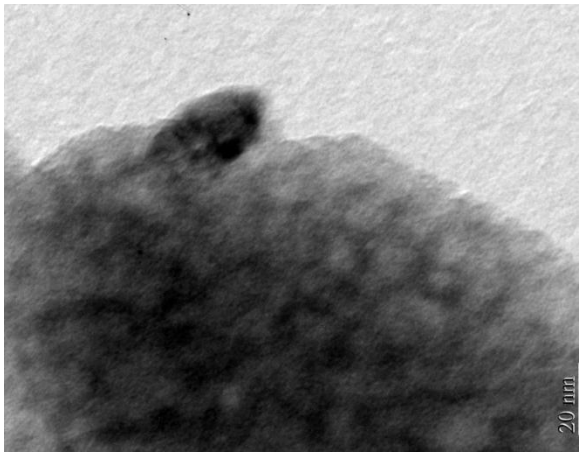

Figure 56: TEM micrograph showing mostly amorphous structure of NAS glass aged for 24 hours at 815°C

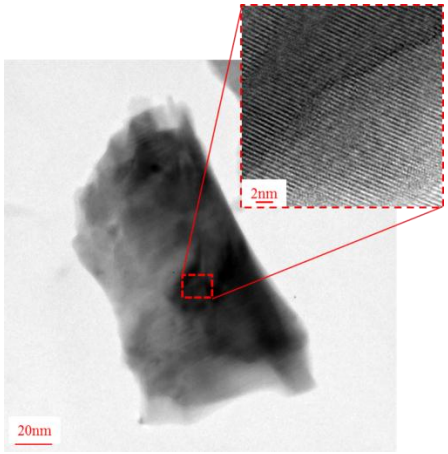

Figure 57: TEM micrograph showing clustered crystallites precipitated in a sample of NAS glass aged for 48 hours at 815°C

The XRD data for powders from the 48 hour aged disk (*Figure 20*) displayed small peaks that seem to correspond to CeO_2, though the peak intensities are too low to be certain. However, CeO_2 actually absorbs photons in the near-UV/blue region, and so luminescence intensity would be expected to drop off drastically as the population of Ce^{4+} centers increased [52]. This may explain the degradation in spectroscopy performance of the disk aged for 48 hours. However, it is unclear why the sample aged for 24 hours would have shown an initially higher light yield in PL/PLE if a CeO_2 phase was being formed.

A previous study by Dantelle [101] showed that the formation of nuclei in PbF_2(Er/Yb)-doped oxyfluoride glass-ceramic depended strongly on the concentration of ErF_3 and YbF_3 in the batch. The rare-earth halides served as seeding agents for the formation of PbF_2 nuclei, with the average crystallite size decreasing from 27nm to 11nm as the total concentration of rare-earth halides was increased from 2-3mol%, as shown in *Figure 58*.

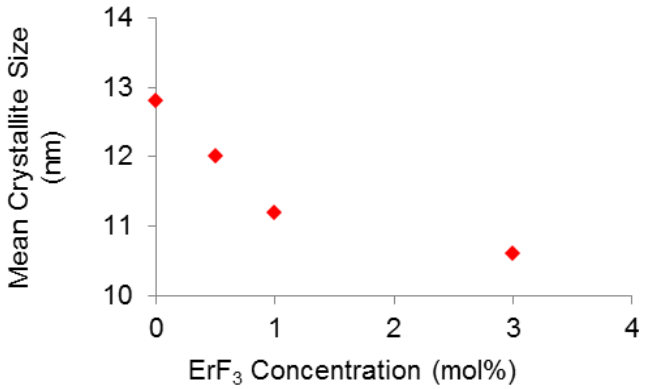

Figure 58: Data plotted from Nikl [101] *showing a decrease in the average crystallite size precipitated as rare-earth halide concentration increased*

Larger concentrations of seed compounds also increased the spatial uniformity of nuclei, though a limit appeared to be reached, beyond which further additions induce

uncontrolled crystallization when the melt as cast and quenched. Increased concentration of nucleating agents also lowered the ceramization temperature [102], as shown by the DTA traces in *Figure 59*. It is crucial for this reaction temperature to be well separated from both the matrix devitrification and glass transition regions to ensure crystallite growth is easily controlled.

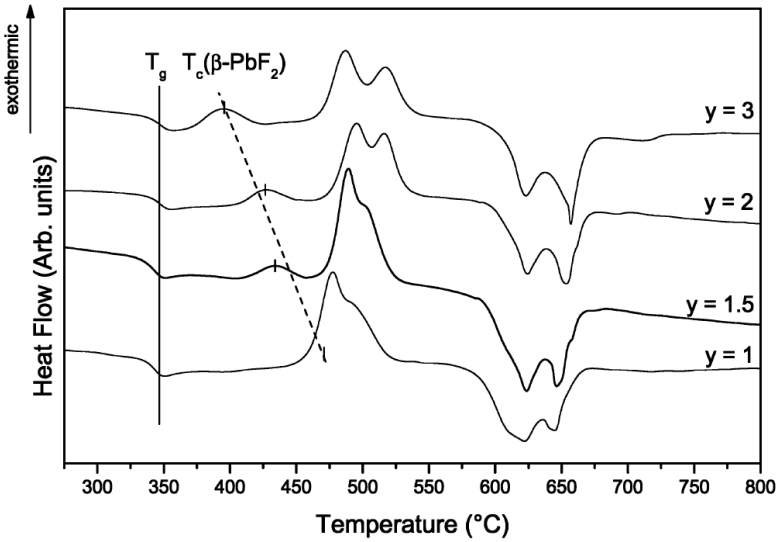

Figure 59: DTA traces from study by Mortier that show how increasing the concentration of nucleating agents reduces the ceramization reaction temperature. The variable 'y' refers to the Yb content [49].

The 20-30mol% loading of rare-earth halides used in this study far exceeded the 1-3mol% used in Nikl's study, and so similar nucleation and growth behavior was expected. However, the characterization methods discussed previously suggest that this was not the case. A study published by Mortier [102] reported that 16-18mol% PbF_2-ErF_3 loading produced nucleation and precipitation of a PbF_2(Er) crystalline phase during ceramization, which indicates that the seeding mechanism still occurs at higher halide concentrations. A major contributor to the discrepancies may be structural non-uniformities in the glass, which can act as preferential sites for heterogeneous nucleation

of scintillating crystals [103]. Randomly distributed defects such as bubbles and regions of higher thermal stress could be sites of higher preference for nuclei formation. When these nuclei grow to crystals, the inhomogeneous distribution of crystals in the glass produces an anisotropic optical response, which may reduce light yield and degrade energy resolution as observed.

Alumino-Borosilicate (ABS) Series

In the ABS glass system, light yield increased with the concentration of scintillating compounds up to the maximum concentration of 30mol%, though the diagram in *Figure 6* predicts that solute concentrations above 31mol% will be rejected and cause formation of a gadolinium silicate phase [70], [72]. However, synthesis of additional batches is required to validate this hypothesis. As $GdBr_3$(Ce) concentration was increased, the excitation peak increased in width and intensity, and the 350nm peak became more prominent than the 320nm peak. The greater peak width was most likely caused by modifications to the glass network caused by rare-earth halide additions to the matrix [104]. Each Ce^{3+} was expected to create two NBO's, which would locally modify the structural environment surrounding the cerium luminescent center [105]. This would introduce greater variance in the crystal field splitting because no two luminescence centers experience the exact same structural surroundings, and thus cause inhomogeneous broadening of the emission peaks. The higher peak intensity resulted from an increased number of luminescent centers with additional $CeBr_3$. The PL intensity for the sample loaded with 20mol% $GdBr_3$-$CeBr_3$ was higher than the 30mol% loading, suggesting that concentration quenching may have begun past 20mol%. However, the light yield was still

much higher than in either of the other systems. Additional studies will be required to determine the $GdBr_3$-$CeBr_3$ loading that marks the onset concentration quenching more precisely. The 350nm excitation/absorption peak may have become more prominent as the population of Ce^{4+} in the network increased. The higher oxidation state of cerium absorbs energy via transfer of charge from neighboring oxygen atoms, with an absorption edge of near 450nm [52]. Because these glasses were prepared in a reducing atmosphere, the Ce^{3+}/Ce^{4+} equilibrium favors the trivalent state, and so the few Ce^{4+} centers present only cause a slight red shift in absorption. The higher Ce^{4+} population was most likely caused solely by the increased $CeBr_3$ concentration.

The refractive index decreased from 1.616 to 1.608 as the $GdBr_3$-$CeBr_3$ concentration was increased from 20mol% to 30mol%, which was unexpected since increases in density and number of NBO's are usually correlated to an increase in refractive index [92]. However, work by Li [88] showed that additions of neodymium to an ABS host glass stabilized AlO_4 tetrahedra, which increased the connectivity of the glass network and lowered the refractive index [106]. Furthermore, rare-earth elements appear to have a greater proclivity for partitioning into a modifier-rich borate phase than a silica-rich phase when incorporated into a borosilicate glass network [107]. Because the electronegativity of boron is higher than that of silicon, the rare-earth electron density is more tightly held and thus less polarizable, resulting in a lower refractive index.

When ABS-20mol% $GdBr_3$(Ce) was aged at 850°C, there was no discernible dependence of the light yield on aging time. Similar behavior was seen for the samples aged at 930°C for varying times (*Figure 34*), though the light yield for that series was consistently

below that recorded for an unaged sample. Much longer XRD scan times were required to bring peaks above the background noise for samples aged at 850°C. The highest intensity peaks were attributed to a $GdBO_3$ phase, with the lower intensity peaks matching $Gd_{0.6}Ce_{0.4}O_{1.70}$. It is possible that, for some reason, a lower fraction of cerium incorporated into the crystalline phase than gadolinium. This would leave the cerium luminescent centers in the high-phonon amorphous phase. Alternatively, it is possible there was significant burn off of cerium during the melting step, and so there is a low concentration in the overall system. Additional study, particularly regarding composition, is required to verify either of these hypotheses. The XRD peaks in the 930°C series closely matched $Gd(BO_3)$ with fewer second phase peaks visible. The refractive index for each of the samples aged at 930°C exceeded the maximum available (1.640) in the set of index matching liquids used, which may have been a product of decreased network connectivity or increased density with a higher volume fraction crystalline phase.

As expected, the energy resolution in the gamma-ray spectrum improved with increasing mole fraction $GdBr_3$(Ce). A 662keV photopeak with 38% resolution was clearly visible in the spectrum generated by a scintillator with 30mol% $GdBr_3$(Ce). The light yield was far lower for the sample with 20mol% loading, though the photopeak resolution was slightly better at 35%. This behavior was reversed in the case of alpha-spectroscopy, where the 20mol% scintillator produced a resolution of 38% at the 5.5 MeV photopeak that was well separated from any background noise, with terrible resolution in the 30mol% sample at 89%. The density of the 30mol% $GdBr_3$(Ce) sample was higher than that of the 20mol% sample, imbuing the 30mol% sample with a higher stopping power.

This caused incident alpha-particles to be absorbed over a shorter interaction distance in the 30mol% sample, resulting in a higher fraction of photons originating from near the glass surface [44]. Photons produced closer to the scintillator surface are more likely to escape before reaching the PMT [16], [19], which causes incomplete light collection and creates a more prominent scattering region in the energy spectrum. Furthermore, photons transitioning from the high refractive index scintillator (1.6) to the lower refractive index PMT (1.5) may experience total internal reflection [35], which reduces the light yield transferred to the PMT within the integration time or increase the fraction of photons that are scattered or absorbed. To mitigate this effect, higher refractive index optical coupling grease may be used or the scintillator surface can be roughened or modified to ensure more intimate contact at the interface.

In the ABS system, increasing scintillator size appeared to improve spectroscopy performance. As seen in *Figure 40*, the 127g scintillator generated a photopeak resolution of 38%, compared to 35% produced by the 68g sample, though the light yield increased by roughly 50% with the increased sample size. The higher light yield was the result of incident gamma-rays depositing a larger fraction of their total energy within the volume of the 127g scintillator compared to the 68g, though the resolution may have been degraded by structural defects and increased scattering within the larger volume scintillator [108]. The opposite behavior was seen in the alpha-spectra in *Figure 41*, where the smallest (54g) scintillator displayed the highest peak intensity and finest energy resolution (45%), despite the lower light yield. The resolution from the 127g sample was 89%, with 53% resolution achieved in the 68g sample, though a portion of

the photopeak was imbedded in the background noise. The discrepancy is, again, most likely caused by increased probability of photons escaping from near the surface of the larger sample, which creates greater statistical fluctuation in photon statistics reaching the PMT, and a larger population of near-surface photons.

The two structural defects that appear to have been most problematic in the larger scintillators were residual thermal stresses and trapped bubbles. Residual thermal stresses, shown in the polariscope images in *Figure 60*, are caused by variations in cooling rate experienced by different regions of the glass, which result in broader distribution of bond angles and distances throughout the network. These structural variations locally alter the refractive index of the glass [83], and scatter incident photons. Photons passing through regions of higher refractive index will be slowed relative to those in a region of lower refractive index, which introduces a delay in the time it takes for the entire photon pulse to reach the scintillator-PMT interface, in addition to the scattering and reflection problems discussed earlier. If the arrival of the slowed photons at the PMT interface is delayed longer than the integration time, these photons are not included in the integrated electrical pulse, which introduces error to the energy spectrum and degrades resolution. However, the severity of the effect of delayed photon integration was most likely negligible since a material with a refractive index of 2.0 would impart a 2ns delay to photons traveling 30cm [35], compared to the ABS system which had a refractive index of 1.608 and only 5cm length.

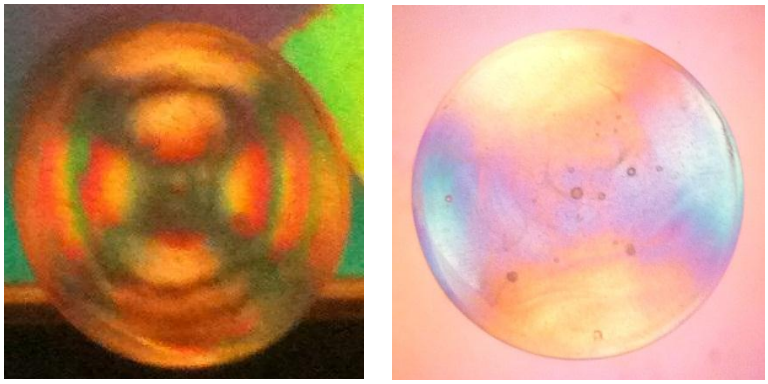

Figure 60: Photographs of 106g NAS sample annealed for 72 hours (left) and 120 hours (right)

In addition to residual thermal stresses, bubbles formed during the melting step and trapped in the final cast part were particularly problematic in the ABS system, with the severity amplified at larger batch sizes. Bubbles were formed when precursor glass powders, such as H_3BO_3 and Na_2CO_3, decomposed and released CO_2 and H_2O during firing [92]. If the melt viscosity was sufficiently high, smaller bubbles became trapped within the resulting cast glass, and caused severe photon scattering at the bubble-glass interfaces. It is thus ideal to eliminate all or as many bubbles from the melt as possible by the addition of fining agents, such as NaF [109]. While NaF additions did not eliminate all bubbles from the ABS melts, the concentration of bubbles through the bulk of the sample was greatly reduced relative to the batches without fining agent. This decreased photon scattering and yielded a drastic improvement in spectroscopy performance between the glass-ceramics with and without the added fining agent (see *Figure 42* and *Figure 43*).

Sodium-Borosilicate (NBS) Series

The primary reason for investigating the NBS glass system was to lower the processing temperatures required. In this sense, the glass system fulfilled its desired purpose. However, the borate-rich system had a significantly lower solubility of scintillating compounds relative to the other glass systems, with a maximum achievable loading of 15mol% $GdBr_3$-$CeBr_3$. Liquid phase separation in the melt and the cast glass also occurred frequently. Additional precursor components, such as BaO and CaO, were incorporated into the glass batch to encourage mixing. This method resulted in somewhat greater melt homogeneity, though when scaling this system to larger batch sizes also proved difficult, continued effort into the development of NBS glasses was not deemed worthwhile. The focus of the overall investigation, therefore, turned solely to the ABS and NAS systems.

Comparison of Radiation Spectroscopy Performance between Glass Systems

The samples from each system that exhibited the highest spectroscopy performance were compared in *Figure 48* and *Figure 49*. The $GdBr_3$(Ce) doping concentrations were 15mol% in the NBS matrix, 19mol% in the NAS matrix, and 30mol% in the ABS matrix. The ABS system produced the highest light yield in both alpha-particle and gamma-ray spectroscopy, though the resolution at the 662keV photopeak was finer in the NAS system (34%) compared to the ABS system (38%). However, there was a narrow separation between the photopeak and the Compton edge in the ABS gamma-ray spectrum, indicating that scattering and incomplete collection of photons were significant [36]. This suggests that if processing techniques are improved to minimize structural

defects in the ABS system, then the superior light yield should produce a finer energy resolution compared to the NAS system due to reduced variance in photon statistics with higher light yields . This theory is supported by a similar trend in the relative light yield and energy resolution seen in the corresponding alpha-spectra. The light yield was again higher in the ABS system, but structural inhomogeneities scattered photons and degraded energy resolution to 89%, compared to the 32% achieved in the NAS system. Photon scattering may have been exacerbated by the higher refractive index of the ABS system (1.616) compared to the NAS (1.580), which increased photon path length through the glass and therefore increased the probability that photons would be scattered by trapped bubbles and other absorption centers. The refractive index of the ABS system may be lowered by increasing the connectivity of the glass network with a higher concentration of refractory compounds, or by substituting the sodium with a less easily polarized alkali cation.

The ABS system also showed superior performance when a similar $GdBr_3$(Ce) loading is incorporated into all three glass systems, as shown by the relative luminescence light yields in *Figure 47*. While the NBS system contained only 15mol% $GdBr_3$(Ce), both the NAS and ABS systems contained approximately equivalent (20 ± 1mol%) $GdBr_3$(Ce) in the precursor batch, but showed very notably different luminescence and spectroscopy behavior. The discrepancies in light yield between the two systems were attributed to differences in the structure of the glass network, which can affect the radiative behavior of rare-earth dopants [96] and the transmittance of emitted photons. For example, the ABS system contained higher boron concentrations relative to the NAS glass, which

probably allowed thermal stresses to be more easily relaxed during annealing of the larger scale batches. The importance of removing thermal stresses was already illustrated in *Figure 24*, which illustrates how longer annealing time improved alpha-spectroscopy performance. Polariscope photographs of the NAS sample shown in *Figure 60* further illustrate the extent to which residual thermal stresses refract light within the larger samples.

While the higher boron content may have improved the performance of the ABS system relative to NAS, the NBS system, which contained the highest boron loading, showed very poor spectroscopy performance. This suggests that the more refractory compounds (Al_2O_3 and SiO_2) play a very important role in ensuring that photons travel through the glass network unimpeded. As discussed previously, Al_2O_3 additions strengthen the connectivity of the SiO_2 glass network by forming AlO_4 groups, which create Al-O-Si bridges that decrease the refractive index [106], and also lower the phonon relaxation tendency of rare-earth ions in the glass [110]. Some rare-earth dopant ions, such as Yb^{3+}, also tend to cluster and form localized regions of high dopant concentration in silica glasses [111] (as shown in *Figure 61*), and such clustering can prematurely induce concentration quenching effects [112]. A study by Arai [113] showed that the addition of aluminum cations will break up these rare-earth cation clusters and thereby improve luminescence efficiency. It is possible that the Ce^{3+} activator used in this study caused clustered crystallites to form, though additional TEM studies are required to be certain. Studies by Vedda et. al. [114] showed that high-cerium concentrations doped into sol-gel silica glasses tend to form CeO_2 aggregates, which severely quench luminescence.

Additional work is required to determine if the reducing atmospheres used in this study were sufficient to inhibit the formation of Ce^{4+} and its corresponding aggregated crystallites.

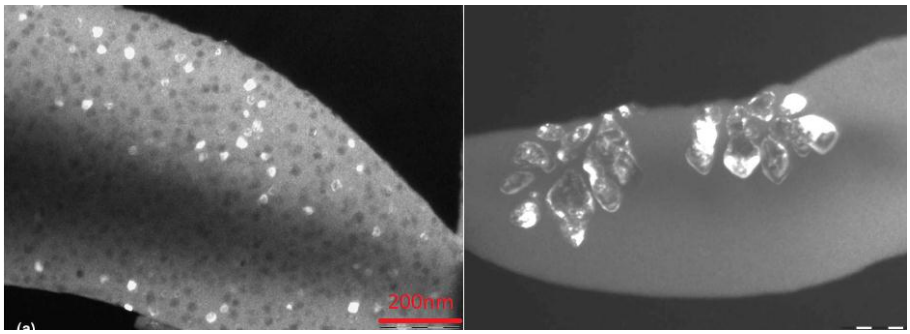

Figure 61: TEM micrographs showing how some rare-earth dopants, such as Er^{3+}, can encourage uniform spatial distribution of crystallites (left), while others, such as Yb^{3+}, cause crystallites to cluster and prematurely induce concentration quenching [101].

The scintillators compared in the gamma-ray and alpha-particle spectra shown in *Figure 48* and *Figure 49* were cylinders of as-cast glass. Changes in luminescent and spectroscopy behavior upon aging the NAS and ABS glass systems suggest that the crystalline phase precipitated from the ABS system degraded scintillation efficiency, while that precipitated from the NAS system initially increased efficiency. From XRD data of the ABS system (*Figure 36*), the gadolinium appeared to segregate into a borate-rich phase during the ceramization step, with no detectable traces of cerium, which resulted in considerable reduction of luminescence intensity (*Figure 34*). In contrast, a $Ce_{0.7}Gd_{0.3}O_{1.85}$ phase was identified in XRD analysis of aged NAS samples, and the degradation of luminescence intensity was less pronounced. While rare-earth metaborates are capable of exhibiting luminescence [115], it appears that segregation of the cerium activator ions into the borate-rich phase is energetically unfavorable in the ABS system studied. In addition, the B-O bond is more covalent in nature than the Si-O bond, which

reduces the degree of expansion experienced by a neighboring Ce^{3+} electron cloud [116]. A more expanded electron cloud decreases the binding energy of the outermost electrons via the Nephelauxetic effect, which allows them to be more easily promoted to the *5d* energy levels [107], [116], [117]. This creates a larger Stokes shift and reduces the self-absorption tendency of the Ce^{3+} luminescence center, thereby increasing luminescence efficiency in the silica-rich system. Future work should, therefore, involve determining glass chemistry or processing techniques that will suppress segregation of rare-earth compounds into the borate-rich phase and promote incorporation into the silica-rich phase in order to maximize luminescent efficiency.

Li suggested [87] that the formation of the $Gd(BO_3)$ phase in an ABS system may be inhibited by modifying the glass chemistry to saturate the borate-rich phase with gadolinium, which would make incorporation of gadolinium into the silicate phase more favorable. Work by Qian et. al. [71] also showed that gadolinium will preferentially segregate into a silica-rich rather than borate-rich phase if the concentration of gadolinium in the glass exceeds a critical threshold. However, in both cases, the solubility limit of rare-earths in the borate phase must be exceeded before solute will begin to segregate into the silicate phase. The drawback is that the rare-earth silicate crystallization reaction tends to occur during melt quenching and so precipitate size is not controllable [72], making this method undesirable. Alternative modifications of glass composition will need to be explored to precipitate the desired phase in a controlled manner.

Conclusions & Future work

While the glass-ceramics synthesized over the course of this investigation did not produce photopeaks with energy resolution as fine as NaI(Tl), producing any discernible photopeaks with a material other than a single crystal is a significant achievement. These initial successes suggest that, with additional development and study, glass-ceramics may prove to be a viable alternative to single crystal scintillators. Potential problems that may have degraded the performance of the glass-ceramics include a lower concentration of scintillating compounds relative to single crystals, scattering of emitted photons caused by residual thermal stresses in the glass, and scintillator volumes slightly smaller than typical NaI(Tl) single crystals. Future studies will work to improve glass processing to reduce the concentration of bubbles trapped in the glass matrix and provide greater understanding of and control over the ceramization reaction.

APPENDIX

Presentations & Publications

Poster Presentation, The 4th International Congress on Ceramics; Chicago, Il; July 2012

Poster Presentation, 5th Annual Meeting of Awardees of the Academic Research Initiative; Lansdowne, VA; July 2012

Gamma Ray Scintillators via BaF_2:Ce Nanopowders

M. Brooke Barta
Georgia Tech Research Institute
925 Dalney St, Atlanta, GA 30332

Introduction

Motivation for Development

According to the Security and Accountability for Every Port Act (SAFE Port Act, H.R. 4954), all cargo entering the country must be scanned for threatening radioactive material.[1] Current scintillator detectors are fragile, hygroscopic, and unable to classify the specific isotope emitting radiation. This research focuses on improving two main scintillator properties: photon yield and bulk density.[2] Photon yield/production refers to the number of photons produced per MeV of gamma ray energy absorbed,[3] while bulk density correlates to the atomic weight of the host/dopant material. Ideal scintillators will have a light yield of more than 5×10^4 photons/MeV, and high bulk density (alkaline/actinide elements) for increased photon interaction.[3]

The best scintillators currently in use are single crystals of NaI, doped with less than 1mol% Tl. These scintillators have a photon yield of 4.1×10^4 photons/MeV and a density of 3.67 g/cm^3.[2] NaI(Tl) single crystals can be grown easily and economically, but are extremely fragile and hygroscopic, and so must be encased in a protective shell.[3] Large single crystals of BaF_2 have lower photon yields than NaI(Tl) crystals due to a higher concentration of defects arising from more sensitive crystal growth.[3] Difficulty arises from the need to grow large single crystals of BaF_2, but if crystal size could be decreased, photon yield and energy resolution could increase.

Inorganic Phosphor Nanopowders

Nano-scale phosphor powders (nanophosphors) offer improved photon yields compared to single crystals by minimizing absorption and scattering due to impurities, which are a problem in large crystal growth.[4-5] BaF_2:Ce nanophosphors in particular exhibit properties that suggest superior performance in scintillator technology. Energy deposited into the powder by lower energy radiation will not excite electrons in BaF_2, and thus the powder will only generate scintillation photons in the presence of high energy gamma-rays, thereby eliminating much noise from the energy spectrum.[6]

Direction of Work

This investigation seeks to improve scintillators by increasing scintillation material density, and increasing photon yield by decreasing defect concentration. Past studies have indicated that scintillator efficiency can be improved by doping a host crystal with rare earth elements.[3] Maintaining this assumption, BaF_2:Ce nanopowders will be

synthesized using a method similar to the chemical precipitation synthesis of LaF_3:Ce.[7] Goals include the creation of a nanophosphor with a high bulk density and increased photon production. Photoluminescence excitation (PLE) and emission (PL), and X-ray diffraction (XRD) measurements will be used to characterize all powders synthesized. Powders with high efficiency indicated by PL measurements will be encapsulated in a UV curable polymer, and gamma ray measurements conducted to measure efficiency upon excitation by a radionuclide source. The results will be compared to single crystal NaI(Tl) scintillators, which are currently the most efficient.

Procedure

BaF_2:Ce Nanophosphor Synthesis

BaF_2:Ce with doping levels from 1-30mol% were synthesized. The molar amount of $Ba(NO_3)_2$ powder was held at a constant 18.89mmol while the amount of $Ce(NO_3)_3$ powder was varied from 0.2-8.09mmol to achieve the desired doping level. These powders were mixed in 80mL of deionized (DI) water in a round bottomed flask, and the mixture stirred mechanically. In a separate flask, 1.6g NaF was mixed into 100mL of DI water with a solution of 3.6g of oleic acid in 100mL of ethanol. This solution was heated to 78°C using a heating mantle. The $Ba(NO_3)_2$ solution was then added drop-wise under a nitrogen gas purge to the NaF solution, and the final mixture held and stirred at 78°C for one hour. The solution was then centrifuged at 3000rpm for 15 minutes, then the liquid decanted and 200mL of ethanol added to each flask. The BaF_2:Ce powders were mechanically agitated and a sample of the suspension was taken and placed into a

scintillation vial for photoluminescence tests. The powder was then dried in air overnight.

BaF_2:Ce Nanophosphor Characterization

Photoluminescence excitation (PLE) measurements were conducted using a Cary Eclipse Fluorescence Spectrometer with a monitor wavelength of 353nm to find the optimal excitation wavelength for the BaF_2:Ce powders. The sample was excited with wavelengths ranging from 200nm to 340nm. Photoluminescence emission (PL) measurements were conducted using a 288nm excitation beam (determined from the PLE measurements) scanning a wavelength range from 300nm to 480nm.

Transmission electron microscopy (TEM) was used to confirm that the nanophosphors were composed of individual particles, while X-ray diffraction (XRD) was used to determine BaF_2:Ce crystallite size. TEM analysis was conducted using a JEOL 100CX TEM operating at 100kV. Particle size analysis was conducted with an X'Pert Pro α-1 diffractometer equipped with a Cu Kα X-ray tube emitting at 1.54Å scanning a 2θ range from 20-70°.

Scintillator Fabrication

To match the refractive indices (RI) of the powder and polymer matrix, commercially available liquids with known RI at 589nm from Cargille Labs Inc. (Cedar Grove, NJ) were used in conjunction with a Leica M165C optical microscope and a 400nm LED. Two drops of RI matching liquid were added to 10mg of BaF_2:Ce powder on a glass slide. An optical microscope was used to determine the visibility of the powder

agglomerates under each RI liquid, which was the criterion for determining the RI of the powder. After a matching liquid was found, a dispersion curve for the specific liquid was acquired from the manufacturer, and the RI of the powder estimated via a polynomial fit to the data.

A UV curable (OptiClad) polymer with a RI of 1.485 at 389nm was acquired from Ovation Polymers (Medina, OH) and used to encapsulate the BaF_2:Ce nanophosphors. The custom made polymer was a mixture of several different monomers that imparted the specific physical and optical properties needed for this investigation. BaF_2:Ce was placed into 10mL of the OptiClad polymer in a standard 40mm diameter by 30mm deep mold. The suspension was homogenized using a Fisher Scientific 550 sonic dismembrator probe to disperse the powder uniformly in the polymer, and then cured using a Lesco Rocket Cure SuperSpot Mk II UV lamp operating with a 100W DC mercury vapor short-arc.

Gamma Ray Measurements

Gamma ray measurements were conducted using a radionuclide source placed on top of the cylindrical scintillator sample. The sample and source were placed on a photomultiplier tube (PMT) and the entire apparatus encased in a shield to block excess light. Photons generated by the scintillator-gamma-ray interactions were recorded by the PMT, and assigned a "channel number" ranging from 1-12keV depending on the energy of the photon emitted. In this test, 1,040 channels between 1keV and 12keV were used, with a total counting time of 6×10^4s.

Results & Discussion

BaF_2:Ce Synthesis

The total mass of the finished BaF_2:Ce powder was kept below 5g because it was found that extensive agglomeration would occur when the batch size exceeded 8g. Drying the finished powder in air also introduced error because BaF_2 is hygroscopic, causing the powder to absorb moisture during the drying process. This was problematic during encapsulation, when excess moisture had an adverse effect on the polymer curing process and, therefore, data collected.

PL and PLE Trends

PLE data monitored at 353nm, yielded a peak at 288nm, indicating that this wavelength would most efficiently excite the BaF_2:Ce powders. A wavelength of 353nm was chosen for PLE measurements from peak locations in a PL spectra.

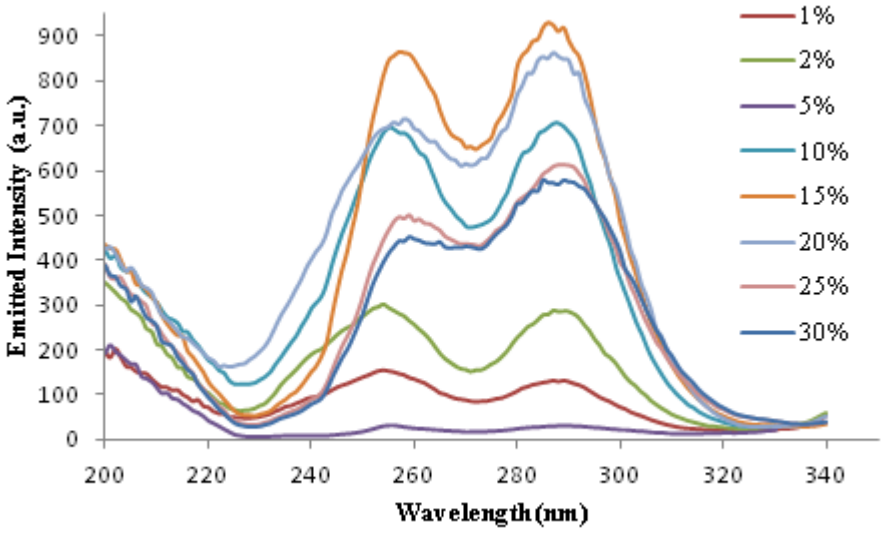

Figure 1: PLE data for BaF_2:Ce powders with dopant levels 1-30mol% (see legend)

After the optimal 288nm excitation wavelength was determined, PL scans were conducted on samples of each doping concentration. It was found that the BaF_2:15%Ce powder sample showed the greatest light intensity between 300-480nm. Reduced photon production (concentration quenching) occurred at 15mol% Ce doping, a much higher level than in large crystals (usually less than 1mol%). One possible explanation for this discrepancy is that energy transfer may be regulated to the nanometer region, thus the energy loss due to dopant-dopant transitions is less widespread and therefore less serious of a problem.[8]

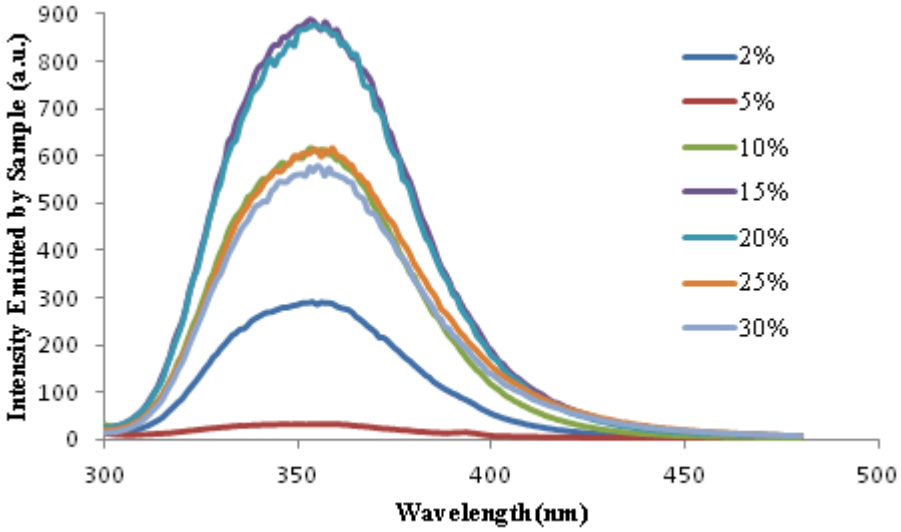

Figure 2: PL data (λ=288nm) for BaF_2:Ce powders with dopant levels 1-30mol% (see legend)

Via TEM observation (see Figure 3), it was concluded that the powder synthesized was composed of individual particles. Results from the XRD analysis are shown in Figure 4, and particle size was estimated to be between 40nm and 50nm using Debeye-Scherrer analysis.

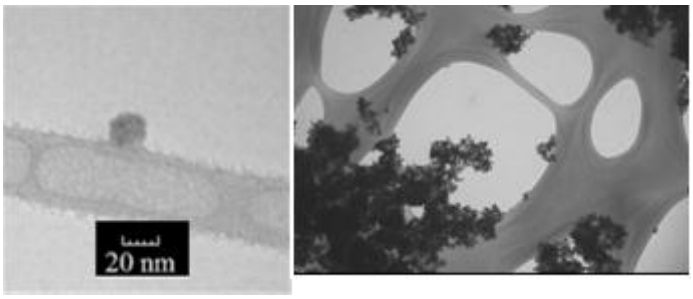

Figure 3: TEM images of BaF_2:15%Ce particle

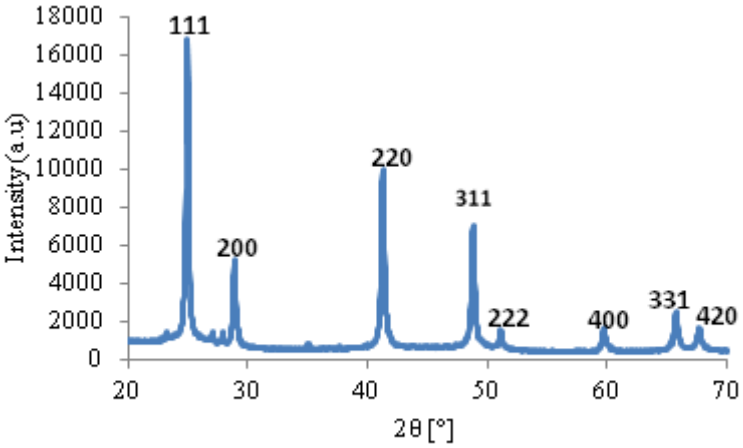

Figure 4: XRD pattern of BaF_2: 1%Ce nanophosphor powder

Nanopowder/polymer Composite

Using RI matching liquids, it was found that the BaF_2:Ce powder should have a RI of 1.485 at 389nm. The puck of BaF_2:Ce encapsulated in the OptiClad polymer was exposed to an Am-241 radionuclide source. The counts for each channel number were summed and normalized to counting time to generate an energy spectrum (Figure 5Figure) from photons generated by gamma-ray excitation of the phosphors. These values would ideally generate energy peaks characteristic of Am-241, which is more accurately shown in the energy spectrum produced by a NaI(Tl) single crystal scintillator (Figure 6). It is theorized that the low photon production and poor energy resolution were caused by

adverse polymer-phosphor chemical interactions, which induced photon scattering rather than transmission, causing the puck to appear a cloudy shade of yellow instead of the desired clear.[9] The opacity may also have been caused by overheating during the polymerization process, which is exothermic, thus creating difficulty in stabilizing the sample temperature as polymer thickness increased. The high and unstable temperatures may have caused monomer burn off, thus altering the optical properties of the cured polymer. The overheating problem could be solved by placing the mold in an ice bath during curing, or chilling the sample in a refrigerator or freezer prior to curing.

Low resolution in the energy spectrum may also be due to a lower density of scintillating material in the composite scintillator compared to a single crystal, thus resulting in a lower light yield. The NaI(Tl) single crystal is composed entirely of scintillating material, whereas the composite scintillator was only loaded with 50vol% scintillating particles, reducing the probability of incident gamma-rays striking and interacting with scintillating material. This problem could be mitigated by encapsulating a higher concentration of particles, or pressing a pellet of BaF_2:Ce particles and using the polymer as a binder. Although 1024 channels were available during the scans, no relevant peaks were generated above channel #61, and so channels above this value are are omitted from the spectra. Removing the superfluous channels simplified analysis of the peaks that were generated by the scintillators under Am-241 excitation.

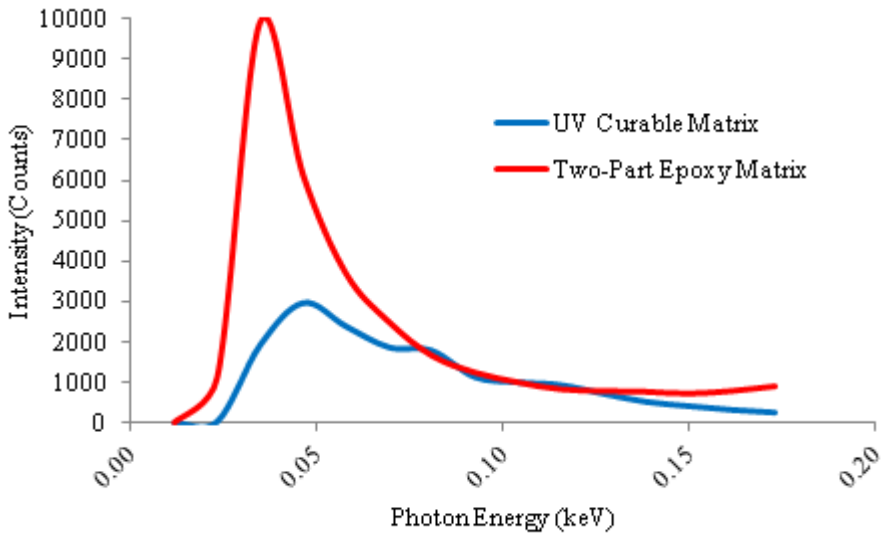

Figure 5: Gamma ray data (energy spectrum) generated by BaF_2:Ce encapsulated in UV curable matrix (50vol% solids loading), measured over 6×10^4s under an Am-241 radionuclide source

Conclusion

While BaF_2:15mol%Ce showed the greatest efficiency of the powders synthesized, if polymer encapsulation remains the preferred method of fabricating the nanophosphor scintillators, a polymer with a more controllable polymerization process will need to be procured. Alternatively, particles may be pressed into a pellet and the polymer used as a protective binder rather than an encapsulant in order to maximize density of scintillating material.

Future Work

Future work in nanophosphor synthesis will include doping BaF_2 with other lanthanide series ions such as Eu^{2+} that have the potential to further increase photon production. Doping with this ion is desirable because it exhibits greater fluorescence on the blue side

of the light spectrum, allowing the light to pass through the polymer matrix (which absorbs light close to UV energy).

Acknowledgements

The author gratefully acknowledges Dr. Jason H. Nadler and Dr. Zhitao Kang of the Georgia Tech Research Institute at the Georgia Institute of Technology for their supervision and guidance. Research was conducted as part of an initiative by the Domestic Nuclear Detection Office (DNDO) in response to the SAFE Port Act.

References

1. U.S. Congress. (2006). Security and accountability for every port act Washington, D.C.

2. C.W.E. van Eijk. "Inorganic-scintillator Development," *Nucl. Instrum. Methods Phys Res, Sect A*, A **2001**, 460, 1-14

3. K.W. Kramer. "Development and characterization of highly efficient new cerium doped rare earth halide scintillator materials," *J Mater Chem*, **2006,** vol. 16, 2773

4. W.H. Tait. Radiation Detection; Butterworth: Boston, 1980

5. D.W. Cook. "Luminescent properties and reduced dimensional behavior of hydrothermally prepared Y_2SiO_5:Ce nanophosphors," *Appl Phys Lett*, **2006,** vol. 88, 103

6. A.V. Golovin. "Mechanism of short-wavelength luminescence of barium fluoride," *Opt Spectrosc*, **1988**, vol. 65, 102

7. J. del-Castillo. “Wide colour gamut generated in triply lanthanide doped sol-gel nano-glass-ceramics,” *J. Nanopart*. Res, **2009**, 789-884

8. T.C. Madden. “The use of Semiconductors Doped with Isoelectronic Traps in Scintillation Counting,” *IEEE Trans Nucl Sci*, June 1968, vol. 15, no. 3, 47-57

9. R. Rosson, Georgia Tech Research Institute, Atlanta, GA, personal communication, 2009.

BIBLIOGRAPHY

[1] D. Lungren, *SAFE Port Act*. Washington, D. C.: United States Congress, 2006, pp. 1–79.

[2] B. D. Milbrath, A. J. Peurrung, M. Bliss, and W. J. Weber, "Radiation Detector Materials: An Overview," *Journal of Materials Research*, vol. 23, no. 20, pp. 2561–2581, 2008.

[3] J. H. Ely, E. R. Siciliano, and R. T. Kouzes, "Comparison of NaI(Tl) scintillators and high purity germanium for vehicle portal monitor applications," *IEEE Symposium Conference Record Nuclear Science 2004.*, vol. 00, no. C, pp. 1584–1587, 2004.

[4] R. T. Klann, J. Shergur, and G. Mattesich, "Current State of Commercial Radiation Detection Equipment for Homeland Security Applications," *Radiation Protectin and Shielding Division*, pp. 555–563, 2008.

[5] N. J. Cherepy, J. D. Kuntz, Z. Seely, S. Fisher, O. B. Drury, and B. Sturm, "Transparent ceramic scintillators for gamma-ray spectroscopy and radiography," *SPIE*, 2010.

[6] I. H. Campbell and B. K. Crone, "Quantum-Dot/Organic Semiconductor Composites for Radiation Detection," *Advanced Materials*, vol. 18, no. 1, pp. 77–79, Jan. 2006.

[7] B. M. Tissue, "Synthesis and Luminescence of Lanthanide Ions in Nanoscale Insulating Hosts," *Chemistry of Materials*, vol. 10, no. 10, pp. 2837–2845, Oct. 1998.

[8] N. J. Cherepy, B. W. Sturm, O. B. Drury, T. a. Hurst, S. a. Sheets, L. E. Ahle, C. K. Saw, M. a. Pearson, S. a. Payne, A. Burger, L. a. Boatner, J. O. Ramey, E. V. van Loef, J. Glodo, R. Hawrami, W. M. Higgins, K. S. Shah, and W. W. Moses, "SrI2 Scintillator for Gamma Ray Spectroscopy," *Proceedings of SPIE*, vol. 7449, p. 74490F–74490F–6, 2009.

[9] J. Chongyi, W. Xingui, G. Du, Z. Zhipeng, and Z. Yucan, "Growth and Properties of Scintillating Crystal BaF2," *Journal of Crystal Growth*, vol. 79, pp. 720–722, 1986.

[10] B. D. Milbrath, B. J. Choate, J. E. Fast, W. K. Hensley, R. T. Kouzes, and J. E. Schweppe, "Comparison of LaBr3:Ce and NaI(Tl) Scintillators for Radio-Isotope Identification Devices," *Nuclear Instruments and Methods in Physics Research*

Section A: Accelerators, Spectrometers, Detectors and Associated Equipment, vol. 572, no. 2, pp. 774–784, 2007.

[11] K. O. Findley, J. Johnson, D. F. Bahr, F. P. Doty, and J. Frey, "Fracture and deformation behavior of common and novel scintillating single crystals," *Proceedings of SPIE*, pp. 670706–670706–12, 2007.

[12] R. Visser, P. Dorenbos, C. W. E. Van Eijk, and R. W. Hollander, "Scintillation properties of Ce3 + doped BaF2 crystals," *IEEE Transactions on Nuclear Science*, vol. 38, no. 2, pp. 178–183, 1991.

[13] E. V. van Loef, C. M. Wilson, N. J. Cherepy, G. Hull, S. a. Payne, W.-S. Choong, W. W. Moses, and K. S. Shah, "Crystal Growth and Scintillation Properties of Strontium Iodide Scintillators," *IEEE Transactions on Nuclear Science*, vol. 56, no. 3, pp. 869–872, Jun. 2009.

[14] J. Selling, M. D. Birowosuto, P. Dorenbos, and S. Schweizer, "Europium-doped barium halide scintillators for x-ray and γ-ray detections," *Journal of Applied Physics*, vol. 101, no. 3, p. 034901, 2007.

[15] M. Tanaka, K. Hara, S. Kim, K. Kondo, H. Takano, M. Kobayashi, H. Ishibashi, K. Susa, and M. Ishii, "Applications of Cerium-Doped Gadolinium Silicate Gd2SiO5:Ce Scintillator to Calorimeters in High Radiation Environment," *Nuclear Instruments and Methods in Physics Research Section A: Accelerators, Spectrometers, Detectors and Associated Equipment*, 1997.

[16] M. Moszynski, "Energy resolution of scintillation detectors," *Proceedings of SPIE*, vol. 5922, pp. 592205–592205–14, 2005.

[17] G. Chen, J. Johnson, R. Weber, R. Nishikawa, S. Schweizer, P. Newman, and D. Macfarlane, "Fluorozirconate-based nanophase glass ceramics for high-resolution medical X-ray imaging," *Journal of Non-Crystalline Solids*, vol. 352, no. 6–7, pp. 610–614, May 2006.

[18] K. W. Kramer, P. Dorenbos, H. U. Gudel, and C. W. E. van Eijk, "Development and characterization of highly efficient new cerium doped rare earth halide scintillator materials," *Journal of Materials Chemistry*, vol. 16, no. 27, p. 2773, 2006.

[19] E. V. van Loef, P. Dorenbos, C. W. E. Van Eijk, K. W. Kramer, and H. U. Gudel, "Scintillation properties of LaBr3:Ce+ crystals: fast, efficient and high-energy-resolution scintillators," *Nuclear Instruments and Methods in Physics Research Section A: Accelerators, Spectrometers, Detectors and Associated Equipment*, vol. 486, pp. 254–258, 2002.

[20] C. M. Wilson, E. V. van Loef, J. Glodo, N. J. Cherepy, G. Hull, S. Payne, W.-S. Choong, W. W. Moses, and K. S. Shah, "Strontium iodide scintillators for high energy resolution gamma ray spectroscopy," *Proceedings of SPIE*, vol. 7079, pp. 707917–707917–7, 2008.

[21] C. W. E. Van Eijk, "New inorganic scintillators: aspects of energy resolution," *Nuclear Instruments and Methods in Physics Research Section A: Accelerators, Spectrometers, Detectors and Associated Equipment*, vol. 471, no. 1–2, pp. 244–248, Sep. 2001.

[22] K. Yang, S. M. Ieee, M. Zhuravleva, M. Ieee, H. Rothfuss, C. L. Melcher, S. M. Ieee, and A. Crystal, "Optical and Scintillation Properties of Single Crystal CsSr1-xEuxI3," in *Nuclear Science Symposium Conference Record*, 2010, pp. 1603–1606.

[23] Y. Yu, D. Chen, Y. Wang, F. Liu, and E. Ma, "A new transparent oxyfluoride glass ceramic with improved luminescence," *Journal of Non-Crystalline Solids*, vol. 353, no. 4, pp. 405–409, Mar. 2007.

[24] Z. Shan, D. Chen, Y. Yu, P. Huang, H. Lin, and Y. Wang, "Luminescence in rare earth-doped transparent glass ceramics containing GdF3 nanocrystals for lighting applications," *Journal of Materials Science*, vol. 45, no. 10, pp. 2775–2779, Feb. 2010.

[25] J. Fu, M. Kobayashi, S. Sugimoto, and J. M. Parker, "Scintillation from Eu 2+ in Nanocrystallized Glass," *Journal of the American Ceramic Society*, vol. 92, no. 9, pp. 2119–2121, Sep. 2009.

[26] Z. Strnad, *Glass-Ceramic Materials*, 1st ed. New York: Elsevier, 1986.

[27] M. Mattarelli, M. Montagna, F. Rossi, M. Ferrari, V. K. Tikhomirov, and A. B. Seddon, "PROCEEDINGS OF THE TOPICAL MEETING OF THE EUROPEAN CERAMIC SOCIETY " NANOPARTICLES , Tm 3 + -Activated Transparent Oxyfluoride Glass Ceramics : A Study by Raman Scattering of the Nanocrystal Size Distribution 1," in *Topical Meeting of the European Ceramics Society*, 2005, vol. 31, no. 4, pp. 519–524.

[28] X. Wang, J. Chen, J. Li, and H. Guo, "Preparation and luminescent properties of Eu-doped transparent glass-ceramics containing SrF2 nanocrystals," *Journal of Non-Crystalline Solids*, vol. 357, no. 11–13, pp. 2290–2293, Jun. 2011.

[29] V. K. Tikhomirov, D. Furniss, A. B. Seddon, M. Ferrari, and R. Rolli, "Er3+ doped ultratransparent oxy-fluoride glass-ceramics for application in the 1 . 54 μm telecommunication window," *Journal of Materials Science Letters*, vol. 21, pp. 293 – 295, 2002.

[30] G. Chen, J. Johnson, S. Schweizer, J. Woodford, P. J. Newman, and D. R. MacFarlane, "Transparent BaCl:Eu2+ Glass-Ceramic Scintillator," *Proceedings of SPIE*, vol. 6142, p. 61422X–61422X–8, 2006.

[31] W. Drozdowski, P. Dorenbos, a. J. J. Bos, J. T. M. de Haas, S. Kraft, E. Maddox, A. Owens, F. G. a. Quarati, C. Dathy, and V. Ouspenski, "Effect of Proton Dose, Crystal Size, and Cerium Concentration on Scintillation Yield and Energy Resolution of LaBr3 :Ce," *IEEE Transactions on Nuclear Science*, vol. 54, no. 3, pp. 736–740, Jun. 2007.

[32] A. Nassalski, M. Kapusta, T. Batsch, D. Wolski, D. Möckel, W. Enghardt, and M. Moszyn, "Comparative Study of Scintillators for PET/CT Detectors," *IEEE Transactions on Nuclear Science*, vol. 54, no. 1, pp. 3–10, 2007.

[33] M. Balcerzyk, M. Kapusta, A. Syntfeld, D. Wolski, G. Pausch, J. Stein, and P. Schotanus, "CdWO4 Crystal in Gamma-Ray Spectrometry," *IEEE Transactions on Nuclear Science*, vol. 52, no. 6, pp. 3124–3128, 2005.

[34] D. Darambara, "State-of-the-art radiation detectors for medical imaging: Demands and trends," *Nuclear Instruments and Methods in Physics Research Section A: Accelerators, Spectrometers, Detectors and Associated Equipment*, vol. 569, no. 2, pp. 153–158, Dec. 2006.

[35] P. Rodnyi, *Physical Processes in Inorganic Scintillators*. Boca Raton, Fl: CRC Press, 1997.

[36] W. J. Price, *Nuclear Radiation Detection*, 1st ed. New York: McGraw-Hill Book Company, Inc., 1958.

[37] M. Moszynski, J. Zalipska, M. Balcerzyk, M. Kapusta, W. Mengesha, and J. Valentine, "Intrinsic energy resolution of NaI(Tl)," *Nuclear Instruments and Methods in Physics Research Section A: Accelerators, Spectrometers, Detectors and Associated Equipment*, vol. 484, no. 1–3, pp. 259–269, May 2002.

[38] S. O. Kasap, *Principles of Electronic Materials and Devices*, 3rd ed. New York: McGraw-Hill Book Company, Inc., 2006.

[39] A. Meijerink, W. J. Schipper, and G. Blasse, "Photostimulated luminescence and thermally stimulated luminescence of Y2SiO5-Ce, Sm," *Journal of Physics D, Applied Physics*, vol. 24, pp. 997–1002, 1991.

[40] T. Yoshioka and M. Ogawa, "Chapter 14: Measurements of phosphor properties," in *Phosphor Handbook*, 2nd ed., Taylor & Francis Group, LLC, 2006.

[41] S. Tanimizu, “Chapter 3: Principal phosphor materials and their optical properties,” in *Phosphor Handbook*, 2nd ed., vol. 1, Taylor & Francis Group, LLC, 2006.

[42] E. Nakazawa, “Chapter 2: Fundamentals of Phosphors,” in *Phosphor Handbook*, 2nd ed., Taylor & Francis Group, LLC, 2006.

[43] N. Miura, “Chapter 7: Phosphors for X-ray and Ionizing radiation,” in *Phosphor Handbook*, 2nd ed., vol. 54, no. 5, Taylor & Francis Group, LLC, 2006.

[44] G. F. Knoll, *Radiation Detection and Measurement*, 4th ed. Hoboken, NJ: John Wiley & Sons, Inc., 2010.

[45] W. M. Higgins, A. Churilov, E. V. van Loef, J. Glodo, M. Squillante, and K. Shah, “Crystal growth of large diameter LaBr3:Ce and CeBr3,” *Journal of Crystal Growth*, vol. 310, no. 7–9, pp. 2085–2089, Apr. 2008.

[46] N. J. Cherepy, G. Hull, A. D. Drobshoff, S. a. Payne, E. V. van Loef, C. M. Wilson, K. S. Shah, U. N. Roy, A. Burger, L. a. Boatner, W.-S. Choong, and W. W. Moses, “Strontium and barium iodide high light yield scintillators,” *Applied Physics Letters*, vol. 92, no. 8, p. 083508, 2008.

[47] X. Qiao, X. Fan, M. Wang, and X. Zhang, “Spectroscopic properties of Er3+–Yb3+ co-doped glass ceramics containing BaF2 nanocrystals,” *Journal of Non-Crystalline Solids*, vol. 354, no. 28, pp. 3273–3277, Jun. 2008.

[48] J. Petzoldt and W. Pannhorst, “Chemistry and structure of glass-ceramic materials for high precision optical applications,” *Journal of Non-Crystalline Solids*, vol. 129, no. 1–3, pp. 191–198, Mar. 1991.

[49] M. Mortier, A. Bensalah, G. Dantelle, G. Patriarche, and D. Vivien, “Rare-earth doped oxyfluoride glass-ceramics and fluoride ceramics: Synthesis and optical properties,” *Optical Materials*, vol. 29, no. 10, pp. 1263–1270, Jun. 2007.

[50] J. Johnson, S. Schweizer, B. Henke, G. Chen, J. Woodford, P. J. Newman, and D. R. MacFarlane, “Eu-activated fluorochlorozirconate glass-ceramic scintillators,” *Journal of Applied Physics*, vol. 100, no. 3, pp. 034701–034705, 2006.

[51] N. J. Cherepy, S. a. Payne, S. J. Asztalos, G. Hull, J. D. Kuntz, T. Niedermayr, S. Pimputkar, J. J. Roberts, R. D. Sanner, T. M. Tillotson, E. V. van Loef, C. M. Wilson, K. S. Shah, U. N. Roy, R. Hawrami, A. Burger, L. a. Boatner, W.-S. Choong, and W. W. Moses, “Scintillators With Potential to Supersede Lanthanum Bromide,” *IEEE Transactions on Nuclear Science*, vol. 56, no. 3, pp. 873–880, Jun. 2009.

[52] J. Fu, J. M. Parker, R. M. Brown, and P. S. Flower, “Compositional dependence of scintillation yield of glasses with high Gd2O3 concentrations,” *Journal of Non-Crystalline Solids*, vol. 326–327, pp. 335–338, Oct. 2003.

[53] W. Chewpraditkul, D. Chen, B. Yu, Q. Zhang, Y. Shen, M. Nikl, R. Kucerkova, A. Beitlerova, C. Wanarak, and A. Phunpueok, “Luminescence and scintillation of Eu2+-doped high silica glass,” *physica status solidi (RRL) - Rapid Research Letters*, vol. 5, no. 1, pp. 40–42, Jan. 2011.

[54] S. Schweizer, B. Henke, P. T. Miclea, B. Ahrens, and J. a. Johnson, “Multi-functionality of fluorescent nanocrystals in glass ceramics,” *Radiation Measurements*, vol. 45, no. 3–6, pp. 485–489, Mar. 2010.

[55] C. Bocker, S. Bhattacharyya, T. Höche, and C. Rüssel, “Size distribution of BaF2 nanocrystallites in transparent glass ceramics,” *Acta Materialia*, vol. 57, no. 20, pp. 5956–5963, Dec. 2009.

[56] S. Bhattacharyya, C. Bocker, T. Heil, J. R. Jinschek, T. Höche, C. Rüssel, and H. Kohl, “Experimental evidence of self-limited growth of nanocrystals in glass,” *Nano letters*, vol. 9, no. 6. pp. 2493–6, Jun-2009.

[57] W. Strek, “Size effects on optical properties of Lu2O3:Eu3+ nanocrystallites,” *Journal of Alloys and Compounds*, vol. 344, no. 1–2, pp. 332–336, Oct. 2002.

[58] L. Li, D. M. Strachan, H. Li, L. L. Davis, and M. Qian, “Crystallization of gadolinium- and lanthanum-containing phases from sodium alumino-borosilicate glasses,” *Journal of Non-Crystalline Solids*, vol. 272, no. 1, pp. 46–56, Jul. 2000.

[59] H. Darwish and M. M. Gomaa, “Effect of compositional changes on the structure and properties of alkali-alumino borosilicate glasses,” *Journal of Materials Science: Materials in Electronics*, vol. 17, no. 1, pp. 35–42, Jan. 2006.

[60] E. W. J. L. Oomen and A. M. . van Dongen, “EUROPIUM (III) IN OXIDE GLASSES Dependence of the emission spectrum upon glass composition,” *Journal of Non-Crystalline Solids*, vol. 111, pp. 205–213, 1989.

[61] Z. Zhang, Y. Zhang, X. Li, J. Xu, and Y. Huang, “The relationships between crystal structure of alkaline earth metal hexagonal aluminate and 4f–5d transitions of Ce3+ and Tb3+ ions,” *Journal of Non-Crystalline Solids*, vol. 354, no. 18, pp. 1943–1947, Apr. 2008.

[62] P. I. K. Onorato and D. R. Uhlmann, “Nucleating Heterogeneities and Glass Formation,” *Journal of Non-Crystalline Solids*, vol. 22, pp. 367–378, Jan. 1976.

[63] P. Amista, “Crystallization behaviour in the system MgO_Al2O3_SiO2,” *Journal of Non-Crystalline Solids*, vol. 192–193, pp. 529–533, Dec. 1995.

[64] N. Lahl, K. Singh, L. Singheiser, K. Hilpert, and D.- J, “Crystallisation kinetics in AO-Al2O3-SiO2 -B2O3 glasses (A=Ba , Ca , Mg),” *Journal of Materials Science*, vol. 35, pp. 3089 – 3096, 2000.

[65] M. Nikl, D. Niznansky, J. Ruzicka, C. Cannas, and T. Yanagida, “Silicate Glass-Based Nanocomposite Scinillators,” in *Advances in Nanocomposite Technology*, A. Hashim, Ed. InTech, 2011.

[66] P. A. Tick, N. F. Borrelli, and I. M. Reaney, “The relationship between structure and transparency in glass-ceramic materials,” *Optical Materials*, vol. 15, no. 1, pp. 81–91, Sep. 2000.

[67] D. Dimartino, N. Chiodini, M. Fasoli, F. Moretti, A. Vedda, A. Baraldi, E. Buffagni, R. Capelletti, M. Mazzera, and M. Nikl, “Gd-incorporation and luminescence properties in sol–gel silica glasses,” *Journal of Non-Crystalline Solids*, vol. 354, no. 32, pp. 3817–3823, Aug. 2008.

[68] A. K. Varshneya, *Fundamentals of Inorganic Glasses*. San Diego: Academic Press, Inc., 1994.

[69] A. Paul, *Chemistry of Glasses*, 2nd ed. New York: Chapman and Hall, 1990.

[70] L. Li, H. Li, Q. Maoxu, and D. M. Strachan, “Gadolinium solubility in peralkaline borosilicate glasses,” *Journal of Non-Crystalline Solids*, vol. 283, no. 1–3, pp. 237–245, May 2001.

[71] M. Qian, “Partitioning of gadolinium and its induced phase separation in sodium-aluminoborosilicate glasses,” *Journal of Non-Crystalline Solids*, vol. 333, no. 1, pp. 1–15, Jan. 2004.

[72] L. Li, “Gadolinium solubility in peraluminous borosilicate glasses,” *Journal of Non-Crystalline Solids*, vol. 281, no. 1–3, pp. 189–197, Mar. 2001.

[73] M. Yoshida, A. Mikami, T. Inoguchi, and N. Miura, “Chapter 9: Electroluminescence materials,” in *Phosphor Handbook*, 2nd ed., Taylor & Francis Group, LLC, 2006.

[74] P. Dorenbos, “Scintillation mechanisms in Ce3+ doped halide scintillators,” *Physica Status Solidi (a)*, vol. 202, no. 2, pp. 195–200, Jan. 2005.

[75] a J. Taylor, R. B. Gibson, and J. P. Roberts, "Two-photon absorption at 248 nm in ultraviolet window materials.," *Optics letters*, vol. 13, no. 10, pp. 814–6, Oct. 1988.

[76] Y. Chen, B. Liu, C. Shi, M. Kirm, M. True, S. Vielhauer, and G. Zimmerer, "Luminescent properties of Gd 2 SiO 5 powder doped with Eu 3+ under VUV–UV excitation," *Journal of Physics: Condensed Matter*, vol. 17, no. 7, pp. 1217–1224, Feb. 2005.

[77] Hamamatsu, "Photomultiplier Tubes (PMTs)," *Electron Tube Divsion*. [Online]. Available: http://sales.hamamatsu.com/index.php?id=20009.

[78] K. Kohmoto, "Chapter 5: Phosphors for lamps and displays," in *Phosphor Handbook*, 2nd ed., vol. 225, no. 1–2, Taylor & Francis Group, LLC, 2006.

[79] S. J. L. Ribeiro, R. E. O. Diniz, Y. Messaddeq, L. A. Nunes, and M. A. Aegerter, "Eu3+ and Gd3+ spectroscopy in fluoroindate glasses," *Chemical Physics Letters*, vol. 220, no. 3–5, pp. 214–218, Apr. 1994.

[80] H. Li, L. Li, D. M. Strachan, and M. Qian, "Optical spectroscopy study of neodymium in sodium alumino-borosilicate glasses," *Journal of Non-Crystalline Solids*, vol. 349, pp. 127–132, Dec. 2004.

[81] J. Yang, S. Dai, N. Dai, S. Xu, L. Wen, L. Hu, and Z. Jiang, "Effect of Bi2O3 on the spectroscopic properties of erbium-doped bismuth silicate glasses," *Journal of the Optical Society of America B*, vol. 20, no. 5, p. 810, 2003.

[82] H. Li, M. J. Davis, I., Alexander J. Marker, and J. S. Hayden, "Glass and Light," *International Journal of Applied Glass Science*, vol. 1, no. 1, pp. 63–73, Mar. 2010.

[83] I. Fanderlik, *Optical Properties of Glass*. New York: Elsevier, 1983.

[84] Y. Dwivedi and S. Rai, "Optical properties of Eu3+ in oxyfluoroborate glass and its nanocrystalline glass," *Optical Materials*, vol. 31, no. 1, pp. 87–93, Sep. 2008.

[85] G. Pucker, K. Gatterer, H. Fritzer, M. Bettinelli, and M. Ferrari, "Optical investigation of Eu3+ in a sodium borosilicate glass: Evidence for two different site distributions.," *Physical review. B, Condensed matter*, vol. 53, no. 10, pp. 6225–6234, Mar. 1996.

[86] M. H. Bartl, K. Gatterer, H. P. Fritzer, and S. Arafa, "Investigation of phase separation in Nd3+ doped ternary sodium borosilicate glasses by optical spectroscopy.," *Spectrochimica acta. Part A, Molecular and biomolecular spectroscopy*, vol. 57, no. 10, pp. 1991–9, Sep. 2001.

[87] H. Li, Y. Su, L. Li, and D. M. Strachan, “Raman spectroscopic study of gadolinium(III) in sodium-aluminoborosilicate glasses,” *Journal of Non-Crystalline Solids*, vol. 292, no. 1–3, pp. 167–176, Nov. 2001.

[88] H. Li, L. Li, J. D. Vienna, M. Qian, Z. Wang, J. G. Darab, and D. K. Peeler, “Neodymium(III) in alumino-borosilicate glasses,” *Journal of Non-Crystalline Solids*, vol. 278, no. 1–3, pp. 35–57, Dec. 2000.

[89] J. Bull, G. Selvaduray, and D. Leiser, “Sol-Gel Synthesis and Densification of Aluminoborosilicate Powders Part 1-Synthesis N / LRA National Aeronautics and,” no. September, 1992.

[90] D. Chen, Y. Wang, Y. Yu, and P. Huang, “Structure and Optical Spectroscopy of Eu-Doped Glass Ceramics Containing GdF3 Nanocrystals,” *Journal of Physical Chemistry C*, pp. 18943–18947, Nov. 2008.

[91] J. F. Schairer and N. L. Bowen, “The System Na2O-Al2O3-SiO2,” *American Journal of Science*, vol. 254, pp. 129–195, 1956.

[92] J. E. Shelby, *Introduction to Glass Science & Technology*, 2nd ed. Cambridge: The Royal Society of Chemistry, 2009.

[93] J. P. Schaffer, A. Saxena, S. D. Antolovich, T. H. J. Sanders, and S. B. Warner, *The Science & Design of Engineering Materials*, 2nd ed. Boston: McGraw-Hill Book Company, Inc., 1999.

[94] S. Baccaro, A. Cecilia, E. Mihokova, M. Nikl, K. Nitsch, and P. Polato, “Radiation damage induced by gamma irradiation on Ce3+ doped phosphate and silicate scintillating glasses,” *Nuclear Instruments and Methods in Physics Research Section A: Accelerators, Spectrometers, Detectors and Associated Equipment*, vol. 476, pp. 785–789, 2002.

[95] Y. Wang and J. Ohwaki, “New transparent vitroceramics codoped with Er3+ and Yb3+ for efficient frequency upconversion,” *Applied Physics Letters*, vol. 63, no. 24. p. 3268, 1993.

[96] R. S. Meltzer, W. M. Yen, Z. Hairong, S. P. Feofilov, M. J. Dejneka, B. M. Tissue, and H. B. Yuan, “Effect of the matrix on the radiative lifetimes of rare earth doped nanoparticles embedded in matrices,” *Journal of Luminescence*, vol. 94–95, pp. 217–220, 2001.

[97] Y. Mita, “Chapter 12: Other phosphors,” in *Phosphor Handbook*, 2nd ed., Taylor & Francis Group, LLC, 2006.

[98] A. Edgar, “Photo-stimulated luminescence from europium-doped rubidium barium bromide in fluorozirconate glass ceramics,” *Journal of Luminescence*, vol. 108, no. 1–4, pp. 19–23, Jun. 2004.

[99] A. Sakamoto and S. Yamamoto, “Glass-Ceramics: Engineering Principles and Applications,” *International Journal of Applied Glass Science*, vol. 1, no. 3, pp. 237–247, Sep. 2010.

[100] I. Oprea, “Optical Properties of Borate Glass-Ceramics,” 2005.

[101] G. Dantelle, M. Mortier, and D. Vivien, “Nucleation efficiency of erbium and ytterbium fluorides in transparent oxyfluoride glass-ceramics,” *Journal of Materials Research*, vol. 20, no. 2, pp. 472–481, 2005.

[102] M. Mortier and G. Patriarche, “Structural characterisation of transparent oxyfluoride glass-ceramics,” *Journal of Materials Science*, vol. 5, pp. 4849 – 4856, 2000.

[103] D. Uhlmann, “Nucleation, Crystallization and Glass Formation,” *Journal of Non-Crystalline Solids*, vol. 39, pp. 693–698, 1980.

[104] G. K. DasMohapatra, “A spectroscopic study of cerium in lithium–alumino–borate glass,” *Materials Letters*, vol. 35, no. 1–2, pp. 120–125, Apr. 1998.

[105] S. Y. Marzouk and F. M. Ezz-Eldin, “Optical study of Ce3+ ion in gamma-irradiated binary barium-borate glasses,” *Physica B: Condensed Matter*, vol. 403, no. 18, pp. 3307–3315, Sep. 2008.

[106] D. E. Day and G. E. Rindone, “Properties of Soda Aluminosilicate Glasses: I, Refractive Index, Density, Molar Refractivity, and Infrared Absorption Spectra,” *Journal of the American Ceramic Society*, vol. 45, no. 10, pp. 489–496, Oct. 1962.

[107] K. Gatterer, “Suitability of Nd(III) absorption spectroscopy to probe the structure of glasses from the ternary system Na2O–B2O3–SiO2,” *Journal of Non-Crystalline Solids*, vol. 231, no. 1–2, pp. 189–199, Jul. 1998.

[108] P. Dorenbos, J. T. M. de Haas, and C. W. E. van Eijk, “Non-Proportionality in the Scintillation and the Energy Resolution with Scintillation Crystals,” vol. 42, no. 6, pp. 2190–2202, 1995.

[109] H. Halem, *Glass Notes*, 3rd ed. Kent, OH: Franklin Mills Press, 1996.

[110] S. Tanabe, “Optical transitions of rare earth ions for amplifers: how the local structure works in glass,” *Journal of Non-Crystalline Solids*, vol. 259, pp. 1–9, 1999.

[111] T. Ishizaka, Y. Kurokawa, T. Makino, and Y. Segawa, “Optical properties of rare earth ion (Nd3+‡, Er3+‡ and Tb3+) - doped alumina films prepared by the sol-gel method,” *Optical Materials*, vol. 15, pp. 293–299, 2001.

[112] K. Narita, “Chapter 4: Practical phosphors,” in *Phosphor Handbook*, 2nd ed., Taylor & Francis Group, LLC, 2006.

[113] K. Arai, H. Namikawa, K. Kumata, T. Honda, and Y. Ishii, “Aluminum or phosphorous co-doping effects on the fluorescence and structural properties of neodymium-doped silica glass,” *Journal of Applied Physics*, vol. 59, p. 3430, 1986.

[114] A. Vedda, N. Chiodini, D. Dimartino, and M. Fasoli, “Insights into microstructural features governing Ce3+ luminescnece efficiency in sol-gel silica glasses,” *Chemistry of Materials*, vol. 18, pp. 6178–6185, 2006.

[115] E. Antić-Fidančev, J. C. Krupa, and M. Lemaître-Blaise, “Optical Study of Rare Earth Metaborates Doped with Europium as a Local Structural Probe,” *Materials Science Forum*, vol. 315–317, pp. 373–379, 1999.

[116] J. Bei, G. Qian, X. Liang, S. Yuan, Y. Yang, and G. Chen, “Optical properties of Ce3+-doped oxide glasses and correlations with optical basicity,” *Materials Research Bulletin*, vol. 42, no. 7, pp. 1195–1200, Jul. 2007.

[117] K. Gatterer, G. Pucker, H. Fritzer, and S. Arafa, “Hypersensitivity and nephelauxetic effect of Nd(III) in sodium borate glasses,” *Journal of Non-Crystalline Solids*, vol. 176, no. 2–3, pp. 237–246, Nov. 1994.